9-1-2021

AN EXPERIMENTAL STUDY OF LIPID-MEMBRANE BASED STRUCTURE FORMATION AND DEVELOPMENT OF A RESPONSIVE SYSTEM

Rui Cao
University of Massachusetts Amherst

AN EXPERIMENTAL STUDY OF LIPID-MEMBRANE BASED STRUCTURE FORMATION AND DEVELOPMENT OF A RESPONSIVE SYSTEM

A Dissertation Presented

By

RUI CAO

Submitted to the Graduate School of the

University of Massachusetts Amherst in partial fulfillment

of the requirements for the degree of

DOCTOR OF PHILOSOPHY

September 2021

Department of Physics

AN EXPERIMENTAL STUDY OF LIPID-MEMBRANE BASED STRUCTURE FORMATION AND DEVELOPMENT OF A RESPONSIVE SYSTEM

A Dissertation Presented

by

RUI CAO

Approved as to style and content by:

_____

Anthony D. Dinsmore, Chair

_____

Jennifer Ross, Member

_____

Christian Santangelo, Member

_____

Sankaran Thayumanavan, Member

_____

Narayanan Menon, Department Head

Department of Physics, University of Massachusetts Amherst

ACKNOWLEDGMENTS

I would like to thank my advisor Professor Tony Dinsmore, who instructed me with great enthusiasm, patience and knowledge to proceed my research. I would not have gone this far without his help. I enjoy the friendly and helpful lab atmosphere Tony builds as well. Additionally, I would like to thank my committee members, Professor Jennifer Ross, Professor Christian Santangelo and Professor Sankaran Thayumanavan for their help in suggestions and feedback in my research works.

Moreover, I would like to show my appreciation to my collaborators Jingjing Gao, Vikash Kumar, Manisha and Ann Fernandez in Thayumanavan's lab. They offered me a lot of materials to fulfill some interesting ideas, we had a great experience during the collaboration.

I also would like to show my gratitude to all lab members in Dinsmore lab. I benefit a lot from our regular group meeting by receiving various ideas and suggestions in research. Besides, everyone is friendly and communicative in daily life which helps me adapt to American lives. As a non-native speaker, I really feel at home in our lab.

Finally, I would like to thank my family and friends. Having been in the United States for 6 years, I would not have made it without their support.

ABSTRACT

AN EXPERIMENTAL STUDY OF LIPID-MEMBRANE BASED STRUCTURE FORMATION AND DEVELOPMENT OF A RESPONSIVE SYSTEM

SEPTEMBER 2021

RUI CAO

B.S. UNIVERSITY OF SCIENCE AND TECHNOLOGY OF CHINA

M.S. UNIVERSITY OF MASSACHUSETTS AMHERST

PH.D. UNIVERSITY OF MASSACHUSETTS AMHERST

Directed by: Professor Anthony D. Dinsmore

The lipid bilayer membrane is an interesting material showing great potential for application in responsive systems because of its flexibility, fluidity, impermeability, and tunable interaction with surrounding polymer and particles. In this dissertation, we show how interactions of lipid bilayer vesicles with surrounding polymers or particles leads to formation of macroscopic materials with tunable properties. We first focus on polymer-membrane interactions. We find that after exposing a positively charged polyelectrolyte (PDADMAC) to vesicles, polymer adsorption and vesicle gelation happens due to the electrostatic interaction, which results a macroscopic aggregated phase, named a vesicle-gel. Using optical microscopy, we found that the vesicle gel retains a closed-cell form. Our shear rheology measurements show that vesicle gel is a solid material with a non-zero shear modulus (of order Pa) and a wide linear response region (yield strain as large as 0.7). We showed that the vesicle gel performance could be tuned with PDADMAC concentration. We attribute the shear modulus to the relaxation of polymer rather than stretching or bending of membranes. Our permeation experiment shows that PDADMAC can significantly modify membrane permeability.

Second, we found a new type of structure forming with high polyelectrolyte concentration: a special object with astonishing internal structures which we refer as a vesicle "superparticle." These objects are approximately 10 to 50 μm in diameter and their interiors are filled with membrane-defined compartments. We show that the internal structure comes from inner membranes of mutilamellar vesicles. Our results show the inner membrane lamellae reorganize when vesicles are exposed to a PDADMAC concentration above threshold (e.g., 14 mg/mL for 400 kDa) while the superparticle's internal structures can be released after the outside PDADMAC concentration is lowered.

Last, we design and demonstrate a light-responsive system that can either form a vesicle-gel or disrupt vesicles and release cargo in response to ultraviolet light. We us charge-converting particles that formed by self-assembly of amphiphilic polymers combined with vesicles. Working with our colleagues Jingjing Gao and S. Thayumanavan, we showed that the final vesicle states can be tuned by varying the charge density combination between membranes and particles. Our results show that there are 4 different vesicle states composed of non-adhesion (free vesicles), vesicle-vesicle adhesion (and the gel phase), vesicle rupture as flexible residues, vesicle rupture as compact residues and spherical caps. We attribute the formation of the different states to the competition between bending and adhesion energy. When adhesion energy is smaller than bending energy, membranes partially wrap particles and double layer interaction is induced, which leads to vesicle-vesicle adhesion. When adhesion energy is larger than bending energy, particles are fully wrapped and membranes tension is increased, which leads to vesicle rupture.

Overall, this thesis shows how controlling adhesive interactions among lipid bilayer vesicles and surrounding polymers or particles leads to formation of new mesoscopic and macroscopic structures. The vesicle-gel reported here could find application as a closed-cell, 99% water solid platform for releasing cargo in response to a stimulus, either by tuning membrane permeability or by disruption of the vesicles.

TABLE OF CONTENTS

Page

LIST OF FIGURES

Chapter 1

INTRODUCTION

Cells are life units with lots of amazing functionalities. A cell usually comprises nuclei, organelles, cytoplasm, and the outer (plasma) membrane as shown in Figure 1.1. The membrane, composed of lipids plus added proteins and sugars, plays several important roles in the survival of a cell: it is a wall, separating nuclei and other organelles from the cytoplasm and from the outside environment; it is also a channel, allowing water and ions to pass selectively; it is a porter, delivering proteins and hormones to their destinations through endocytosis and exocytosis. In this thesis, we are going to explore the properties and potential applications of the lipid membranes.

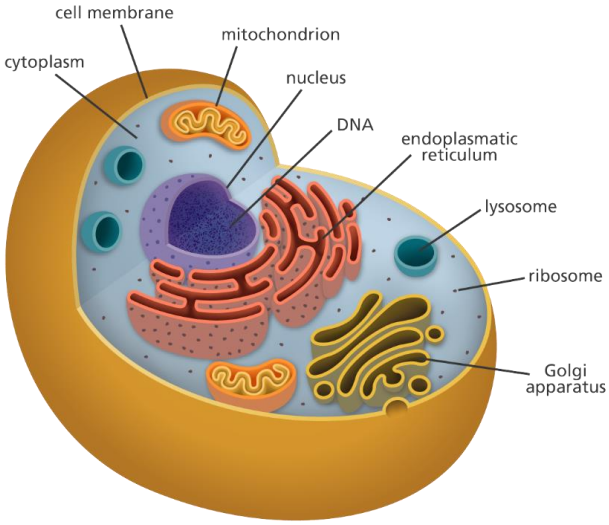

Figure 1.1: A schematic diagram of human body cell (From www.yourgenome.org)

The molecules which are named as phospholipids and composed of the cell membrane play an important role in accomplishing these functionalities. The general approach in this thesis is to tune the mesoscopic and macroscopic structures of membranes by adding polymers or nanoparticles that bind to the membrane with controllable strength. We begin with lipid bilayer vesicles, ranging from roughly 1 μm to 50 μm and consisting of a membrane surrounding an aqueous interior. When particles or polymers are added, the charges on the particles, polymers and membrane lead to attractive forces that drive structure

formation. The resulting structures include a solid gel of vesicles, which roughly resembles a cellular tissue or a membraneous web [1]; a suspension of large vesicles filled with defined interior compartments; and ruptured vesicle/particle composites that release cargo from within the vesicles.

In this chapter, we will discuss the structures of lipid molecules and the properties of lipid bilayer membranes. We then turn to a discussion of shear rheology and its working principles, which will be used in this thesis to characterize the vesicle-based gels. Additionally, we will briefly explain the electrostatic double-layer interaction between charged surfaces in water containing free ions. We will also discuss the energy competition between bending and adhesion, which determines conditions in which membrane will adhere to one another or fully wrap the adhering particles.

1.1 From Lipids to Vesicles

1.1.1 Lipid and vesicle

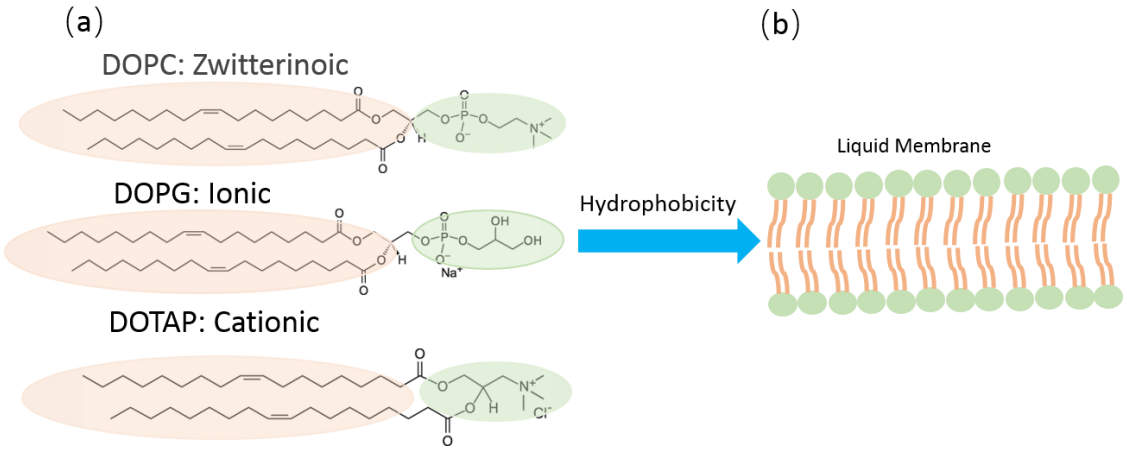

Figure 1.2: (a) Illustrations of 3 kinds of lipids: DOPC, DOPG and DOTAP. Each molecule has two unsaturated hydrophobic tails and one hydrophilic head (Molecular structures come from www.avantilipids.com). The head groups can carry charges given the head structure. (b) Lipids form bilayer structure to overcome hydrophobicity.

Figure 1.2(a) shows the molecular structures of three kinds of lipids, 1,2-dioleoyl-sn-glycero-3-phosphocholine (DOPC) 1,2-dioleoyl-sn-glycero-3-phospho-1'-rac-glycerol (DOPG) and 1,2-dioleoyl-3-trimethylammonium-propane (DOTAP). Phospholipids (referred to from now on as just lipids) are

amphiphilic molecules: each lipid has a hydrophilic head (green part in Figure 1.2(a)) and two hydrophobic tails (pink part in Figure 1.2(a)). To help lipids overcome the hydrophobicity energy cost in an aqueous environment, two lipids arrange themselves tail-to-tail and leaving the two hydrophilic heads towards water due to the spontaneous curvature [2]. To further decrease the hydrophobicity energy, this tail-to-tail pattern is extended one by one and a 4-nm-thick lipid bilayer membrane is formed. Due to the unsaturated tail (with the double carbon-carbon bond), the tails are not straight and the membrane is fluid with no shear modulus near room temperature. In other words, each lipid molecules in fact move freely on its own side of the membrane [3] [4]. After the tail-to-tail pattern is aligned, the final hydrophobic energy cost at the membrane ends needs to be handled. The solution is to let the membrane form a closed-form object which makes sure no hydrophobic part is left towards water. The speculated formation process is shown in Figure 1.3(a) [5]. This closed spherical object is referred as a vesicle.

Different lipids have various headgroups, which decides what kind of charge the lipids carry. For example, the head groups of DOPC, DOPG and DOTAP are zwitterionic, cationic and anionic respectively as shown in Figure 1.2(a). Previous studies have shown that DOPC carries slightly negative charge in aqueous solution (with a surface potential of approximately -10 mV), DOPG is heavily negatively charged comparing to DOPC (surface potential up to -80 mV), while DOTAP is positively charge [6] [7].

There is another kind of lipid that is going to be mentioned a lot in chapter 3 and 4, which is named as soy-lecithin (SLPC). SLPC is largely purchased from American Lecithin company, the ingredients are composed of at least 85.0% PC-headgroup lipid, 0 to 6% Lyso-PC lipid and a few amounts of other non-lipid species. In generally, the charge property of SLPC is very similar to that of DOPC due to the same head group.

In some cases, fluorescent lipids were added in order to see the membrane with high contrast. We used a lipid with a 1,2-dioleoyl tail and with a phosphatidylethanolamine headgroup that is

functionalized with rhodamine. These lipids are called Rh-DOPE. Because the tail has the same composition as DOPC, DOPG, and DOTAP, it mixes uniformly in the membrane. When mixed with SLPC, it also mixes uniformly as will be shown later.

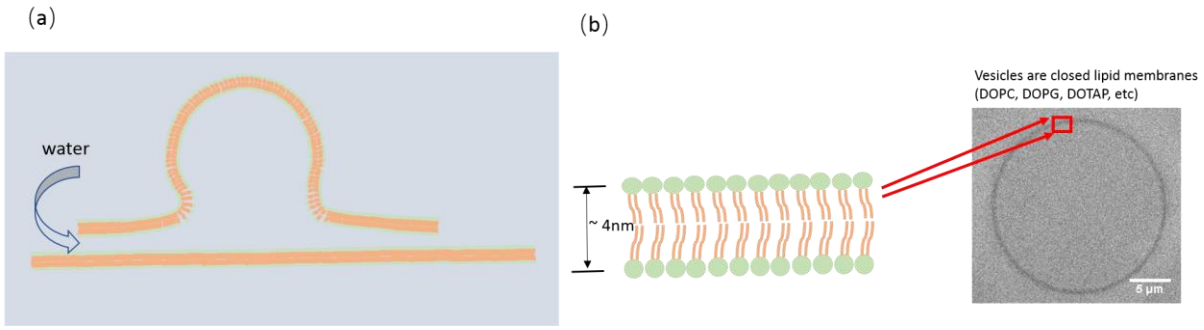

Figure 1.3: (a) Vesicle formation speculation. (b) Vesicle image taken under bright field whose boundary is lipid membrane and the thickness of lipid membrane is roughly 4 nm.

Figure 1.3(b) shows an example of a vesicle composed of lipid membranes imaged under bright field optical microscopy. The membrane serves as a boundary to separate the inside and outside. Vesicle size can range from a few tens of nano meters to micrometer scale, which is correlated with the membrane area. In this thesis, the vesicles used are in the order of micron scale. Vesicles can also be multilamellar: unilamellar vesicles only have one lipid bilayer, while multilamellar vesicles have several inside layers. The shape of vesicles is usually spherical but it can vary because the membrane is soft.

1.1.2 Lipid membrane elasticity

Given that the membrane thickness is much smaller than the membrane's lateral length scale, the simplest way to characterize membrane is to consider it as a two-dimensional surface. The membrane shape can vary [8]. In 1973, Helfrich proposed a classic model describing the bending energy density of closed lipid membrane [9]

$$f_c = \frac{\kappa}{2}(c_1 + c_2 - c_0)^2 + \bar{\kappa} c_1 c_2 = \frac{\kappa}{2}(2H - c_0)^2 + \bar{\kappa} K_G \qquad \text{(Eq. 1.1)}$$

Where c_1 and c_2 are two principle curvatures at a given point on a membrane surface, c_0 is the spontaneous curvature, which is a property of the membrane and is 0 for symmetric lipid bilayers, κ and $\bar{\kappa}$ are bending modulus and Gaussian bending modulus respectively, H and K_G are named mean curvature and Gaussian curvature [10]. The parameter f_c is the free energy per unit membrane area. The key part of this theory is the bending modulus, which describes the energy cost of bending, which comes from compressing one leaflet of the bilayer and stretching the other leaflet. The Helfrich Hamiltonian that includes osmotic pressure Δp (pressure difference between outside and inside) is

$$F_H = \int dA\left(\frac{\kappa}{2}(2H - c_0)^2 + \bar{\kappa}K_G + \lambda\right) + \int dV\,\Delta p \qquad \text{(Eq. 1.2)}$$

dA and dV are area and volume units respectively, λ is the Lagrange multiplier which marks the area constraint, and F_H is the total free energy. The area constraint comes from the conservative of total lipid amount.

After taking the first order variations, Ou-Yang, *et al*., derived the equation describing the equilibrium shape [11] [12] of a free vesicle:

$$\Delta p - 2\lambda H + \kappa(2H + c_0)(2H^2 - c_0 H - 2K_G) + 2\kappa\nabla^2 H = 0 \qquad \text{(Eq. 1.3)}$$

Eq. 1.3 has shown the physical parameters affecting vesicle geometry are the osmotic pressure andbending modulus. The Gaussian bending modulus is excluded as long as the membrane surface topology remains fixed (*i.e.*, no holes appear) [13]. These parameters will be mentioned multiple times in the following chapters.

When oppositely charged particles or polymers approach a membrane, they can bind and induce adhesion of vesicles, which will be described in Section 1.3.1, below. When a spherical particle binds to a membrane, there is a competition between the adhesion, and the bending modulus, which can lead to complete wrapping of the particle. This topic is described in Section 1.3.2, below.

1.2 Shear rheology

We found that when vesicles adhere to one another, they form as solid material (as will be described later). To characterize this gel, we need to distinguish the solid from the initial fluid suspension.

There are two ideal models for materials: Hookean solids and Newtonian liquids. Although most materials are neither of these (being viscoelastic), these models are very informative.

For Hookean solids (pure solid), it states that the stress response of a materials proportional to the applied strain, where σ is the stress and ε is strain, k is the ratio called shear modulus.

$$\sigma = k\varepsilon \qquad \text{(Eq. 1.4)}$$

For Newtonian liquids (pure liquid), the stress is proportional to strain rate like in Eq. 1.4, η is the ratio called viscosity, representing the internal friction of a liquid

$$\sigma = \eta\dot{\varepsilon} \qquad \text{(Eq. 1.5)}$$

From Eq. 1.4 and 1.5, it is not hard to find that for pure solid, the strain and stress should be in the same phase while for pure liquid, the stress response has a phase lag comparing with the applied strain. But given a viscoelastic system, how to characterize its properties? Is it a pure viscous system or elastic system?

The answer lies in the rheology [14]. Rheology is the study of the flow of matter, either in a liquid state, or as "soft solids" or solids under conditions in which they respond with flow rather than deforming elastically in response to an applied force. Rheology measurements are done using a rheometer, shown in Figure 1.4(a). After a sample is loaded in the rheometer, excessive material should be trimmed around the cone. The motor rotates the cone to apply a time-varying strain to the sample.

In fact, rheology is like a black box, giving it an input and receiving an output. Based on the input and output, physical properties of a material can be inferred. For example, if the input is a harmonic strain

with strain amplitude ε_0 and frequency ω

$$\varepsilon(t) = \varepsilon_0 sin\omega t, \quad \text{(Eq. 1.6)}$$

then we measure a stress response

$$\sigma(t) = \sigma_0(\omega)\sin(\omega t + \delta(\omega)) \quad \text{(Eq. 1.7)}$$

with stress amplitude $\sigma_0(\omega)$ which is frequency dependent, and there is another phase term $\delta(\omega)$ representing the phase lag between input and output. By replacing $\sigma_0(\omega)$ with ε_0

$$\begin{aligned}\sigma(t) &= \sigma_0(\omega)\sin(\omega t + \delta(\omega)) \\ &= \varepsilon_0[\tfrac{\sigma_0(\omega)}{\varepsilon_0} cos\delta(\omega)\sin(\omega t) + \tfrac{\sigma_0(\omega)}{\varepsilon_0} sin\delta(\omega)\cos(\omega t)] \\ &= \varepsilon_0(G'\sin(\omega t) + G''\cos(\omega t)) \quad \text{(Eq. 1.8)}\end{aligned}$$

with

$$G' = \tfrac{\sigma_0(\omega)}{\varepsilon_0} cos\delta(\omega),\ G''=\tfrac{\sigma_0(\omega)}{\varepsilon_0} sin\delta(\omega) \quad \text{(Eq. 1.9)}$$

Figure 1.4(b) shows a typical strain-stress response. Here two parameters dependent on frequency are derived: G' is called the storage modulus and G'' is called the loss modulus. First let us think about the dimension of G' and G''. Stress has dimension $F/_{m^2}$ and strain is dimensionless, so G' and G'' have the same dimensions as stress, which is P_a or $J/_{m^3}$. Now referring back to Eq. 1.9, G' is in the same phase as input and G'' is out of phase, which shows that G' represents the solid-like elastic behavior of a material and G'' is the liquid-like viscous behavior. So the physical meaning for G' is how much energy can be stored per volume during shear in which volume is conserved, and G'' is how much energy is consumed (dissipated) per volume.

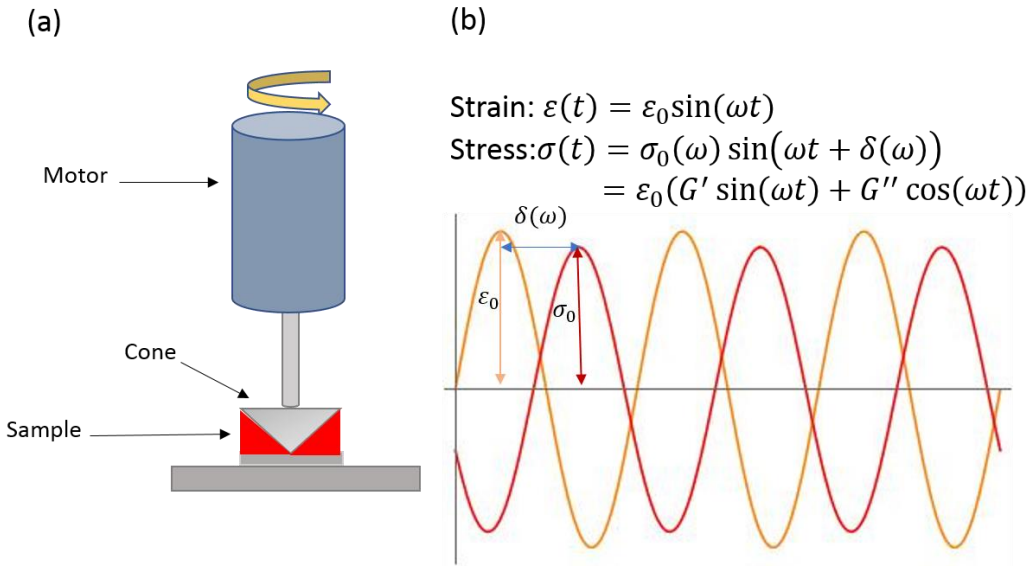

Figure 1.4: (a) Schematic plot of shear rheology. After sample is loaded, motor drives the cone to apply strain to the sample. (b) A typical strain-stress response illustration.

Figure 1.5 shows the rheology results for compressed emulsions made by Mason, *et al.* [15]. We can see in the frequency sweep in Figure 1.5(a) that G′ is larger than G′′ and is nearly constant with respect to frequency which represents the emulsions measured in this experiment are solid. Figure 1.5(b) shows the strain amplitude dependence, indicating the yield strain of different concentrations of emulsions. The highest yield strain of compressed emulsion is roughly 0.04 when the effective volume fraction ϕ_{eff} is 0.80.

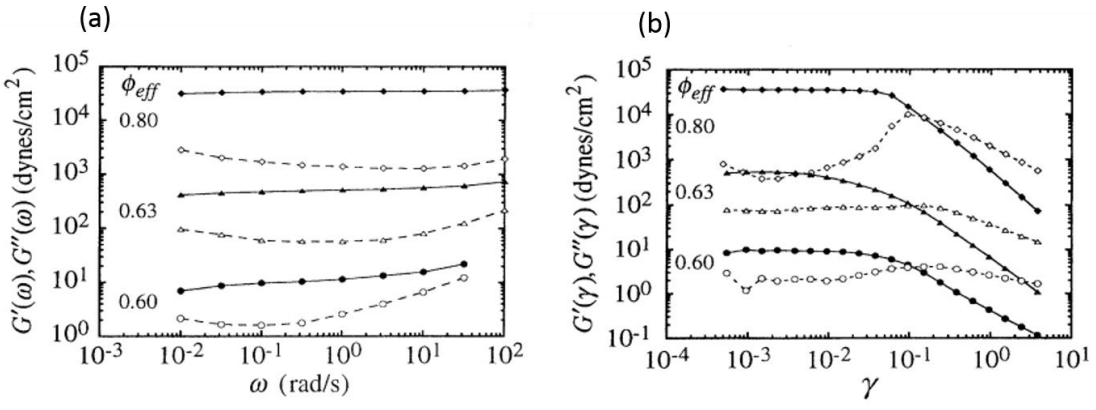

Figure 1.5 Shear rheology results of compressed emulsions (Figure copied from Mason et al, PRL). (a) Frequency sweep of emulsions in different volume ratios. (b) Strain amplitude dependence sweep of emulsions. Figures adapted from Mason, et al, Phys. Rev. Lett. **75**, 1995.

The criterion to classify a material as solid and liquid is to compare storage and loss modulus at (ideally) 0 frequency. If the storage modulus is constant and has a value that is larger than the loss modulus, a viscoelastic solid behavior is shown; on the contrary, if loss modulus is larger, the material may be classified as a viscoelastic liquid.

1.3 Particle-membrane interaction

1.3.1 Double layer interaction

Given the fact that lipid membranes are often charged, vesicles are able to interact with free charged particles or other vesicles in the solution. The interaction has been explained well by Poisson-Boltzmann model. We consider negatively charged vesicles that coexist with free positive and negative ions in aqueous solution, as shown in Figure 1.6(a). We do not consider the membrane elasticity at this moment but only think about the electrostatic interaction between a rigid, flat membrane and particles. This section summarizes the electrostatic double-layer interaction, based on the references Colloidal Dispersions (B. Russel, D. A. Saville, W. R. Schowalter, Cambridge University Press, 1989).

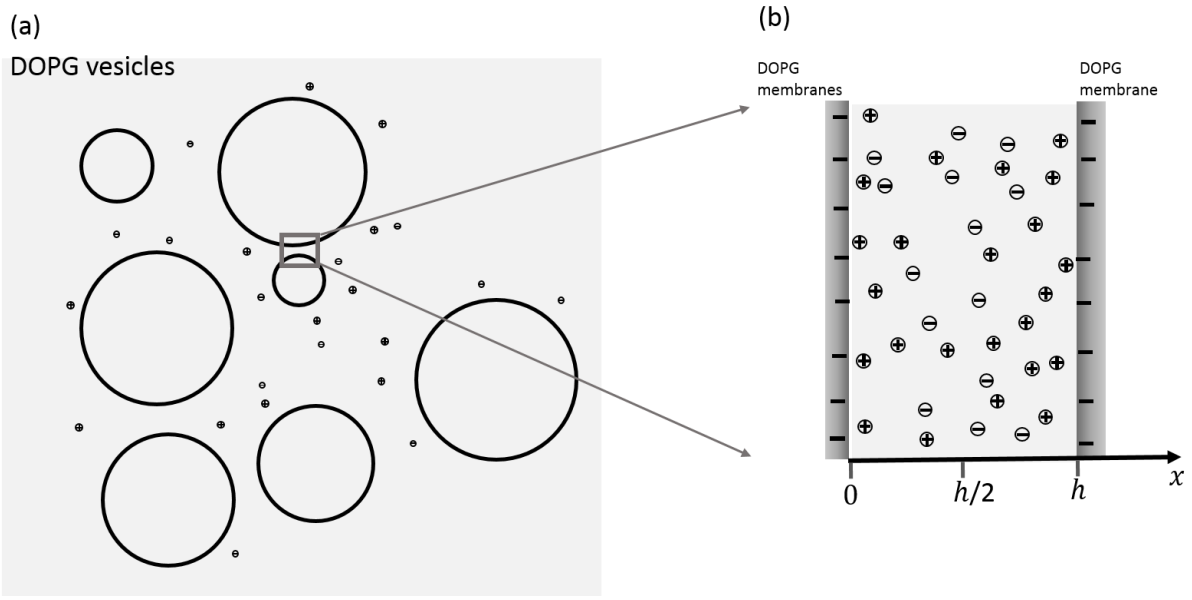

Figure 1.6: (a) Schematic plot of vesicle coexisting with ions. (b) Zoom in of two close vesicles, which are treated as flat, charged plates

For simplicity, we assume all positive and negative ions carry equal amount of charge q and $-q$ with ion size far less than vesicle size. We can treat the membranes as two infinitely large uniformly charged plates as shown in Figure 1.6(b). Assume the distance between two vesicles is h, and we create a coordinate x to represent the distance between left side membrane and an inside point.

Now let's only consider the electric field induced by the left side membrane. Assume the electric potential in the space is $\psi(x)$, from Poisson equation, we have

$$\frac{d^2\psi(x)}{dx^2} = -\frac{\rho(x)}{\varepsilon\varepsilon_0} \qquad \text{(Eq. 1.10)}$$

ε_0 is the dielectric permittivity, ε is the dielectric constant. $\rho(x)$ is the charge density in the space. Given both positive and negative charge exists, we have

$$\rho(x) = q\big(n_+(x) - n_-(x)\big) \qquad \text{(Eq. 1.11)}$$

$n_+(x), n_-(x)$ are positive and negative ion density which are characterized by the Boltzmann distribution

$$n_+(x) = n_\infty e^{-\beta q\psi(x)} \qquad \text{(Eq. 1. 12)}$$

$$n_-(x) = n_\infty e^{\beta q\psi(x)}, \qquad \text{(Eq. 1.13)}$$

where n_∞ is the particle density at infinite position and $\beta = \frac{1}{k_B T}$.

Taking Eq. 1.11, 1.12, 1.13 to 1.10, we can get

$$\frac{d^2\psi(x)}{dx^2} = \frac{qn_\infty(e^{\beta q\psi(x)} - e^{-\beta q\psi(x)})}{\varepsilon\varepsilon_0}. \qquad \text{(Eq. 1.14)}$$

When the potential or membrane charge density is not too high, Eq. 1.14 can be approximated by Debye-Hückle theory by expanding the exponential term with Taylor expansion to the first order [16]:

$$\frac{d^2\psi(x)}{dx^2} = \frac{2\beta n_\infty q^2}{\varepsilon\varepsilon_0}\psi(x) = \frac{\psi(x)}{l_D^2} \qquad \text{(Eq. 1.15)}$$

$l_D = \sqrt{\frac{\varepsilon\varepsilon_0}{2\beta n_\infty q^2}}$ is referred as the Debye length. It characterizes the electric screening distance of the solution and does not depend on the charge density of the surfaces. When $x \gg l_D$, membranes cannot feel the membrane-induced electric field, they still move as free particles like ideal gas (we assume the membranes do not interact with each other by other forces; we neglect van der Waals and solvation forces which are at shorter length scale than l_D). When $x < l_D$, membranes' movement are affected due to the impact from electric filed.

If we assume the membrane surface potential is ψ_0, by solving Eq. 1.15, we can get the electrostatic potential is

$$\psi(x) = \psi_0 e^{-\frac{x}{l_D}}. \qquad \text{(Eq. 1.16)}$$

Following the same idea, we can get the potential induced by right side is

$$\psi(x) = \psi_0 e^{-\frac{h-x}{l_D}}. \qquad \text{(Eq. 1.17)}$$

So the total potential is

$$\psi_{total}(x) = \psi_0(e^{-\frac{x}{l_D}} + e^{-\frac{h-x}{l_D}}). \qquad \text{(Eq. 1.18)}$$

The potential plot is shown in Figure 1.7.

From the potential illustration in Figure 1.7 we know that ions with opposite charges are inclined to accumulate in the zone between vesicles due to lower potential energy.

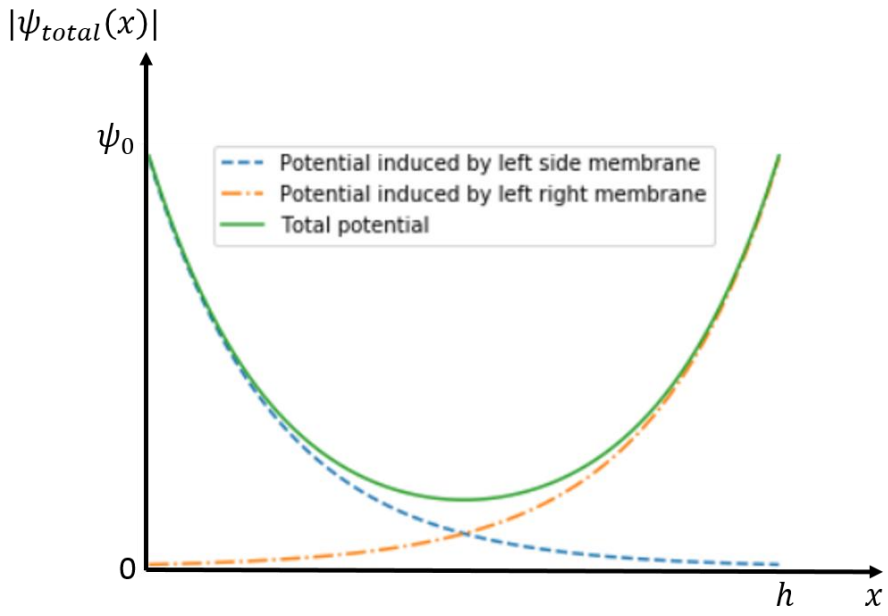

Figure 1.7: Absolute value of potential induced by two membranes.

With the potential, we can estimate the total particle concentration as

$$n_{total}(x) = n_+(x) + n_-(x) = n_\infty(e^{\beta q \psi_{total}(x)} + e^{-\beta q \psi_{total}(x)}) \quad \text{(Eq. 1.19)}$$

Maintaining the assumption of Debye- Hückle theory and expanding $n_{total}(x)$ to second order, we find

$$n_{total}(x) = n_\infty(2 + \beta^2 q^2 \psi_{total}^2(x)) \quad \text{(Eq. 1.20)}$$

From the ideal gas law, osmotic pressure can be represented as

$$p = nk_BT \quad \text{(Eq. 1.21)}$$

where n is particle concentration per volume.

From Eq. 1.20 we conclude that the ion concentration is not homogeneous between two vesicles. The inhomogeneous particle concentration induces an osmotic pressure difference to push two vesicles together as shown in Eq. 1.21, which results in the two vesicles' attracting each other.

The effect described above is called the electrostatic double layer interaction [17]. The first layer represents the charged surface, second layer is the diffuse layer mostly composed of counterions, which leads to the osmotic pressure. In this thesis, we are going to talk about this effect multiple times in later chapters.

The above discussion can also describe the electrostatic double layer interaction between a particle and a membrane. If the separation between the particle surface and membrane is small compared to the particle radius a, then both surfaces can be treated as plate plates, as in Figure 1.6(b).

1.3.2 Bending and adhesion energy competition

After considering the particle-membrane interaction in section 1.3.1, we know that particle binding to membranes can drive vesicles to attract each other. In this section, we are going to discuss the membrane elasticity effect in particle-membrane interaction.

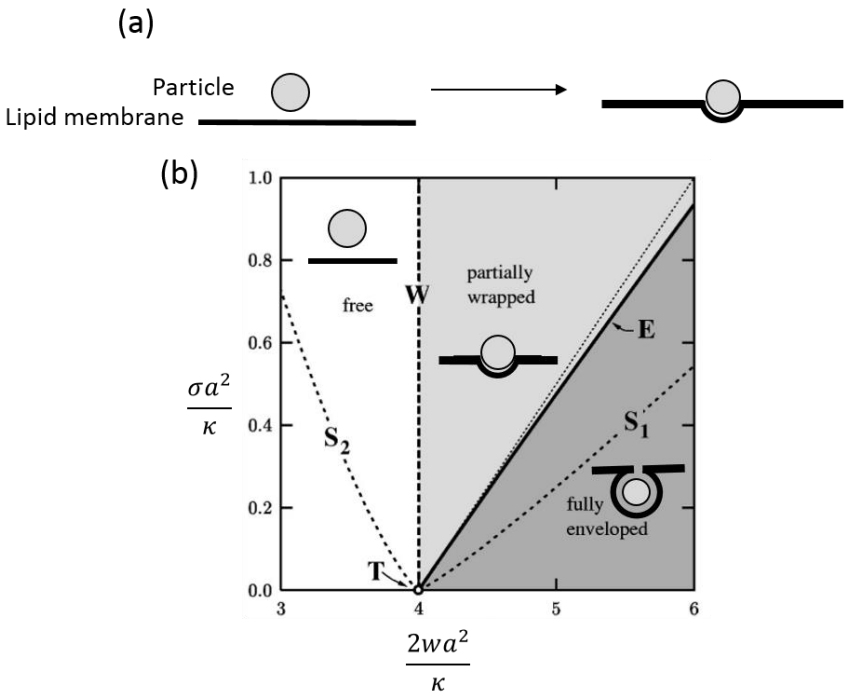

Figure 1.8: (a) Illustration of membrane wrapping over particle. (b) Particle wrapping phase diagram in the dependence on w, κ and σ(Figure adapted from M. Deserno, Phys. Rev E **69**, 031903 2004)

When a particle binds to a membrane as shown in Figure 1.8(a), there is an energy competition among bending, adhesion and tension. We define the particle radius is a, vesicle bending modulus is κ, membrane lateral tension after binding is σ, the adhesion energy per area between particle and membrane is w. Based on the calculation of Deserno, *et al.* [18], total adhesion energy is

$$E_{ad} = -wA_{ad} = -2\pi wza^2 \quad \text{(Eq. 1.22)}$$

where A_{ad} is the adhesion area, z is the degree of wrapping. Bending energy is

$$E_{bend} = \frac{1}{2}\kappa(\frac{1}{a} + \frac{1}{a})^2 A_{ad} = 4\pi z\kappa \quad \text{(Eq. 1.23)}$$

The energy paid to membrane tension is

$$E_{bend} = \pi a^2 z^2 \sigma \quad \text{(Eq.1.24)}$$

The energy competition is going to decide the particle wrapping state as shown in Figure 1.8(b). We can see when adhesion energy is fairly weak ($\frac{2wa^2}{\kappa} < 4$), particles are free and have no interaction with membrane. When adhesion energy exceeds a threshold ($\frac{2wa^2}{\kappa} > 4$), particle-membrane interaction is strong enough to drive membranes to wrap particles. When the membrane tension σ is fixed, the increase in w can lead to a phase transition from partial wrapping to fully wrapping. Therefore, in general, we can see that by varying w, we can get different interaction state.

In conclusion, the particle-membrane interaction can be considered as two parts: one is the double layer interaction bringing two vesicles to adhere with each other; the other part is the membrane wrapping particles. We will discuss these two parts in detail in later chapters.

The remainder of the thesis proceeds as follows: Chapter 2 provides an overview of the experimental methods. In chapter 3, a polyelectrolyte induced vesicle gel will be discussed, where the electrostatic double layer interaction leads to adhesion and structure formation. In chapter 4, we will

discuss a distinct lipid membrane formation referred as superparticles. In chapter 5, vesicle response to charged particles will be discussed. We will show that particle wrapping can be tuned with the electrostatic interaction strength, which can be switched by exposure to ultraviolet light.

Chapter 2

METHODS AND TECHNIQUES

2.1 Introduction

In this chapter, we briefly introduce some technical methods used in our experiments. To fabricate giant vesicles, we implemented two fabrication methods: electroformation and co-solvent. Previous researches have shown both methods are reliable and easy to accomplish [19]. The main difference between these two methods is the size of the resulting vesicles. Electroformation can yield vesicles with size mainly in 10-μm-scale while the co-solvent method mainly produces 1-μm-scale vesicles. In order to observe vesicle states, several microscopy methods were used, including bright field, fluorescence, confocal, and dark field microscopy. Bright field microscopy has been widely used and the mechanism is well-know. Confocal and dark-field microscopies have some similarities with brightfield microscopy, but there are some significant differences in confocal and dark field. Therefore, we will briefly explain the mechanism of confocal and dark field microscopy in this chapter. Besides the technical methods mentioned above, we also implemented some image analysis methods, including adhesion angle measurement between two adhered vesicles, copper bead position tracking and light intensity tracking over time. Some other methods were also adapted in our experiments, including osmotic pressure measurement, solution mixture, etc. They will be displayed in the materials and sample preparation section in following chapters.

2.2 Vesicle fabrication methods

2.2.1 Electroformation

In this thesis, we used two methods to make vesicles. First one is referred as electroformation [20]. A lipid in chloroform stock solution (concentration can be varied) was prepared. Working in a chemical hood, two clean ITO-coated glass slides were coated with 50 μL of a lipid solution. The ITO glasses slides were purchased from Delta Technologies, Part No. CB-501N-S111, size 25x75x1 mm, resistance 5 – 15Ω.

During the lipid coating, we injected the lipid solution on ITO glasses first, then used a clean needle to spray the lipid solution as uniformly as possible, which helped chloroform evaporated within 20s. Then both coated glasses were dried under vacuum for 2 h. The ITO slides were held by Teflon spaces with their ITO-coated surfaces facing one another. The gap between them (3 mm thick) was filled with 3mL of 180 mOsm/L aqueous sucrose solution (unless otherwise mentioned). Electroformation was carried out at 40 °C with a sinusoidal applied voltage at 10 Hz and peak-to-peak voltage 2.4 V for 105 min. After transferring the vesicle suspension to a vial, we added 2.5 mL of glucose solution of identical osmolarity. After letting this sample sediment for 24 h, we collected 300 µL of concentrated vesicle suspension from the bottom. The electroformation procedure is shown in Figure 2.1.

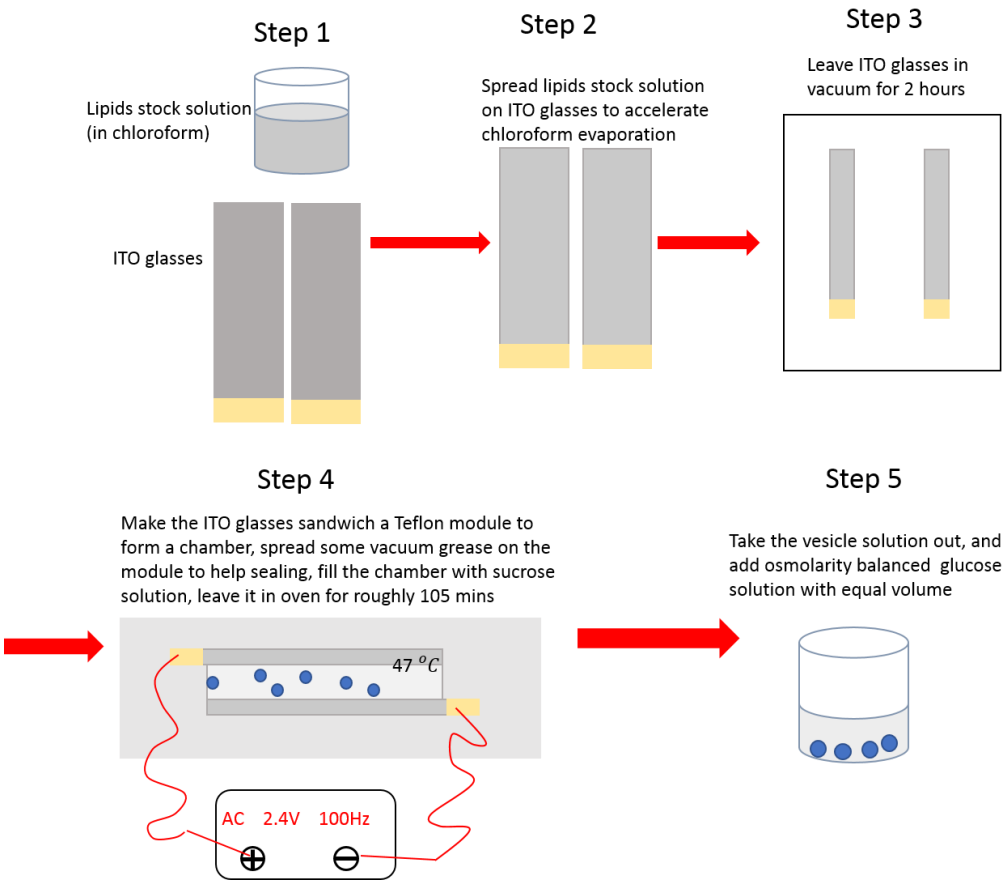

Figure 2.1: Illustration of electroformation procedure

2.2.2 Co-solvent

The co-solvent method was used to obtain vesicles with a diameter of approximately 1 μm. 500 μL of 180 mOsm/L sucrose solution was added dropwise to 1 mL of SLPC (mentioned in chapter 1.1.1) stock solution (1mg/mL stock solution of SLPC in tetrahydrofuran (THF)), while stirring (60 rev/min). The solution was left in a hood for 36 h to let the THF evaporate. We then injected 500 μL of glucose solution (180 mOsm/L), allowed it to sediment for 1h, and then collected 120 μL of concentrated vesicles at the bottom. The procedure of co-solvent method is shown in Figure 2.2.

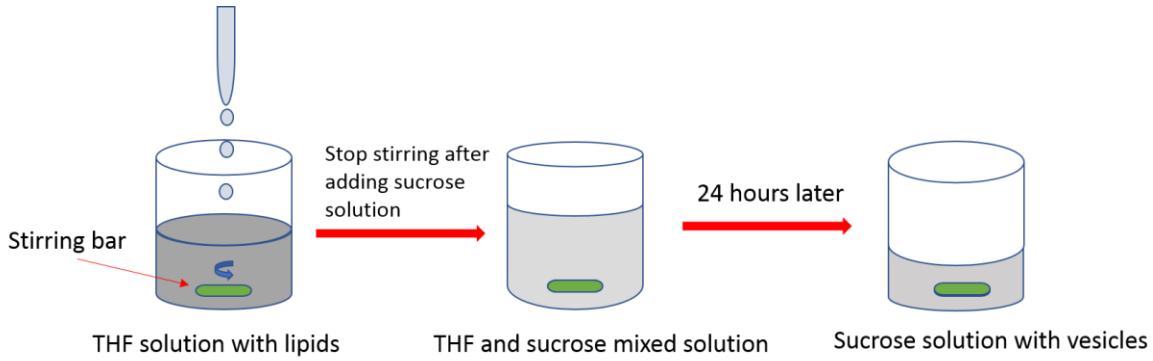

Figure 2.2: Illustration of co-solvent method procedure

The vesicle yield between these two methods has a significant difference in vesicle size. Vesicles fabricated via electroformation has radii in 10 μm scale while vesicles fabricated via co-solvent is roughly in 1 μm scale. In Figure 2.3, we show two images comparing the typical yield of vesicles fabricated via electroformation and co-solvent. We are going to use this difference in next chapter.

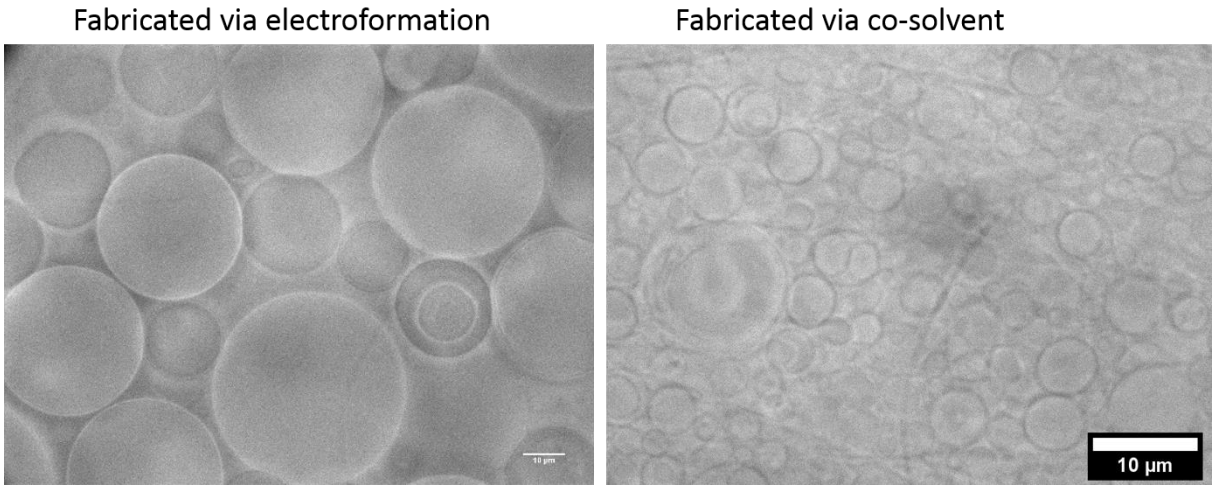

Figure 2.3: Vesicle yield comparison between electroformation and co-solvent (SLPC vesicles)

2.3 Confocal microscopy

Confocal microcopy is a fluorescent microscopy technique that blocks light from outside the focal plane and only allows light from the focal plane to pass [21]. Therefore, confocal microscopy is widely used for 3D imaging. The principle of confocal microscopy is shown in Figure 2.4(a). The excitation laser light passes through a pinhole (light source pinhole aperture in Figure 2.4(a)) and an excitation filter. After encountering a reflective mirror, the incident laser hits the loaded sample and excites fluorescence. During the path towards to detector, the excitation light is blocked by a filter (fluorescence barrier filter in Figure 2.4(a)) but fluorescence is transmitted. Then comes a crucial point: another pinhole is set after the filter and blocks fluorescence from other planes but leaves fluorescence from the focal plane to pass. In this dissertation, we report confocal microscopy images of samples in later chapters. Figure 2.4(a) shows a fluorescent image of DOPC vesicles doped with 0.1% Rhodamine-DOPE (a fluorescent lipid) taken by a Hamamatsu digital camera C11440, a Zeiss 63× Plan Neofluar objective(1.4 NA) and a confocal custom system based on the VTEye confocal module from Visitech International.

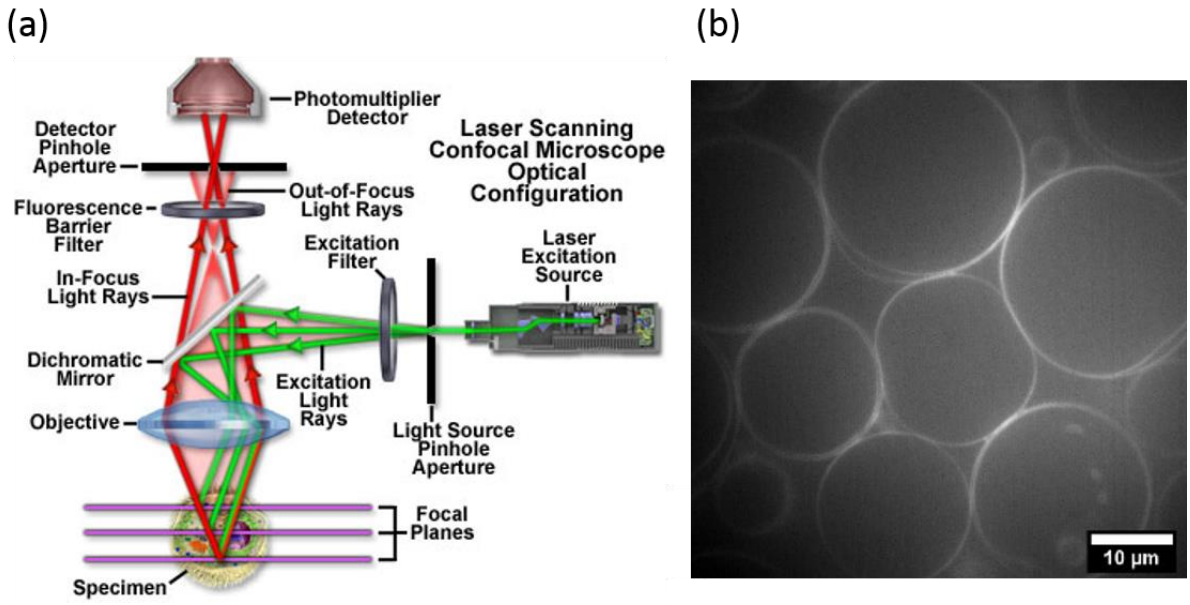

Figure 2.4: (a) Schematic plot of confocal microscopy (from www.olympus-lifescience.com).

(b) Confocal images of DOPC vesicles (0.1% Rhodamine-DOPE is doped).

2.4 Dark field microscopy

Dark-field microscopy was used to obtain high contrast images without fluorescence [22]. The schematic plot explaining the optical path is shown in Figure 2.5(a). The difference from bright field microscopy is that the center of the condenser is blocked but the light near the edge in condenser is transmitted. After the unblocked light hits sample, photons are scattered by objects in the sample. Objects with sharp edges or with high refractive index contrast scatter more strongly than those with smooth edges or low index contrast, so thick objects are brighter than thin objects under dark field. In Figure 2.5(b), we show a picture of DOPC vesicles taken under dark field microscopy. We can see the background issignificantly darker than the vesicle edge. By using dark-field microscopy, we also detected the presence of particles on vesicle membranes, as described in chapter 5.

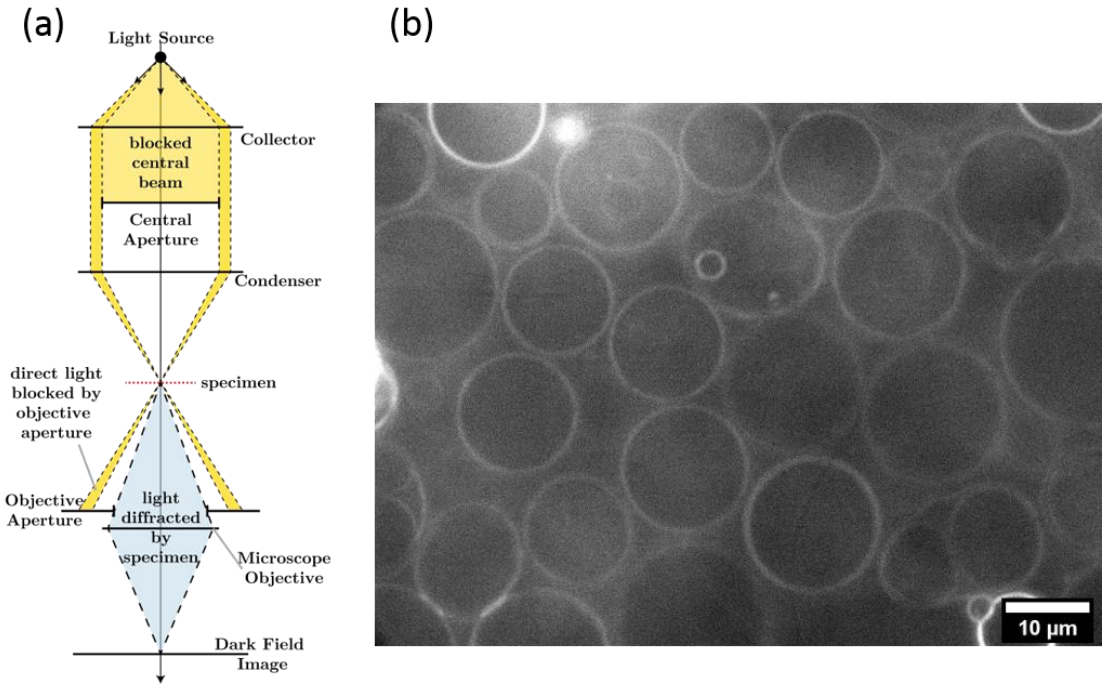

Figure 2.5: (a) Schematic plot of dark field microscopy (www.en.wikipedia.org/wiki/Dark-field_microscopy). (b) A dark field image of DOPC vesicles in a solution of glucose and sucrose.

2.6 Copper bead tracking

In experiments, sometimes we need to track object position overtime. We use python program to track the object movement. Our algorithm is to find one distinct point of the object, then track the point over time. As shown in Figure 2.6, we tracked the center of a copper bead to acquire its displacement. In our program, we assume the light intensity is lowest at the center, so we tracked the point with lowest pixel value.

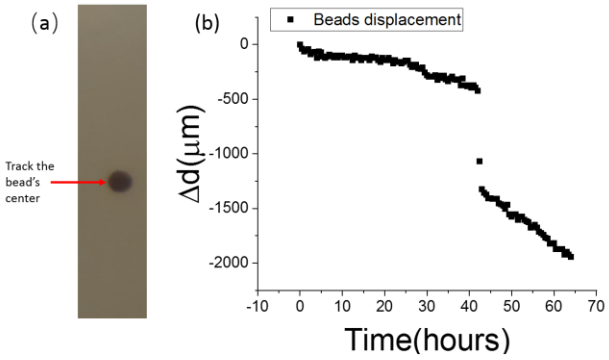

Figure 2.6: (a) Position of copper bead at t = 40 h. The distinct point we selected was the bead center. (b) The bead displacement overtime.

The python code is shown below.

```
import numpy as np

import scipy
import cv2
import matplotlib.pyplot as plt
path = 'cropped1.avi' #cropped1.avi is the video file
cap = cv2.VideoCapture(path)
end_frame = 130
beads_height = np.zeros(end_frame)
consecutive = 10
background = 110
t = 0
while cap.isOpened():
  ret, frame=cap.read()
  gray = cv2.cvtColor(frame, cv2.COLOR_BGR2GRAY)
  m, _ = gray.shape
  if t>=end_frame:
    break
  elif t<84:
    beads_height[t] = np.argmin(gray[:,83])
  else:
    beads_height[t] = np.argmin(gray[:, 87])
  t+=1
```

2.6 Vesicle adhesion angle measurement

To estimate the adhesion energy per area between polyelectrolyte and vesicles, we measure adhesion angle between two adhered vesicles. The adhesion angles were measured through the plugin named “Contact Angle” in Fiji (which is just ImageJ). The installment instruction of the plugin is on NIH

website: https://imagej.nih.gov/ij/plugins/contact-angle.html.After loading images to Fiji as shown in Figure 2.7(b), select "Contact Angle" in the Plugins menu, the Fiji appearance changes as shown in Figure 2.7(a). Afterwards, select at least 5 points on the curved surface shown in Figure 2.7(c), then select the point list option. A window pops out like Figure 2.7(d). Click the "Manual Points Procedure", a fitted circle and eclipsis appear on the original plot as shown in Figure 2.7(e). Another window would pop out as well indicating the angles. We are going to use this method for adhesion angle analysis in chapter 3.3.3.

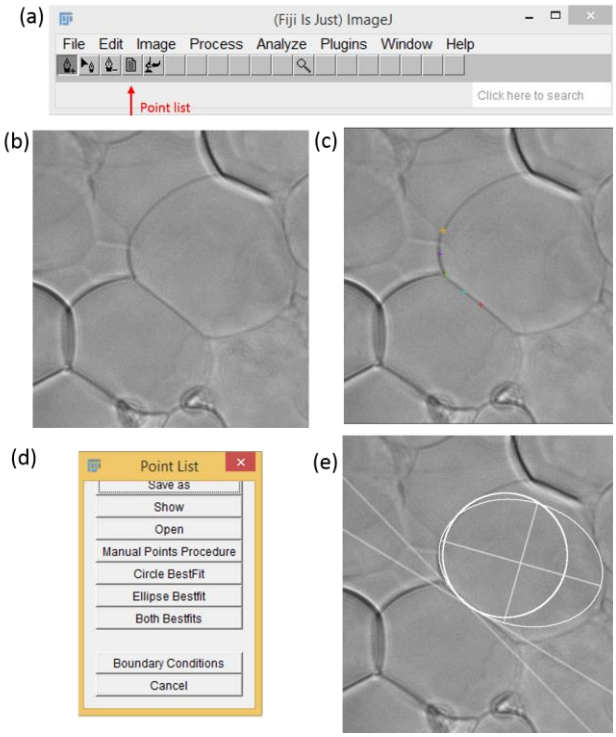

Figure 2.7: (a) Fiji appearance after select Contact Angle plugin. (b) Original image. (c) Select 5 point on the curved surface. (d) The popped window after click point list. (e) Fitted circle and eclipsis.

2.7 Light intensity ratio tracking

In chapter 5.2.4, we reported the light intensity ratio tracking over time on 10% DOPS and 90% DOPC lipid membrane when exposed to nano particles. We used python program to track the several areas on lipid membrane as shown in Figure 5.7. We initially cropped the area (still in video) we are interested in like the double layer region and single layer region as shown in Figure C. After loading each video to the program frame by frame, we located the beginning pixel of the membrane where 5 out of 10 consecutive pixels after the beginning pixel were above a critical value (in my code, I set the critical value as 0.2). This critical value is manually set. Then we took the average pixel value of these 10 pixels as the pixel value on membrane.

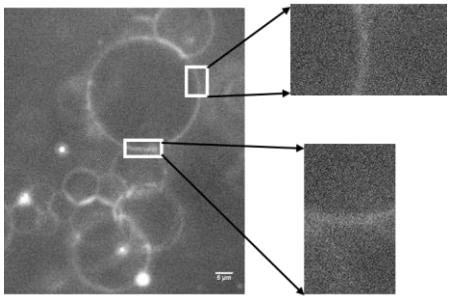

Figure 2.8 : Single layer and double layer region illustration.

The code is shown below:

```
import numpy as np
import cv2
import matplotlib.pyplot as plt
cap = cv2.VideoCapture('double_layer_region.avi') # double_layer_region.avi is the cropped video of the double layer region
intensity_change = np.zeros((711,)) #store the intensity ratio change over time, 711 is the frame number
t = 0
while cap.isOpened():
    ret, frame=cap.read() # frame is loaded
    gray = cv2.cvtColor(frame, cv2.COLOR_BGR2GRAY) #make frame as gray
    length = 130     #some region not used, manually set the length and width
    width = 60
    line_intensity = np.zeros((width, )) # scan pixels row by row
    for i in range(width):
        line= gray[:,i]
        background = np.mean(line[10:40] + line[90:120])/2 # background value is estimated from two ends of the row
        for j in range(55, 80): #scan in a narrower range to find where the membrane begins
            tmp = line[j:j+10]
            #if there are 5 points have light intensity jump, these 10 pixels mark the membrane
            if np.sum((tmp-background)/background>=0.2)>=5:
                line_intensity[i] = np.mean(tmp)/background
                break
    intensity_change[t] = np.mean(line_intensity)
    t+=1
plt.plot(np.arange(len(intensity_change)),intensity_change)
```

Chapter 3

POLYELECTROLYTE INDUCED VESICLE GEL

In this chapter, we discuss the properties of vesicle gels resulting from adhesion caused by addition of oppositely charged polyelectrolytes (polycations). In our experiments, large scale samples of vesicle gels (1 mL) in different polymer concentration were fabricated. We estimated the vesicle-vesicle adhesion strength based on image analysis, finding that the adhesion strength is not monotonic with polymer concentration. We found that vesicle gel could be triggered to release contents by addition of XX-nm silica particles and that the gel formation could be reversed by addition of SDS micelles. We demonstrated that fluorescence solute could rapidly permeate through the interstices of the vesicle gel. The presence of the polycation also significantly enhanced permeability of soluble fluorescein-based dyes through the membrane. At the same time, shear rheology shows that vesicle gel shows a non-zero storage modulus in the low frequency region and the storage modulus does not scale with vesicle size. We attribute the storage modulus coming from the polymer elasticity lying between membranes. The shear rheology of the vesicle gels is compared to emulsions and a membranous web, a combination of small vesicles and peptides [1]. This work provides a potential of drug delivery method and new solid coating material.

3.1 Introduction

Drug delivery is an interesting topic for long time. The material accomplishing the delivery should be able to encapsulate cargo inside and release it at certain position when exposed to certain stimuli. Moreover, the material should be stable enough and able to resist certain amount of physical disturbance. Lipid bilayer membranes which are boundaries to separate inside and outside environment have shown a great potential to serve as trigger-release system because the membrane's permeability can be switched from low to high [23]. The membranes are closed-form in an aqueous environment, leading to a sealed-

object vesicles in which more than 99% weight is simply water. Developing a solid matrix composed of vesicles is therefore a promising approach to controlled-release materials

Recent studies have shown that peptides and large phospholipid vesicles (LUVs) form a gel-like viscoelastic membraneous web, which has a non-zero shear modulus [1]. This work also demonstrated a liquid-liquid to liquid-gel phase transition after addition of the adhering peptide. Recent work by Sarah Zuraw-Weston, Derek Wood, and Ian Torres in the Dinsmore group showed that a combination of SLPC vesicles with either weakly-binding nanoparticles or polycations (poly-L-lysine or polydiallyldimethylammonium chloride (PDADMAC)) led to vesicle-vesicle adhesion and a gel [24].The previous work, however, did not report on the effects of the polymer concentration or vesicle size, nor measure the frequency-dependent rheology or other properties of these gels.

In this chapter, we report a polyelectrolyte induced vesicle-vesicle adhesion based gel which can be fabricated in large scale. Our results show that vesicle gel has non-zero elastic shear modulus (G') at low frequency range and can support localized shear stress for several hours. The measured value of G' varies monotonically with the strength of adhesion between the vesicles, which is tuned by the polymer concentration, c_P. The gel is soft ($G' \sim 2$ Pa) and the shear response remains linear and reversible up to large strain, 70%. For a given adhesive energy between vesicles, we found to our surprise that changing the average vesicle size from about 1 to 10 μm had a negligible effect on G'. The destruction of the vesicles in the gel (and release of their interior) can be trigged by addition of silica nanoparticles that bind strongly to the vesicles and disrupt them. The gelation process is reversed when gel is exposed to SDS micelles. Finally, we found that anionic fluorescein dye can rapidly permeate through the interstices of the gel and that the polycation promotes permeation of the dye across the membrane. We also proved cationic dye Rhodamine-6G still can partition in membranes in the presence of polyelectrolyte. Our work provides the design principles for a new material in which more than 99% of the volume is water but has solid

mechanical response with closed-cell morphology. Vesicle gels could be used as smart coating material that could encapsulate and release sensors or catalysts or other cargo on demand.

In the remainder of this chapter, we first provide the results of our experiments and then discuss them separately, in section 3.4. We end with a brief conclusion.

3.2 Experiment and results

3.2.1 Materials and sample preparation

Materials: To make lipid vesicles, we used a lipid extracted from soy lecithin containing mostly phosphatidylcholine headgroups (PC) (American Lecithin Company, Oxford, CT; Phospholipon 85G). We refer to this lipid as SLPC. It contains 91.5% PC-headgroup lipid, 2.8% Lyso-PC lipid, 1% unspecified nonpolar lipids, 0.3% PE lipid, and few amounts of other non-lipid species. We also used 1,2-dioleoyl-sn-glycero-3-phosphocholine(DOPC) (Avanti Polar Lipids, Alabaster, AL; cat. no. 850375C). For fluorescence imaging, we added 0.1 mol% Lissamine-rhodamine-B-1,2-dioleoyl-sn-glycero-3-phosphoethanolamine(Rh-DOPE, cat. no. 810150P). As the polycation, we used poly(diallyldimethylammonium chloride) solution (PDADMAC, 100k – 200 kDa, 20 wt. % in water), purchased from Sigma-Aldrich (St. Louis, MO, cat. no. 40,901-4). For permeability studies, we used fluorescein sodium salt (Sigma-Aldrich, cat. no. 16,630-8), fluorescein isothiocyanate-dextran(Fl-dextran (average molecular weight 4 kDa) (Sigma-Aldrich cat. no. 46944) and Rhodamine-6G perchlorate (Sigma-Aldrich cat. no. 25-244-1). To probe the response of the gel, we added silica nanoparticles (Ludox AS-30; 11.3-nm radius by dynamic light scattering) (Sigma-Aldrich cat. no. 42,083-2) and sodium dodecyl sulfate (SDS from Sigma-Aldrich cat. no. 436143). In the AS-30 suspensions, powder sucrose was added to achieve 180 mM.

Vesicle preparation. All vesicles were made with sucrose inside and a glucose-sucrose mixture outside. In all cases (except as noted), the osmolarities of the interior and exterior were measured (Vapro pressure osmometer model 5600) and kept at 180 mOsm/L to avoid osmotic stress. Osmolarity

measurements were repeated 3 times and the standard deviation was usually 3-4 mOsm/L. The 10-µm-scale vesicles were made by electroformation mentioned in chapter 2.2.1. The concentration of SLPC stock solution was 100 mg/mL. We combined the results of 5 to 6 repetitions to acquire at least 1.5 mL of concentrated vesicle suspension. To make the 1-µm-scale vesicles, co-solvent method was adapted as described in chapter 2.2.2. We combined the results of 50 repetitions to obtain 6mL of concentrated vesicle suspension. We then waited another 2 h for sedimentation and further collected the 2.5mL vesicle suspension at the bottom, then added 2.5mL sucrose in D_2O (180 mOsm/L). We added D_2O sucrose solution to help vesicles suspend in the upper area. Otherwise, vesicles were highly dispersed.

Mixing vesicles and polycation, forming gels and superparticles. We made a solution of 35 mg/mL PDADMAC stock solution in water with measured osmolarity 180 mOsm/L. This was added to concentrated vesicle suspensions with volume ratio ranging from 0 to 0.2 to tune the polymer concentration c_P. We used a pipette to repeat a mild inject-eject process 20 times to aid mixing. The sample was left on table for approximately 48 h.

Microscopy. The vesicle-polymer mixtures were observed with optical microscopy. Bright field images were acquired using a CoolSnap HQ2 camera (Roper Scientific) and a Zeiss 63× Plan Neofluar objective with 1.4 NA. Confocal images (Visitech International, custom system based on the VTEye) were acquired using a Hamamatsu digital camera C11440 and a Zeiss 63× Plan Neofluar objective(1.4 NA). We used ImageJ [25] to measure sizes and other geometric measures.

Rheology. The rheological experiments were performed on a rheometer AR - G2/AR2000ex/AR1500ex Rheometer from TA instruments. A cone-plate geometry was used, with cone angle 2° and diameter 40 mm. The volume of a typical sample after combining polymer and vesicles was roughly 1 mL. Samples were carefully deposited on the rheometer plate by slowly pouring the gel on the plate and removing the excessive water with absorbent paper. To the eye, the gel appeared homogeneous

white. After loading the sample, we first held the strain amplitude γ_0 fixed at 0.028 and swept the angular frequency ω from 0.1 to 628 rad/s. We then fixed ω = 10 rad/s and varied γ_0 from 10^{-3} to 10.

3.2.2 Vesicle Gel Morphology

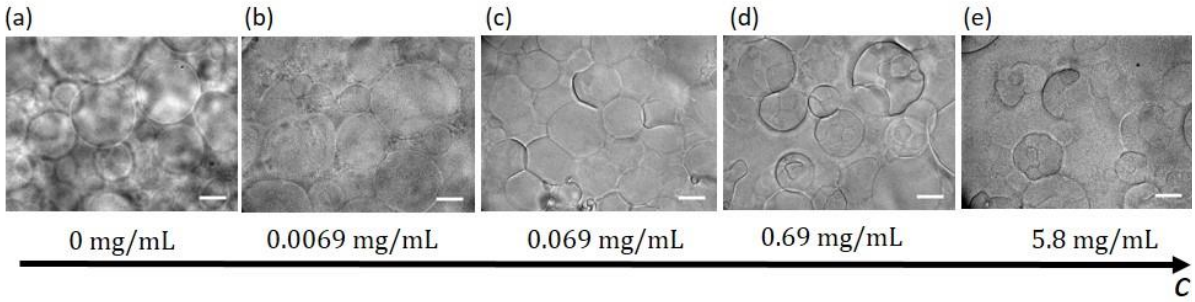

Figure 3.1: 10-μm-scale vesicle morphology dependence on PDADMAC concentration, c_P. In the absence of polymer (a), vesicles are freely suspended. When polymer concentration is relatively low (b), vesicles have weak adhesion; after increasing the concentration (c), adhesion gets stronger; with further increase of polymer concentration (d, e), the adhesion gets weaker again and curved surfaces emerge inside vesicles. Scale bars are 10 μm.

We exposed 10-μm-scale vesicles to PDADMAC solutions at concentrations (c_P) ranging from 0 to 5.8 mg/mL. As described in the chapter 3.2.1, we maintained the same osmolarity (180 mOsm/L) on both sides of the lipid membranes to avoid osmotically stressing the vesicles. Figure 3.1 shows brightfield images of the 10-μm-scale vesicle gel samples acquired 48 hours after preparation. Without added polymer (c_P = 0) as shown in Figure 3.1(a), most of the vesicles were approximately spherical and diffused freely with no vesicle-vesicle aggregation. In the presence of the PDADMAC with $0.0069 \leq c_P \leq 0.069$ mg/mL as shown in Figure 3.1(b, c), we observed well-defined areas of contact between neighboring vesicles, indicating adhesion between vesicles. These are the "vesicle gel" samples. We never saw vesicles spontaneously detach from one another during observation. When 0.69 mg/mL $\leq c_P \leq$ 5.8 mg/mL as shown in Figure 3.1(d, e), we found vesicle-vesicle adhesion plus a new morphology consisting of vesicles

with interior compartments. We refer these new structures as “superparticles” and will discuss them in Chapter 4.

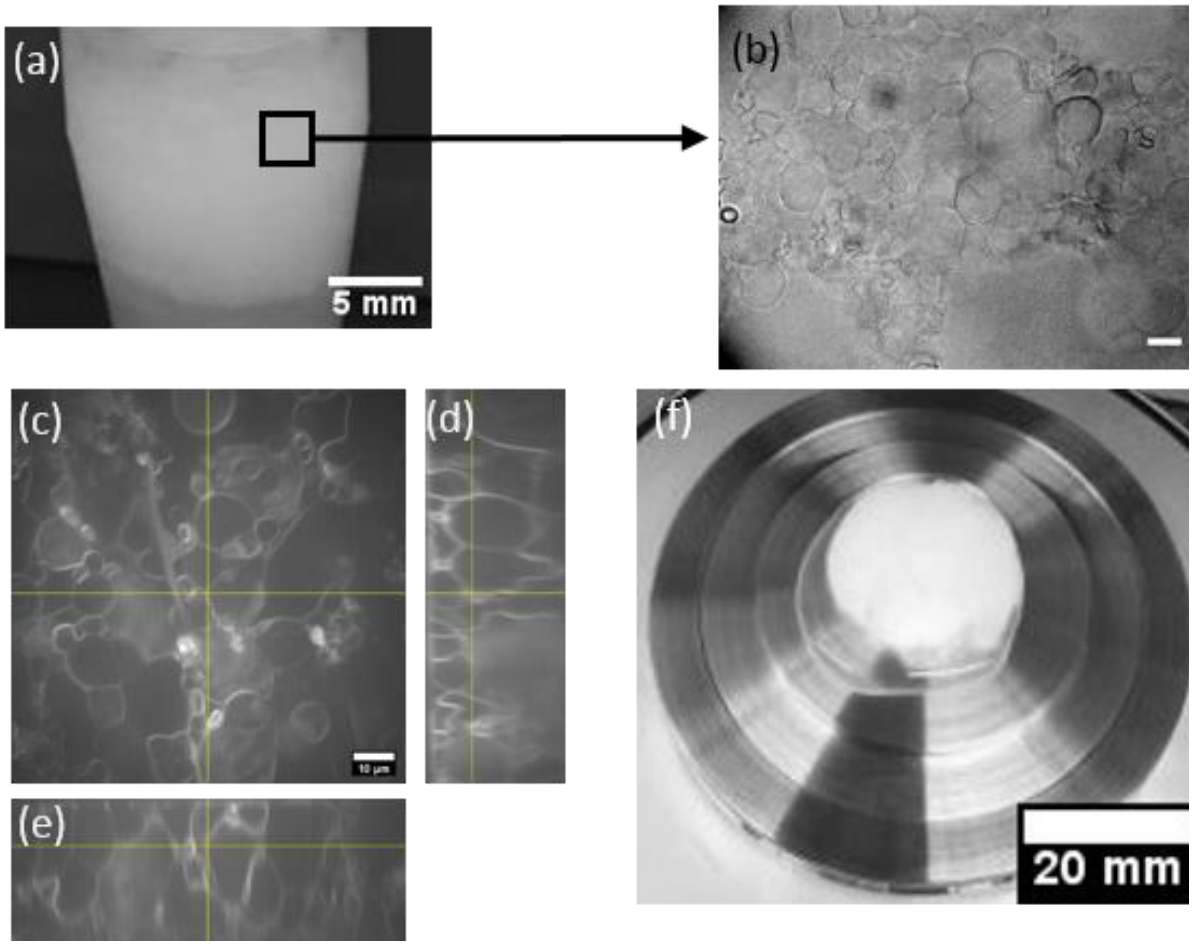

Figure 3.2: (a) Large volume of 10-μm-scale vesicle gels at c_p=0.069 mg/mL. (b) Zoomed image of the large scale vesicle gel. Scale bar is 10 μm. (c), (d), (e)Orthogonal views of gel in three directions. (f) Vesicle gel at c_p=0.069 mg/mL was deposited on rheometer plate.

Taking advantage of the adhesion between vesicles in the presences of PDADMAC, we produced large scale vesicle-gel materials by fabricating large quantities of vesicles. Figure 3.2(a) shows a sample of large volume with c_P = 0.069 mg/mL, 48 h after mixing vesicles with PDADMAC solution. The volume of this gel was approximately 1.0 mL. Figure 3.2(b) is a microscope image of the sample shown in Figure of 3.2(a). Figure 3.2(c, d, e) are confocal images of a fluorescent sample with same c_P, 24 h after mixing vesicles with PDADMAC. This sample had 0.1mol% Rh-DOPE added to label the membranes. Figure 3.2(c)

shows the bottom image of a three-dimensional stack of images. Figures 3.2(d,e) show edge-views of cuts through the center of the imaged volume, indicated by the yellow lines in Fig. 3.2(c). The images show that the vesicle structure was preserved (they form closed volumes), so that the vesicle-gel had a closed-cell morphology.

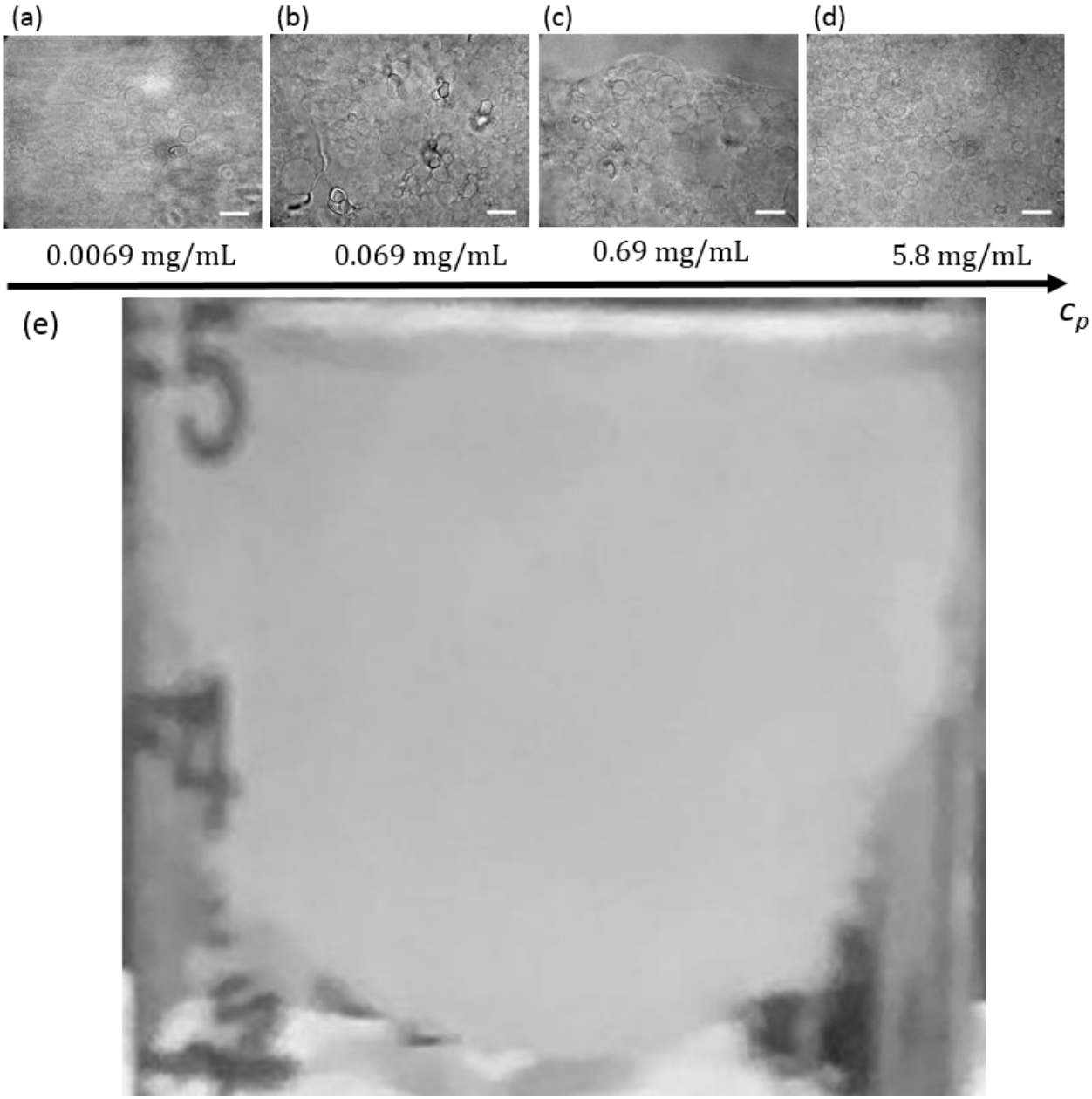

Figure 3.3: 1-μm-scale vesicle morphology dependence on PDADMAC concentration. When polymer concentration is relatively low (a), vesicles have weak adhesion; after increasing the concentration (b, c), adhesion gets stronger; with further increase of polymer concentration (d), the adhesion gets weaker again and curved surfaces emerge inside vesicles. (e) Large volume (roughly 1mL) of 1-μm-scale vesicle gels at c_p=0.69 mg/mL. Scale bar is 10μm.

Like 10-μm-scale vesicle gel, 1-μm-scale vesicle gel has an identical trend as shown in Figure 3.3. When c_P=0.0069mg/mL in Figure 3.3(a), weak adhesions between vesicles were observed. With c_P increasing to the range between 0.069 and 0.69 mg/mL in Figure 3.3(b, c), well-defined contact areas were observed; this was the strong adhesion region. When 5.8 mg/mL ≤ c_P in Figure 3.3(d), the adhesion became weak again. Figure 3.3(e) shows a sample of large scale of 1-μm-scale vesicle gel with volume roughly 1 mL

3.2.3 Vesicle gel properties

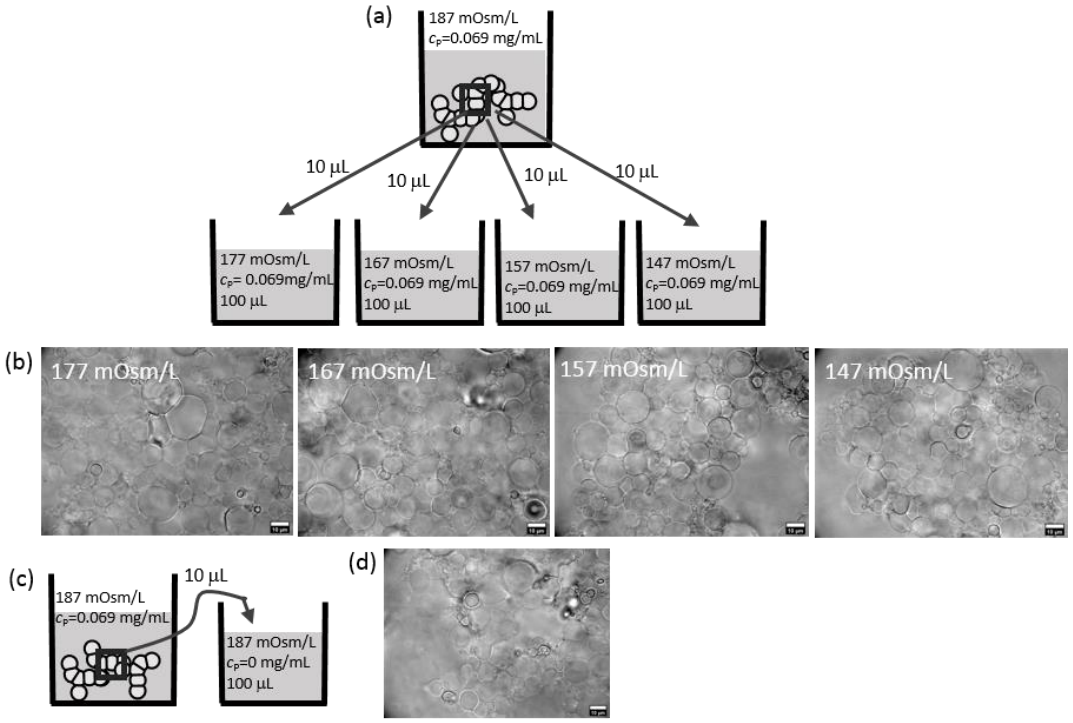

Figure 3.4: (a) Apply osmotic shock to vesicle gel(187 mOsm/L) by depositing 10- m-scale vesicle gel to environment with osmotic pressure as 177, 167, 157, 147 mOsm/L. During this process, no shear applied. (b) Vesicle gel state 48 hours after applied with osmotic shock. Vesicle gel does not break up, still holds as an aggregate. (c) Depositing vesicle gel (c_p = 0.069 mg/mL) in non-polymer environment. During this process, no shear applied. (d) Vesicle gel state after 48 hours deposited in non-polymer environment. Vesicle gel does not breakup.

To test the robustness of the vesicle gel, separately varied c_P and the osmotic stress on the vesicles. First, we put 10 μL gel sample (c_p = 0.069mg/mL, here the osmolarity was 187 mOsm/L) in 1 mL glucose

solution (c_p = 0) with the same osmolarity. The gel did not breakup even though the sample was kept in the reduced-c_P environment for 96 hours as shown in Figure 3.4 (c, d). There was no sign of vesicle-vesicle adhesion weakening as well. We also exposed the vesicle gel to an osmotic shock at constant c_p, by adding 10 μL vesicle gel samples (c_p = 0.069mg/mL, 187 mOsm/L) to 100 μL glucose solutions (c_p = 0.069mg/mL) with osmolarity 147, 157, 167, 177 mOsm/L. No vesicle destruction was observed after 48 hours as shown in Figure 3.4 (a, b). Our result has shown the gel remains intact in non-polymer environment and resists rupture or other detectable degradation under osmotic stress up to ~40 mOsm/L.

To further check the reversibility of vesicle gel, we exposed to vesicle gel to sodium dodecyl sulfate (SDS) micelles. SDS micelles are negatively charged and approximately 4 nm in diameter and have a critical micelle concentration of 8.2 mM at 25 °C [26]. We put 20 μL gel sample (c_p = 0.069mg/mL) in perfusion chamber as shown in Figure 3.5(b), then injected 5 μL osmolarity balanced (180 mOsm/L) SDS micelles suspension (SDS concentration 8.2 mM) to the gel. Our results show that SDS micelles can change the gel structure, by destroying vesicles and compromising vesicle-vesicle adhesion. We observed that some vesicle pairs with clear adhesion surface became free vesicles within 30 s after exposure to SDS micelles as shown in Figure 3.5(c). The experiment was conducted twice, we confirm it is repeatable. These results show that the vesicle gelation process is reversible.

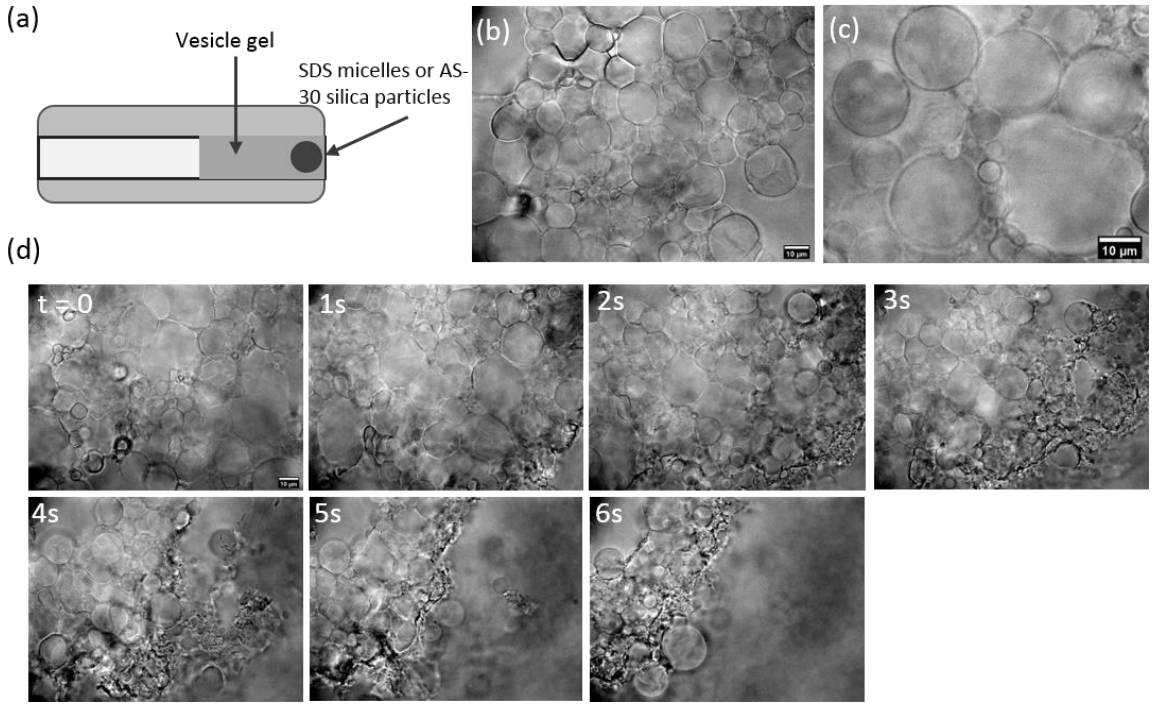

Figure 3.5: (a) Perfusion experiment exposing SDS micelles or AS-30 silica particles to 10-μm-scale vesicle gel. In this process, the osmolarity was balanced. (b) Vesicle gel before exposing to SDS micelles. (c) After gel exposed to SDS-micelles, the adhesion was disappearing and some vesicles ruptured. (d) Vesicle gel destruction process after exposed to AS-30 silica particles. Membranes are squeezed into a compact aggregate within seconds.

To test the release potential of vesicle gel, we exposed to vesicle gel to silica nanoparticles (Ludox AS-30 particles, radius 11.3 nm by DLS). We put 20 μL gel sample (c_p = 0.069mg/mL) in a perfusion chamber, then injected 5 μL osmolarity balanced AS-30 particles (particle concentration 0.1 mM, no dilution, 180mOsm/L) to the gel. The AS-30 particles destroyed almost all individual vesicles and compressed the gel into an aggregated residue within 20 seconds as shown in Figure 3.5(d). We observed more than 90% vesicles were destroyed within 6 s with all residues stuck to one another. We observed this was the typical phenomenon.

3.2.4 Effective adhesion strength

To quantitatively describe the strength of adhesion between pairs of vesicles, we define a dimensionless parameter that we refer to as the effective adhesion strength λ, inspired from previous work [27]:

$$\lambda = \frac{D_c^2}{R_1^2+R_2^2},$$

where R_1, R_2 are the mean radii of two adhered vesicles and D_c is the diameter of the adhesion interface (see inset of Figure 3.6). This quantity is proportional to the ratio of the adhesion area to the mean surface area of the adhered vesicles. R_1, R_2 and D_c were measured from every pair of adhered vesicles with clearly visible radii and adhesion surface. Vesicles in the gel were not always spherical, so for each vesicle, R was taken as the mean of the long and short axes. All the measurements were accomplished with Fiji. For each value of c_P, we made two to three samples, taking 10 to 15 images and measuring a total of 20-40 data points from these images. The mean for each c_p was used to estimate λ, and the error bar is the standard error of the mean.

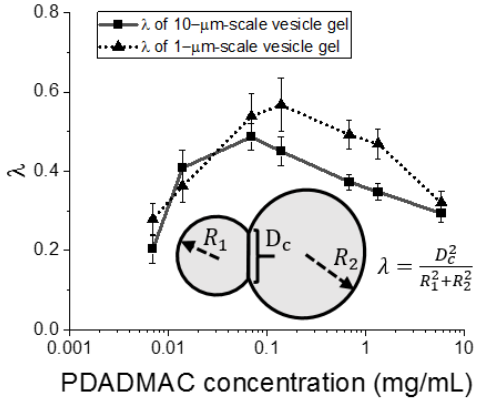

Figure 3.6: Measured effective adhesion strength, λ, *vs*. polymer concentration c_P for 10-μm and 1-μm-scale vesicle gels. Inset: schematic of the definition of λ. R_1, R_2 are the mean radii of two adhered vesicles, D_c is the diameter of the adhered surface. Larger λ means stronger adhesion.

Figure 3.6 shows that λ has a peak for vesicle-vesicle adhesion for both 10-μm-scale vesicle gel and 1-μm-scale vesicle gel. When c_p < 0.2 mg/mL, the area of the adhesion spots increased with c_P, indicating a stronger binding energy between membranes, per unit area. When $c_P \geq 0.69$ mg/mL, we found that the energy of adhesion decreased. We attribute the decrease of λ at high c_P to a dense coating

of PDADMAC on each vesicle, approaching the limit where all vesicles become positive and repulsive. The mechanism for this will be described below.

3.2.5 Shear rheology of the 10-μm and 1-μm-scale vesicle gels

From chapter 1.2, we know that shear rheology is good a tool to judge if a material is solid or liquid. For the vesicle gel, two important factors which could affect the mechanical properties are the polymer concentration c_P and the vesicle size. We begin with a discussion of varying c_P to check the different rheological behaviors between different PDADMAC concentrations.

The mechanical properties of 10-μm-scale vesicle gel were studied with oscillatory shear rheology. To make this gel, we exposed 1.5 mL of concentrated GUV suspension (in 180 mOsm/L sucrose and glucose mixture) to stock PDADMAC solution (35 mg/mL, 180 mOsm/L) under certain volume ratio to achieve different concentrations and mixed the solution uniformly. After resting on a table for 48 h, samples were carefully deposited on the rheometer plate by slowly pouring the gel on the plate and removing the excessive water using absorbent paper. The gel was in white and homogeneity as shown in Figure 3.2(f). After the sample was loaded, we first held the strain amplitude γ_0 fixed at 0.028 and varied angular frequency ω from 0.1 to 628 rad/s. We then fixed ω = 10 rad/s and varied γ_0 from 10^{-3} to 10.

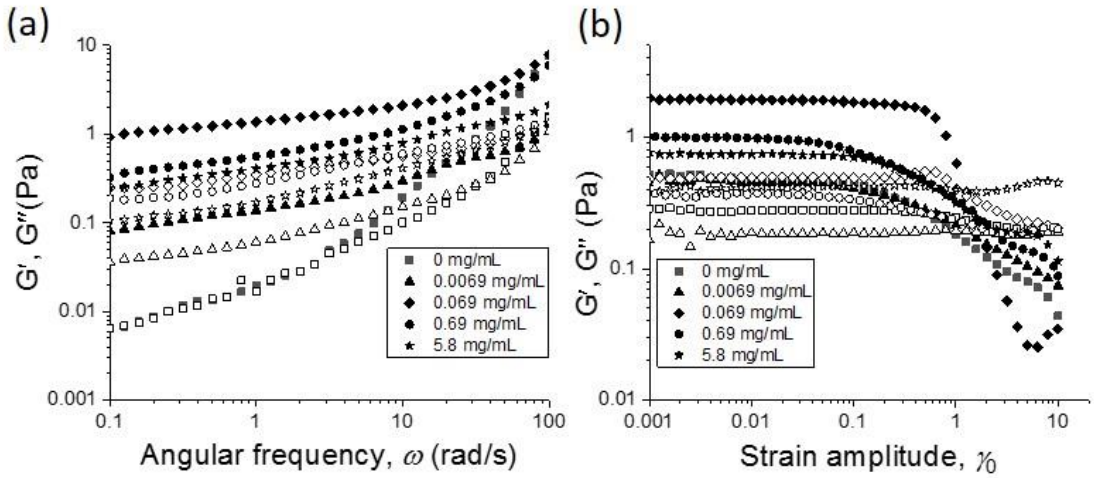

Figure 3.7: Shear rheology of the 10-μm-scale vesicle system with $0 \leq c_P \leq 5.8$ mg/mL. (a) Frequency dependence with strain amplitude $\gamma_0 = 0.028$. (b) Strain-amplitude dependence with frequency $\omega = 10$ rad/s.

Figure 3.7 compares the rheology between concentrated vesicle suspension ($c_P = 0$) and gel with c_P = 0.0069-5.8 mg/ml. Figure 3.7(a) is the frequency sweep with $\gamma_0 = 0.028$. We do not show the data at $\omega > 100$ rad/s, due to the dominance of the rotor's inertia in this regime. The plot shows a typical scan for each c_p. For each c_P other than zero, 2-3 samples were prepared with indistinguishable GUVs (as seen in the microscope) and 2-3 sweeps were conducted for each sample. For a given sample, different sweeps could be a little different but shared the same trend with frequency. There was no systematic difference between each sweep. For a given c_p, different samples had the same trend with frequency, and the amplitude varied as shown by the error bars in Figure 3.8. The concentrated vesicle

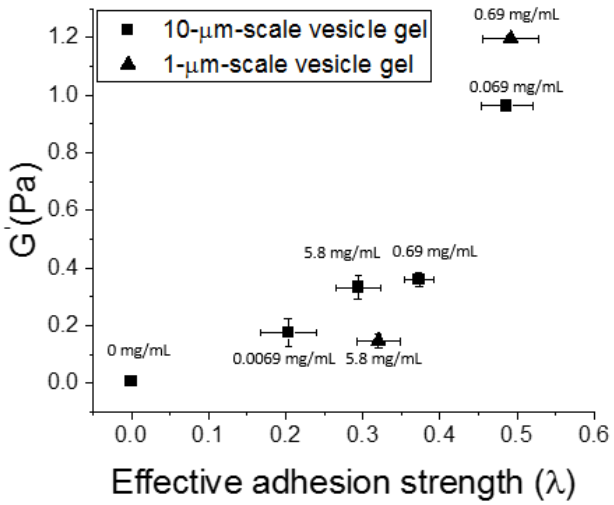

Figure 3.8: Plot of measured G' *vs.* λ for 10-μm and 1-μm-scale vesicle gels at $\omega = 0.1$ rad/s and $\gamma_0 = 0.028$.

suspension (c_p=0) had storage modulus G' near 0.0065 Pa at 0.1 rad/s. In samples with c_P = 0.0069 mg/mL gel, G' fell between 0.08 to 0.3 Pa; for 0.069 mg/ml gel, G' is near 1 Pa, for 0.69 mg/ml gel, G' fell between 0.3 to 0.4 Pa, for 5.8 mg/ml gel, G' fell between 0.2 to 0.3 Pa.

Figure 3.8 shows the measured G' at 0.1 rad/s vs. the measured effective adhesion, λ. We find that although λ depended non-monotonically on c_p, the modulus was a monotonic function of λ. Figure 3.7(b) shows the strain amplitude sweep with ω = 10 rad/s. For gels with c_P = 0.069 mg/ml, the G' had an approximate plateau at a value near 2 Pa, with linear response region extending to $\gamma_0 < 0.7$. For gels formed in other concentrations, the plateau values of G'varied, but the yield strains were all near 0.2.

From the comparison of G' and yield strain in different PDADMAC concentration, we can see gel performance can be tuned by c_p..

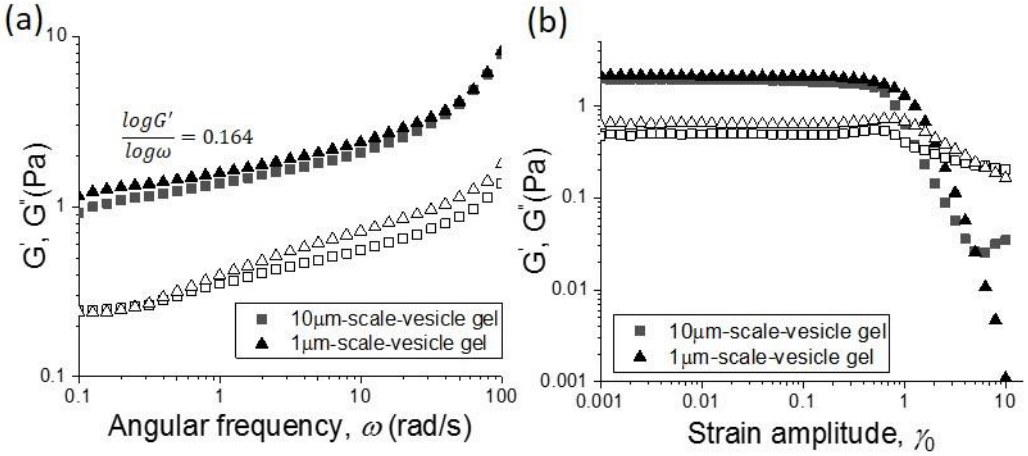

Figure 3.9: Comparison of the shear rheology of 10-μm and 1-μm scale vesicle-gels that have similar λ. (a) Frequency sweep with strain γ_0= 0.028. (b) Strain amplitude sweep with frequency ω = 10 rad/s.

To isolate the effect of vesicle size in determining gel rheology, we selected two different vesicle-gel systems with similar λ. From Figure 3.6, we observed 1-μm-scale vesicle gel with c_p=0.69 mg/mL has close λ to 10-μm-scale vesicle gel with c_p= 0.069 mg/mL. We exposed 2.5 mL of 1-μm-scale concentrated vesicles suspension to 2.5 mL of osmolarity-balanced D_2O sucrose solution and 0.1 mL

stock PDADMAC solution. (We added D_2O sucrose solution to help vesicles float in upper area and increased the vesicle concentration). The 1-μm-scale vesicle gel microscopic image is shown in Figure 3.3(c, e). After 48 h, we followed the same procedure of the shear rheology measurement as we did for 10-μm-scale vesicle gel.

Figure 3.9 has the frequency dependence and strain amplitude dependence of 10-μm-scale (c_P = 0.069 mg/mL, λ = 0.48±0.03) and 1-μm-scale (0.69 mg/mL, λ = 0.49±0.03). These concentrations were chosen to obtain similar λ. In Figure 3.9(a), we can see the 10-μm-scale vesicle gel with PDADMAC concentration 0.069 mg/ml has G' near 1 Pa in low frequency region (<10 rad/s) while 1-μm-scale vesicle gel in 0.69 mg/mL has G' near 1 Pa as well. For the strain amplitude dependence in Figure 3.9(b), G' for both of them had a plateau near 2 Pa and decreasing modulus for strain amplitude above 0.7. In summary, the 1-μm-scale and 10-μm-scale gel had indistinguishable rheology.

Figure 3.9(b) shows G' *vs.* λ for 10-μm-scale and 1-μm-scale vesicle gels. It is clear to see that G' has positive correlation with λ: gel with higher λ has higher G'. We conclude that G' scales with λ, not with c_P. From comparing our 10-μm-scale and 1-μm-scale vesicle gels, we conclude that G' does not scale with vesicle size for a given λ.

3.2.6 Copper beads held by vesicle gel

To explore if vesicle gel has shear modulus at zero frequency (and not just at the rheometer's low-frequency limit of 0.1 rad/s), we put 300 μL vesicle gel (c_p=0.069 mg/mL) in vial, then let copper beads (average diameter 300 μm, density 8.96 g/cm^3) fall on gel as shown in Figure 3.10(a). We kept recording the positions of each bead and observed that both beads and gel displaced with time as shown in Figure 3.10(b). We used a python program (in chapter 2.5) to track the displacement of gel and a selected copper bead that was not close to the surface of the vial. The displacement of gel and bead are shown in Figure 3.10(c, d) respectively. We observe that both gel and the selected bead were falling, which demonstrated

that the bead and gel formed one unit with density higher than sugar solution. The relative displacement between gel and the selected bead is shown in Figure 3.10(e). Figure 3.10(f) shows the relative displacement in the first 10 hours.

We observed that the displacement showed a poor fit over 10 hours to a linear trend (R^2 value 0.145 which represents an insignificant linear relation), Therefore, given the insignificant linear trend, we conclude that the gel acted as an elastic material in the timescale of approximately 10 h. Our experiments by far has shown vesicle gel indeed is a solid at very low frequency or long times.

In control experiments with no polymer, we found that a concentrated vesicle suspension cannot support copper beads. Therefore, the discovery in Figure 3.10 is significant.

In the long time scale (> 10 h), we saw the bead suddenly sediment within the gel. The reason could be due to the gel yield slow dissolution of copper from the bead or reduction/oxidation reactions at the copper surface, which could reduce the electrostatic double layer adhesion between polycations and the membrane, leading to local yield of the gel

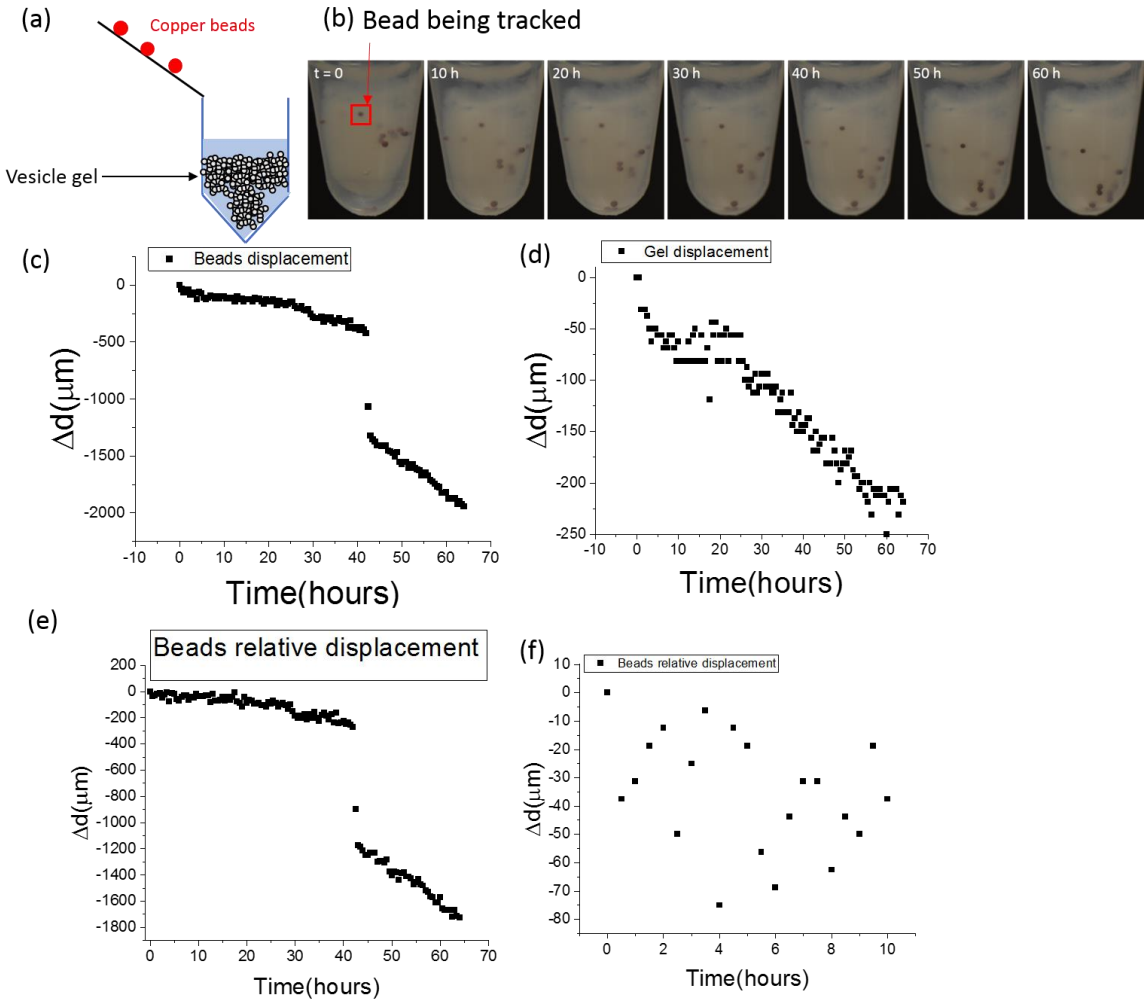

Figure 3.10: (a) Illustration of Beads' drop on vesicle gel with momentum. (b) Time evolution of beads' positions on gel. Both gel and beads moved downwards. (c) Relative displacement of the bead. (d) Relative displacement of gel. (e) The relative displacement of bead towards gel. (f) The relative displacement and its linear fitting in first 10 hours.

3.2.7 Solute permeability of vesicle-gels

The vesicle gel provides an exciting potential to act as a barrier to protect a surface from a solute. Although there is no single membrane across the entire sample, the close adhesion between neighboring vesicles might serve to prevent solute transport. In order to explore if the vesicle-gel material can serve as a macroscopic barrier, , we used a confocal fluorescence microscope to image the membrane (Rh-DOPE, excitation wavelength 532 nm) and the dye (fluorescein sodium salt, excitation wavelength 442 nm) separately.

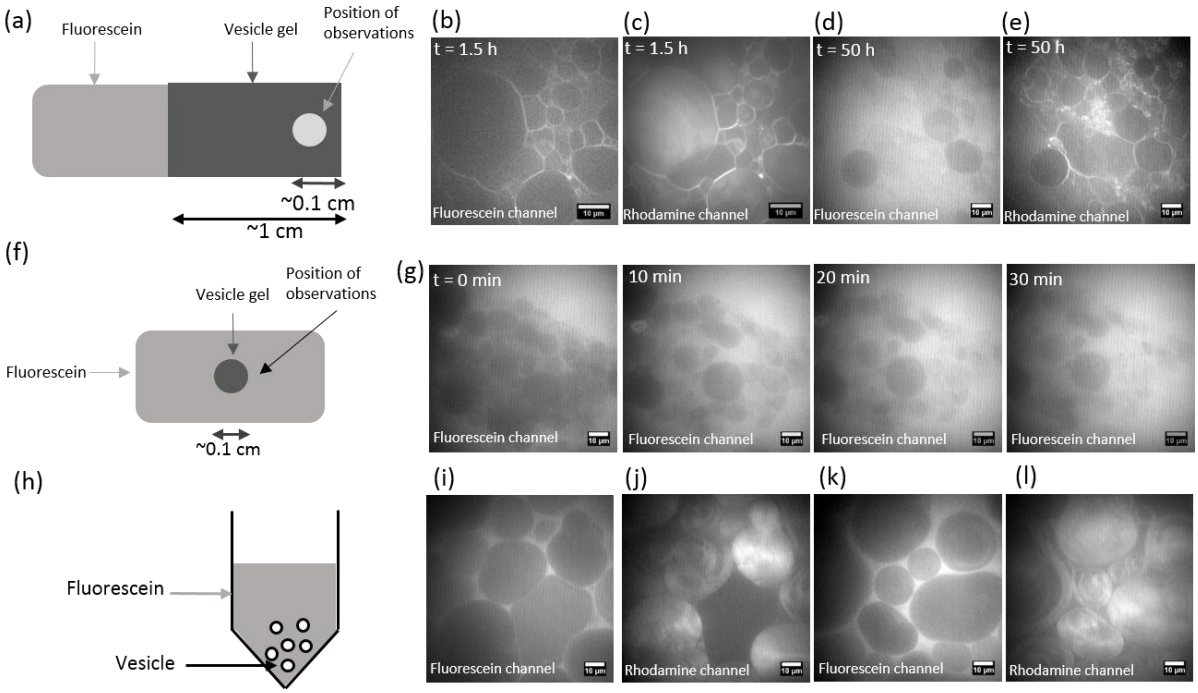

Figure 3.11: Fluorescein permeates along the surfaces of membranes within the vesicle gel. (a) Schematic plot of permeation experiment chamber. Fluorescein solution and vesicle gel were placed contiguous to each other, and the observation position was far from dye end. (b,c), (d,e) are 2 pairs of images. Each pair shows the same location with one taken under 442 nm excitation and the other one under 532 nm excitation. (b, c) were taken 1.5 h and (d, e) were 50 h after chamber was sealed. (f) Schematic plot of permeation of gel surrounded by fluorescein solution. (g) Permeation process of a vesicle gel sample (442 nm excitation). (h) Schematic plot of leaving free vesicles in fluorescein solution. (i, j, k, l) are two pairs of images, with each pair showing the same location under 442 nm and under 532 nm. Both pairs were taken 53 hours after immersion in fluorescein. Images were taken under confocal microscopy.

We placed 40 μL osmolarity-balanced fluorescein solution, contiguous to a 40 μL vesicle gel sample, letting dye diffuse to the gel region, and sealed them it a chamber as shown in Figure 3.11 (a). The gel was made with 10-μm-scale GUVs doped with 0.1% Rh-DOPE with excitation wavelength 532 nm and c_P = 0.069 mg/mL. Fluorescein solution is 0.001 mM (180 mOsm/L) with c_P = 0. Figure 3.11(b, c), (d, e) are 2 locations in the observation region after 1.5 h and 50 h, respectively. Our confocal images in Figure 3.11 (b, c) show fluorescein near the membrane, indicating that fluorescein can permeate on the membranes (along the membrane surfaces) to our observation region within 2 h. However, we saw no green fluorescence from inside the vesicles, indicating that that fluorescein did not permeate through the membrane. After 50 h, fluorescein did permeate through (across) membranes as shown in Figure 3.11(d, e), in which some vesicles were indistinguishable from the environment. Roughly 75% of vesicles were permeated by fluorescein. Figure 3.11(f) illustrates a different experiment, in which the vesicle gel sample was much smaller and surrounded by 50 μL fluorescein solution. In this case Figure 3.11(g) shows significant permeation of the dye through (across) the membranes within 30 min. Our control experiment is illustrated in Figure 3.11(h): we exposed 5 μL free SLPC vesicle suspension in 50 μL 0.001 mM fluorescein solution (180 mOsm/L); c_P = 0. After 53 h, no obvious fluorescein penetration was observed as shown in Figure 3.11(I, j) and 3.11(k, l). Therefore, PDADMAC can enhance the ability of fluorescein (sodium salt) to permeate across the SLPC lipid membrane.

To find out how PDADMAC concentration affects fluorescein penetration, we monitored fluorescein permeation through DOPC membrane (doping 0.1% Rh-DOPE) under c_p = 0, 0.00069, and 0.0069 mg/mL as shown in Figure 3.12(a). Here we used the synthetic DOPC rather than the mixed-composition extract SLPC in order to see whether an undefined component of the SLPC played an important role. We mixed 100 μL DOPC vesicle suspension and 100 μL 0.001 mM osmolarity balanced fluorescein solution, add 0, 0.004, 0.04 μL PDADMAC stock solution (180 mOsm/L) in vials, then observed in a perfusion chamber like

Figure 3.11(f, g). Due to the low c_p, vesicles were dispersed. Figure 3.12(b) represents the time dependence of fluorescein penetration under different c_p. We did not see fluorescence for any c_p in the first two hours. But after 2.5 hours, we saw clear fluorescence inside vesicles with c_p = 0.0069 mg/mL, and no obvious light inside vesicles for $c_p \leq$0.00069 mg/mL even after 27 hours. Our results showed that trans-membrane permeability to the dye can only be affected when c_p reaches a threshold of approximately 0.0069 mg/mL.

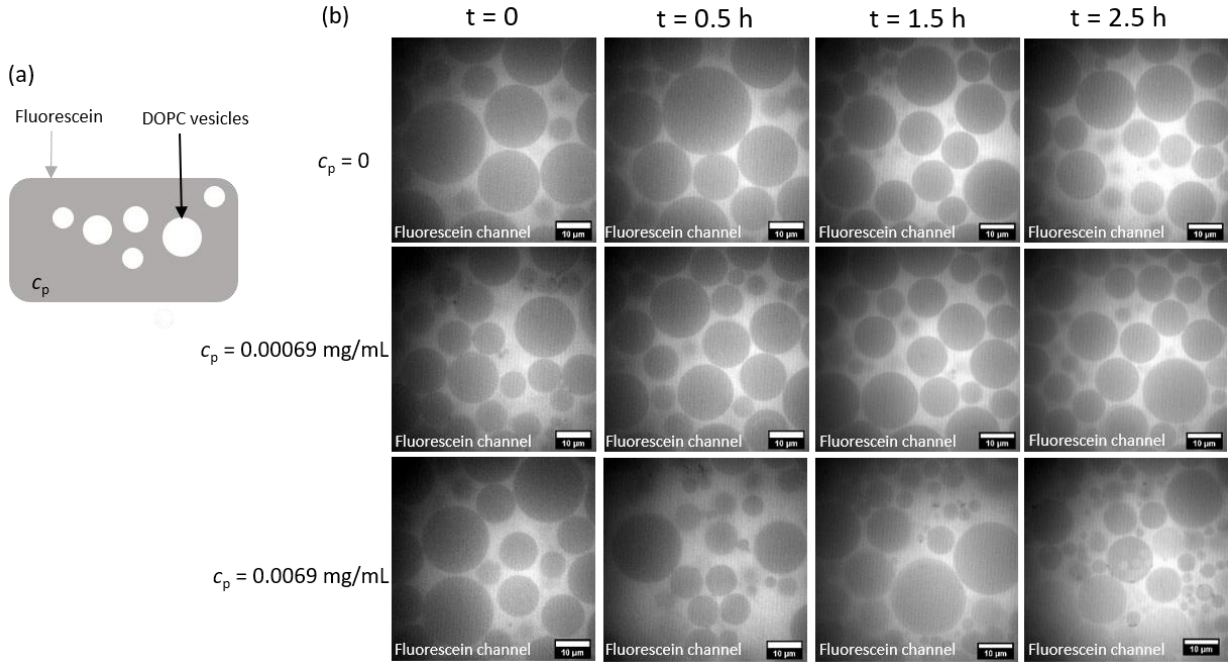

Figure 3.12: (a) DOPC vesicles (0.1% Rh-DOPE doped) mix with osmolarity balanced fluorescein solution under c_p = 0, 0.00069 mg/mL, 0.0069 mg/mL. (b) Time dependence of fluorescein penetration through DOPC membrane under different c_p. At 2.5 h, vesicles under c_p =0.0069 mg/mL were penetrated by fluorescein. Images were taken under confocal microscopy.

We investigated whether molecular size plays a role in the penetration through the membrane. We tried Fluorescein-dextran (FITC-dextran, average molecular weight 4000, same excitation wavelength as fluorescein). We sealed 60 μL osmolarity balanced FITC-dextran solution (0.52 mM with glucose added, c_p = 0) contiguous with 30 μL SLPC vesicle gel (c_p =0.069 mg/mL) in a chamber like Figure 3.13(a). After 24

hours, clear fluorescence was seen in the interior of some vesicles as shown in Figure 3.13(b, c) and (d, e), we observed 13.5% vesicles were penetrated after 24 h. Therefore, fluorescein-dextran can permeate through (across) the membrane as well, in the presence of PDADMAC.

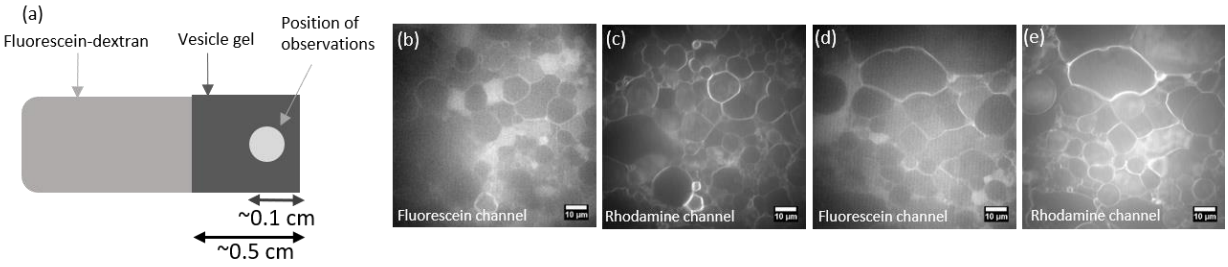

Figure 3.13: (a) Schematic of the experiment to monitor permeation of fluorescein-dextran in vesicle gel. Fluorescein-dextran and vesicle gel were placed contiguous to each other and theobservation position was far from the dye end. (b,c), (d,e) were 2 pairs of confocal images. Each pair shows the same location with one taken under 442 nm excitation and the other one under 532 nm excitation. Both pairs were taken 24 hours after chamber was sealed.

After seeing the penetration of dye through membrane, we investigated whether salt could affect the permeation. We deposited 5 μL vesicle gel (c_p = 0.104 mg/mL) in 50 μL fluorescein-dextran solution (0.52 mM, 180 mOsm/L, c_p = 0, and 50 mM NaCl) as shown in Figure 3.14(a). After 24 h, we observed vesicles were almost indistinguishable from the environment and very significant trans-membrane permeation happened: more than 90% of vesicles were penetrated by fluorescein-dextran as shown in Figure 3.14(b, c) and (d, e). In the absence of salt, we found only 13.5% of vesicles were penetrated by fluorescein-dextran after 24 h, so we conclude that salt significantly promotes the permeation through membranes.

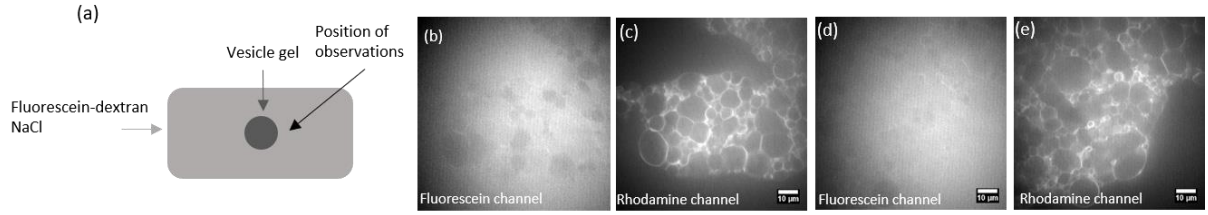

Figure 3.14: Fluorescein-dextran permeates on vesicle gel in the existence of salt. (a) Schematic plot of permeation of gel surrounded by fluorescein-dextran . (b,c), (d,e) were 2 pairs of confocal images, each pair shows same location with one taken under 442 nm and the other one under 532 nm. Both pairs were taken 24 hours after chamber was sealed.

Given that anionic dye can permeate through lipid membranes under the existence of PDADMAC, we then investigated whether cationic dye can permeate as well. We selected Rhodamine-6G perchlorate (same excitation wavelength as Rh-DOPE) as the solute for the permeation experiment. In control experiments, we mixed 20 μL SLPC or DOPC vesicle suspension (180 mOsm/L) and 20 μL 0.1 mM Rhodamine-6G perchlorate solution (180 mOsm/L). The results show that Rhodamine-6G can permeate on and through SLPC and DOPC lipid membranes within 10 min in the absence of PDADMAC as shown in Figure 3.15(a, b). Then we sealed 60 μL 0.1 mM Rhodamine-6G perchlorate solution and 40 μL 10–μm-scale vesicle gel (c_p = 0.069 mg/mL) in a chamber like Figure 3.13. Rhodamine-6G permeates along the lipid membranes through the gel 1 h after dye and gel were put together as shown in Figure 3.15(c). (Fluorescence is clearly visible in the region of the membrane.) After 24 hours, some vesicles were penetrated by Rhodamine-6G, as shown in Figure 3.15(d). Therefore, PDADMAC cannot stop Rhodamine-6G permeation as well. Given the hydrophobicity of the Rhodamine 6G, it is possible that the dye strongly partitioned into the hydrophobic domain of the lipid bilayer. Indeed, in Figure 3.15 (a), the fluorescence inside the multi-vesicular vesicles appears to be membrane-associated.

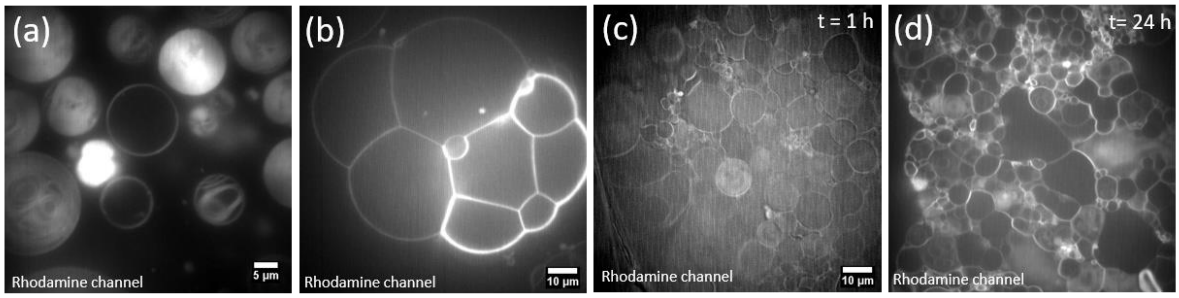

Figure 3.15: (a) Rhodamine-6G permeates on and through free SLPC vesicles. (b) Rhodamine-6G permeates on and through free DOPC vesicles. (c) Rhodamine-6G permeates on and through SLPC vesicle gel (c_p = 0.069 mg/mL) 1 hour after put contiguous. (d) Rhodamine-6G permeates on and through SLPC vesicle gel (c_p = 0.069 mg/mL) 24 hours after put contiguous.

3.3 Discussion

3.3.1 Vesicle gel properties discussion

The physical essence of vesicle-vesicle adhesion comes from the electrostatic interaction. Although the SLPC head is zwitterionic like DOPC, we also believe that it is slightly negatively charged in aqueous environment, like DOPC [6]. The electrostatic interaction can drive PDADMAC to bind to membranes. The double layer interaction described in chapter 1.3.1 pushes two vesicles closer together. So when two vesicles adhered, PDADMAC in fact lay between two vesicles and bridged them, causing vesicle-vesicle adhesion as shown in Figure 3.16(a, b).

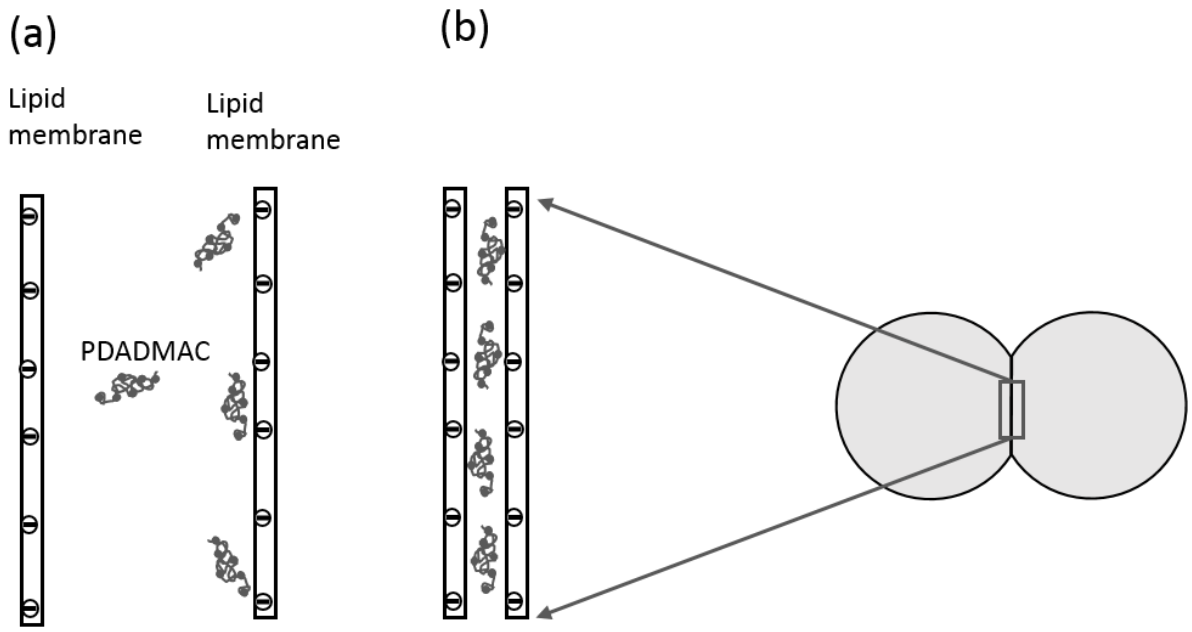

Figure 3.16: (a) PDADMAC binds to SLPC membrane due to electrostatic interaction. (b) PDADMAC lies between two membranes and induces vesicle-vesicle adhesion.

The destruction triggered by the AS-30 particles can be explained by the strong binding energy, which leads to wrapping of the particle by the membranes and increasing of membrane lateral tension. The high tension finally causes the vesicle rupture [24]. We believe the mechanism is same as the work of Zuraw-Weston, et al, but here the adhesion energy between anionic particles and anionic membrane is due to polycation.

The gel cannot be easily reversed by diluting the polymer owing to the strong binding energy between PDADMAC and lipid membrane. The time scale requiring to reverse gel might be several orders larger than the reported time here (96 hours). However, our result shows adding SDS does cause rapid breakup, which we attribute to SDS forming complexes with the PDADMAC [28], and therefore rapidly removing it from the vesicle surfaces. Some of the vesicles are also compromised, which we attribute to incorporation of some of the lipids into surfactant micelles or vice versa [29].

We attribute the anionic dye (fluorescein, FITC-dextran) permeation along the surfaces of the lipid membrane to diffusion. The electrostatic interaction between PDADMAC and the anionic fluorescein dye should enhance the concentration of dye in the regions between the vesicles, thereby enhancing permeability through the interstices of the gel [30]. The permeation through (across) the lipid membrane on the other hand is attributed to the membrane stretching after PDADMAC binds, which we propose enlarges the nanometer-scale gaps between lipid molecules and allows dye to penetrate through. For the cationic dye (Rhodamine-6G), we attribute the dye permeation to the hydrophobicity, since Rhodamine-6G might be hydrophobic even it is water soluble.

3.3.2 Physical origin of shear modulus

Shear rheology has shown the gel which is >99% water has G' of a few pascals in the low-frequency region. Here we discuss what physical parameters could affect the modulus of the gel.

We found that λ does not have a monotonic relationship with c_p from Figure 3.7(a). When c_p is low, the adhesion energy per area between membranes increases with c_p, which leads to stronger adhesion between vesicles; after c_p reaches a certain point, polymers are excessive so the membranes can be over coated, the adhesion energy per area then decreases. Figure 3.17(a) shows our illustration of our proposal.

For the shear modulus, comparing with modulus induced from stretching modulus ($K_{stretch}/R \sim 10^4 Pa$) or bending modulus ($\kappa/R^3 \sim 10^{-4} Pa$), the vesicle gel G' is far off. So during the shear, the membrane elasticity may not contribute to G' and there might be some component of the system that is softer and therefore sets G'. PDADMAC bridges vesicles together, so the gel can relax the strain by deforming the polymers rather than stretching or bending the membrane as shown in Figure 3.17(b). Lee et al reported a vesicle-biopolymer gel fabricated with surfactants (cetyl trimethylammoniumtosylate and

sodium dodecyl benzene sulfonate) and polymer chitosan (190 – 310k Da). They found their gel had G' near 50 *Pa*, they also attributed the origin of G' to the polymer bridging effect over vesicles [31].

Ho, et al reported a membranous web formed with DOPC/POPC vesicles (100 – 200 nm) and 4BAH2 (H-WRTLEAFWAKHMWNFIS- GIQYLA-NH2) peptide (340−690 μM). They found the membranous web had G' 50x greater than our gel (100 *Pa*). The interaction energy as measured by adhesion angles (described below) is similar, but the driving force is different from our gel. They speculated hydrophobic force was the driving force causing vesicle-vesicle adhesion, which could be much stronger than the electrostatic interaction between lipid membranes and polyelectrolyte.

In the frequency sweep, our result shows that there is a slow increase of G' with ω. which appears to have a power-law behavior with an exponent approximately 0.16. One possibility is due to a slow polymer relaxation process. When the shear frequency is getting higher and higher, PDADMAC cannot follow the shear frequency by relaxing itself back forth to compensate the strain, which in turn increases the elastic potential of polymer. Meller, *et al*. reported with emulsions in micro scale with depletion (G' ~ 100 Pa) have close slope at 0.18 (polymer concentration 2 mg/mL; poly(ethylene oxide), 900 kDa) [32] [33] [34]. For both the depletion experiments and our polymer-based adhesion experiments the product of the polymer relaxation time and the frequency of the applied shear may be the relevant control parameter. The long-time compliance experiment indicates that there really is a plateau modulus at low frequency.

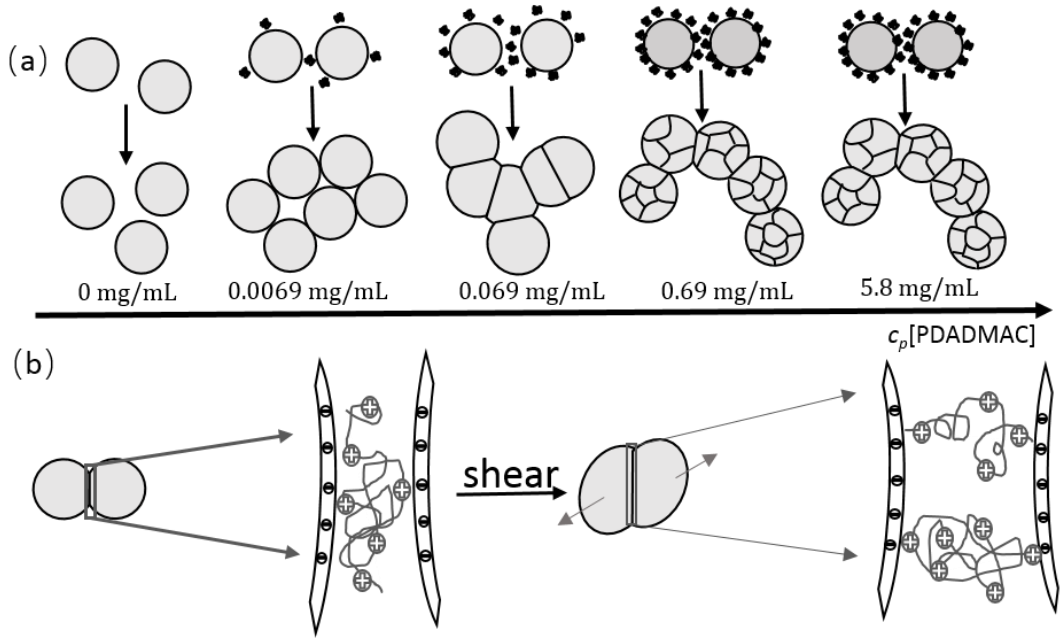

Figure 3.17: (a) Vesicle adhesion *Vs* PDADMAC concentration illustration. (b) The illustration of shear applied to vesicle gel.

There is a peak of G'' when the vesicle gel yields. The peak resembles that found in emulsions [35]. Here, however, the yield strain values are much higher than found in compressed emulsions, where the yield strain depends on volume fraction and did not exceed 0.14. We attribute the peak in G'' to energy dissipated by peeling back membranes, which then reattach with a distorted shape.

From Figure 3.8(b), we conclude there is a positive correlation between G' and λ, and a faster-than-linear increase. This resembles the behavior of colloidal silica gels with attraction strength induced by depletion attraction [36]. We attribute to the increase of *G*' to the growth of correlation length (or vesicle-cluster size) as well as stiffening of individual vesicle-vesicle bonds. In emulsions, Aben, *et al.,* also measured *G*' vs polymer concentration (depletion strength) and conclude a linear dependence but the data actually suggested faster than linear [37]. They found that the measured modulus was about 100x smaller than predicted from the stiffness of inter-droplet adhesive bond and the expected structural correlation length, which they attribute to heterogeneity in the gel.

3.3.3 Adhesion energy estimation

Given that vesicle gel performance does not scale with vesicle size, we propose that *G*' is determined by the adhesion energy per area, w divided by a characteristic length of the vesicle gel system. The characteristic length could be a mesoscopic one, coming from a correlation length or cluster size as pointed out by Aben, *et al*., and summarized in the previous paragraph. Now a natural question comes: how do we estimate the adhesion energy per area *w*?

In the chapter 3.2.4, we characterized the strength of inter-vesicle adhesion by λ, which is effectively the relative area taken up by individual adhesion patches between adjacent vesicles. Here we consider a different measure of adhesive strength: the angles between the adhesive region and the free regions next to the adhesive patch. From these angle measurements, we can calculate the ratio of adhesive energy per area (*w*) to the mean tension in the two vesicles. We can then estimate the tension using some assumptions.

The definitions of the angles are shown by the schematic diagram in the Figure 3.18(a). The angles were measured using the same samples as described in chapter 3.2.4. In general, the shape of the vesicle is set by a combination of *w*, tension τ, and bending modulus κ. Generally, the bending modulus affects the membrane shape over small scales and the stretching energy and tension affect it over large scales, with a cross-over length scale given by $L = (\kappa / \tau)^{1/2}$. The values of τ in giant vesicles can range from μN/m range (in vesicles that are subjected to a weakly hyperosmotic suspension and are visibly floppy) to a few mN/m (which is the tension at which vesicles lyse). These values correspond to *L* in the range of 300 to 10 nm. In our samples, the tension is likely to be in the mN/m scale in the gel, given that we never see the thermal undulations. Our measurements of membrane shape are therefore made at length scales larger than *L* and therefore dominated by τ rather than κ. In this regime, the membrane shape can be viewed as a balance of *w* vs. τ. If we describe the two vesicles as having different tensions τ_1 and τ_2, then we find that

$$\tau_1 \sin\theta_1 = \tau_2 \sin\theta_2$$

and

$$w = \tau_1(1 - \cos\theta_1) + \tau_2(1 - \cos\theta_2).$$

If we now define $\tau_{\text{mean}} = \frac{1}{2}(\tau_1 + \tau_2)$, then we find

$$\frac{w}{\tau_{\text{mean}}} = 2\,\frac{\sin\theta_1 + \sin\theta_2 - \sin(\theta_1+\theta_2)}{\sin\theta_1 + \sin\theta_2}. \qquad \text{Eq. (3.1)}$$

Figure 3.18(b) shows the values of w/τ_{mean} measured from the angles and using Eq. (3.1) for individual vesicles, the angles θ_1, θ_2 were acquired through the adhesion angle measurement described in chapter 2.6. The mean value for each c_P, shown as the red symbols, show a trend of rising and then falling with c_P. This trend is very like the trend of $\lambda(c_P)$, discussed shown in Figure 3.6. The peak value of w/τ_{mean} is approximately 0.2. To extract a value of w, we need to make an assumption about the mean tension. The most likely result is a tension in the mN/m scale, close to the maximum tension that can be sustained prior to lysis. Assuming, therefore, a tension of 1 mN/m, we infer $w = 2\times10^{-4}$ J/m^2 or 5×10^4 $k_BT/\mu m^2$. Since each lipid molecule occupies about 70 Å^2 in each membrane, this reduces to approximately, $w = 0.04$ k_BT per pair of lipid molecules.

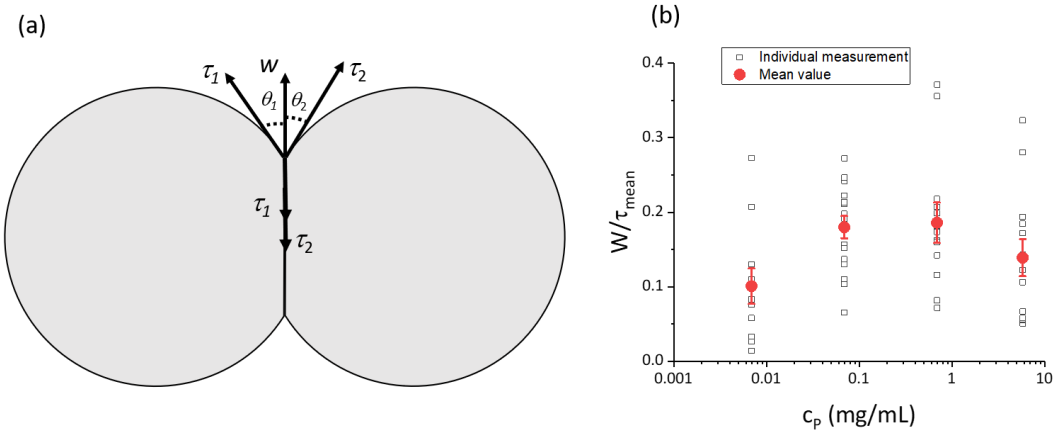

Figure 3.18: (a) Illustration of membrane tension τ_1, τ_2, θ_1 and θ_2. (b) Plot of measured w/τ_{mean}

The ratio of w/G' may be interpreted as a length scale in the system. For c_P = 0.069 mg/mL, we estimate w/G' as (2×10^{-4} J/m^2)/2Pa = 100 μm, or approximately 10 times the particle size. Such a large length indicates that long-range correlations in the sample (finite-sized clusters of vesicles, or regions of weak adhesion or voids) may make the measured modulus substantially lower than might be expected from the single-vesicle-scale interactions. In prior work on emulsions and particle gels made with attractive interactions (such as by Aben *et al*., discussed above), similar comparisons have also shown G' substantially less than expected from single-particle-scale interactions.

3.4 Conclusion

In this chapter, we reported vesicle gel formation induced by PDADMAC. The driving force is the double layer interaction induced vesicle-vesicle adhesion, which we can use make large scale gel composed of vesicles. Our results show that the vesicle gel can withstand osmotic shock up to ~40 mOsm/L, keep adhesion strength after the polymer is diluted by a factor of 100, reverse the adhesion process by addition of SDS micelles, and release internal cargo by addition of anionic silica nanoparticles. Shear rheology measurement and copper beads holding experiment show the gel is a solid with non-zero shear modulus with linear shear response up to 0.7 strain amplitude. Finally we showed that PDADMAC can dramatically increase the membrane permeability to anionic or cationic fluorescent dyes.

In future work, it will be interesting to look at gels induced by particles. The attractions could be depletion or electrostatic. Given that particles cannot relax strain and that they are expected to form in-plane structures that may be rigid, we expect either membrane stretching or particle detachment would be dominant during the shear process, which might lead to a higher G'.

Chapter 4

CONCENTRATED POLYELECTROLYTE INDUCED MEMBRANE DEFORMATION – SUPERPARTICLES

In this chapter, we discuss a new membrane morphology: unlike ordinary multilamellar vesicles, this new structure consists of an outer spherical membrane with highly curved inner compartments that partition all of the interior volume. We refer this special morphology as superparticles. Examples of superparticles were shown in chapter 3, Figure 3.1 (d,e). in this chapter, we provide the details and show that superparticle formation is due to reorganization of the inner membranes in multilamellar vesilces. When the outside PDADMAC concentration is lowered, we found that the outside membrane of superparticles cannot hold the inside compartments and we observed vesicles escaping from the inside of the original vesicle. We show that superparticles can only form under high PDADMAC concentration and the threshold concentration is dependent on PDADMAC molecular weight.

4.1 Introduction

Owing to the fluid membrane property, lipid membranes can change shape with high degree of freedom. So far, this thesis has mainly focused on unilamellar vesicles, which have a single lipid bilayer. In many cases, though, samples contain multilamellar vesicles that have many (likely up to thousands) bilayers that are stacked to make a thicker outer membrane. In addition, we routinely find “multivesicular” vesicles, which by definition have vesicles encapsulate within them (and which might or might not be multilamellar). Because of the excess area within multilamellar vesicles, there is a vast room for new kinds of membrane morphology when the vesicles are exposed to stimuli. As a practical matter, one might simply want to extract the interior lamellae in the form of new unilamellar vesicles. Alternatively, it would be interesting to design more complex morphologies.

For unilamellar vesicles, the range of possible structure is broad. In chapter 1.1.1, we described how lipid membranes can be charged based on the lipid composition; in chapter 1.1.2, Helfrich

Hamiltonian (Eq. 1.1), we described that osmotic pressure can play an important role in membrane morphology. Therefore, many stimuli can cause membrane deformation by electrostatic interaction (vesicle gel in chapter 3), osmotic pressure or depletion force etc. Previous studies, for example by Deserno, *et al*., has shown theoretical and simulation work on particle-membrane interaction [18], indicating the membrane bending and particle-membrane adhesion energy competition decides the microscopic membrane geometry modification. Zuraw-Weston, *et al*., demonstrated the morphology transition from vesicle-vesicle adhesion to vesicle rupture by tuning membrane electrostatic interaction with nano particles [24]. Oglecka, *et al*., induced reminiscent membrane morphology transformation with osmotic shock [38]. All of these works illustrate the application potential by triggering membrane morphology transition.

In this chapter, we present a novel membrane morphology referred as "superparticles". We found superparticles formed when multilamellar vesicles were exposed to highly concentrated PDADMAC solutions with balanced osmotic strength. The distinct feature of a superparticle is the highly curved inner compartments, which appear to completely fill up the interior volume. We demonstrated that inner compartments originated from reorganization of the interior lamella. We also showed that superparticles have release potential when PDADMAC concentration in environment was lowered. We further found the critical concentration of superparticle formation was lower in the presence of PDADMAC with higher molecular weight. We attribute the superparticle formation to the penetration of PDADMAC into vesicles, coating the inner membranes, and inducing electrostatic repulsion and delamination.

4.2 Experiments and results

4.2.1 Materials and sample preparation

Materials: To make lipid vesicles, we used SLPC described in chapter 3.2.1. For fluorescence imaging, we added 0.1 mol% Lissamine-rhodamine-B-1,2-dioleoyl-sn-glycero-3-phosphoethanolamine(Rh-DOPE, cat. no. 810150P) and 0.1 mol% 1,2-dioleoyl-sn-glycero-3-

phosphoethanolamine-N-7-nitro-2-1,3-benzoxadiazol-4-yl (NBD-DOPE, cat. no. 810145P). We used a molar concentration as 0.1 mol%. As the polycation, we used 3 kinds of poly (diallyldimethylammonium chloride) solutions (PDADMAC) in different molecular weight (MW). First one: MW 100k – 200 kDa, 20 wt. % in water, cat. no. 40,901-4, lot. no. 02101CA, we refer it as type 0 PDADMAC stock solution; second one: MW<100k Da, 35 wt. % in water, cat. no. 52-237-6, lot. no. MKCJ9009, referred as type 1 PDADMAC stock solution; third one MW 400k -500k Da, 20 wt. % in water, cat. no. 40-903-0, lot. no. MKCF6920, as type 2 PDADMAC stock solution. All PDADMAC were purchased from Sigma-Aldrich (St. Louis, MO). Note, however, that the batches that were used in the present chapter are, in many cases different from the batch used in the previous chapter, The reasons for this will be discussed below.

Vesicle preparation. All vesicles were made with sucrose inside and a glucose-sucrose mixture outside. In all cases, the osmolarities of the interior and exterior were measured (Vapro pressure osmometer model 5600) and kept at 180 mOsm/L to avoid osmotic stress. Osmolarity measurements were repeated 3 times and the standard deviation was usually 3-4 mOsm/L. The vesicles were made by electroformation mentioned in chapter 2.2.1. The concentration of SLPC stock solution was 100 mg/mL.

Mixing vesicles and polycation, forming gels and superparticles. We made PDADMAC stock solutions in water with measured osmolarity 180 mOsm/L. This was added to concentrated vesicle suspensions with volume ratio ranging from 0 to 0.6 to tune the polymer concentration c_P. We used a pipette to repeat a mild inject-eject process 20 times to aid mixing. The sample was left on table for approximately 48 h.

Microscopy. The vesicle-polymer mixtures were observed with optical microscopy. Bright field images were acquired using a CoolSnap HQ2 camera (Roper Scientific) and a Zeiss 63× Plan Neofluar objective with 1.4 NA. Confocal images (Visitech International, custom system based on the VTEye) were acquired using a Hamamatsu digital camera C11440 and a Zeiss 63× Plan Neofluar objective(1.4 NA). We used ImageJ [25] to measure sizes and other geometric measures.

4.2.2 Superparticle morphology

From chapter 3.2.2, we know that at the two highest values of PDADMAC concentration(c_P) that we studied (100k – 200 kDa, c_P = 0.69 and 5.8 mg/mL using batch), we found vesicle-vesicle adhesion plus a new morphology consisting of vesicles with interior compartments Figure 3.1(d,e) shows examples of these structures, which we call "membrane superparticles." These superparticles have a well-defined exterior membrane (like a particle) with a characteristic interior structure consisting of membrane-defined compartments. In diameter, superparticles ranged from 10 to 50 μm.

Considering that the interior compartments consume membrane area, we would like to figure out where the excessive membranes come from. We mixed 10 μL Rh-DOPE doped (0.1 mol%, emit light under Rhodamine channel), 10 μL NBD-DOPE doped (0.1 mol%, emit light under FITC channel) and 80 μL normal SLPC vesicles together. Then we exposed 20 μL of type 0 PDADMAC stock solution (100k – 200k Da, 35 mg/mL, 180 mOsm/L) to the mixed vesicle suspension. After 48 hours, we observed the superparticle morphology under bright field and fluorescent microscopy as shown in Figure 4.1(a, b, c). Figure 4.1(a) shows the superparticle morphology under bright field; Figure 4.1(b, c) present superparticle emitting fluorescence under Rhodamine and FITC channel respectively. The two fluorescent vesicles in Figure 4.1(b, c) are adjacent as shown in Figure 4.1(a) but each only emits fluorescence under one channel, which means each superparticle is labeled by a unique fluorescent lipid. After reviewing more than 30 regions, we did not observe any superparticles emitting light under both fluorescent channels in our experiments. Therefore, the superparticle inner membranes come from the original vesicle itself.

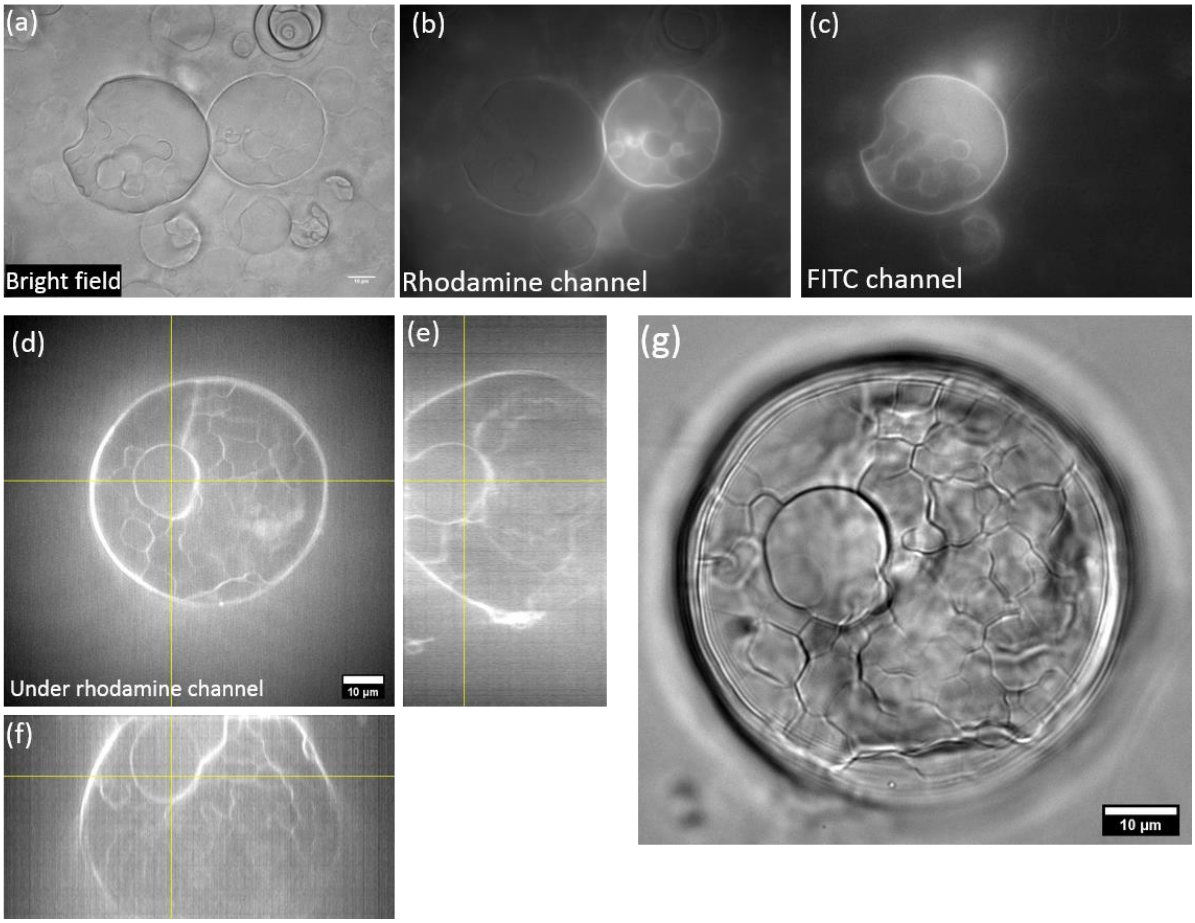

Figure 4.1: (a, b, c) Superparticle (Type 0 PDADMAC, 100k – 200k Da, c_p=5.8 mg/mL) image under bright field, rhodamine channel and FITC channel. A single superparticle can only have one fluorescence. (d, e, f) Confocal images of orthogonal views of a superparticle from 3 directions. (g) The superparticle in (d, e, f) under bright field.

Figure 4.1(d) shows the bottom image of a three-dimensional stack of confocal microscopic images. Figure 4.1(e,f) show edge-views of cuts through the center of the imaged volume, indicated by the yellow lines in Figure 4.1(d). Figure 4.1(g) shows the same superparticle in Figure 4.1(d, e, f) under bright field. We can see the inner compartments are in closed-form. These images also show that the outer membrane is still brighter than the inner membranes, indicating that the outermost membrane surface remains multilamellar.

4.2.3 Superparticle formation and release

To find out the superparticle formation process, we exposed 100 mL vesicle suspension to 20 mL type 0 PDADMAC stock solution (100k – 200k Da, 35 mg/mL, 180 mOsm/L) and mixed them uniformly. 30 mL of the mixed suspension were withdrawn and sealed in a glass chamber to prevent water evaporation. The chamber was then placed under bright field inspection and images were recorded. The whole process is shown in Figure 4.2(a). In Figure 4.2(a), at t = 0, the inner side of vesicles were still clean, with no noticeable structure. After 5 h, there were some compartments appearing clearly and at 10 h the interiors of the vesicles had many compartments. These compartments came from reorganization of the inner side membranes reorganization. We confirm the formation process in Figure 4.2(a) is typical.

Our results indicate superparticles' inner compartments originate from inner membranes. That is to say, only multilamellar vesicles can become superparticles. To prove our hypothesis, we fabricated unilamellar vesicles through electroformation after decreasing the SLPC stock solution to 10 mg/mL (as compared to the 100 mg/mL used for the other experiments in this chapter). The yield contained almost no multilamellar vesicles, judging by the spherical shape and low contrast seen in optical microscopy. Then we followed the same procedure described in chapter 3.1 to raise type 0 PDADMAC (100k – 200k Da) concentration to 5.8 mg/mL. We observed no superparticle formed afterwards. Therefore, only multilamellar vesicles can form superparticle. The membrane area consists of inner compartments belongs to the excessive inner membrane area.

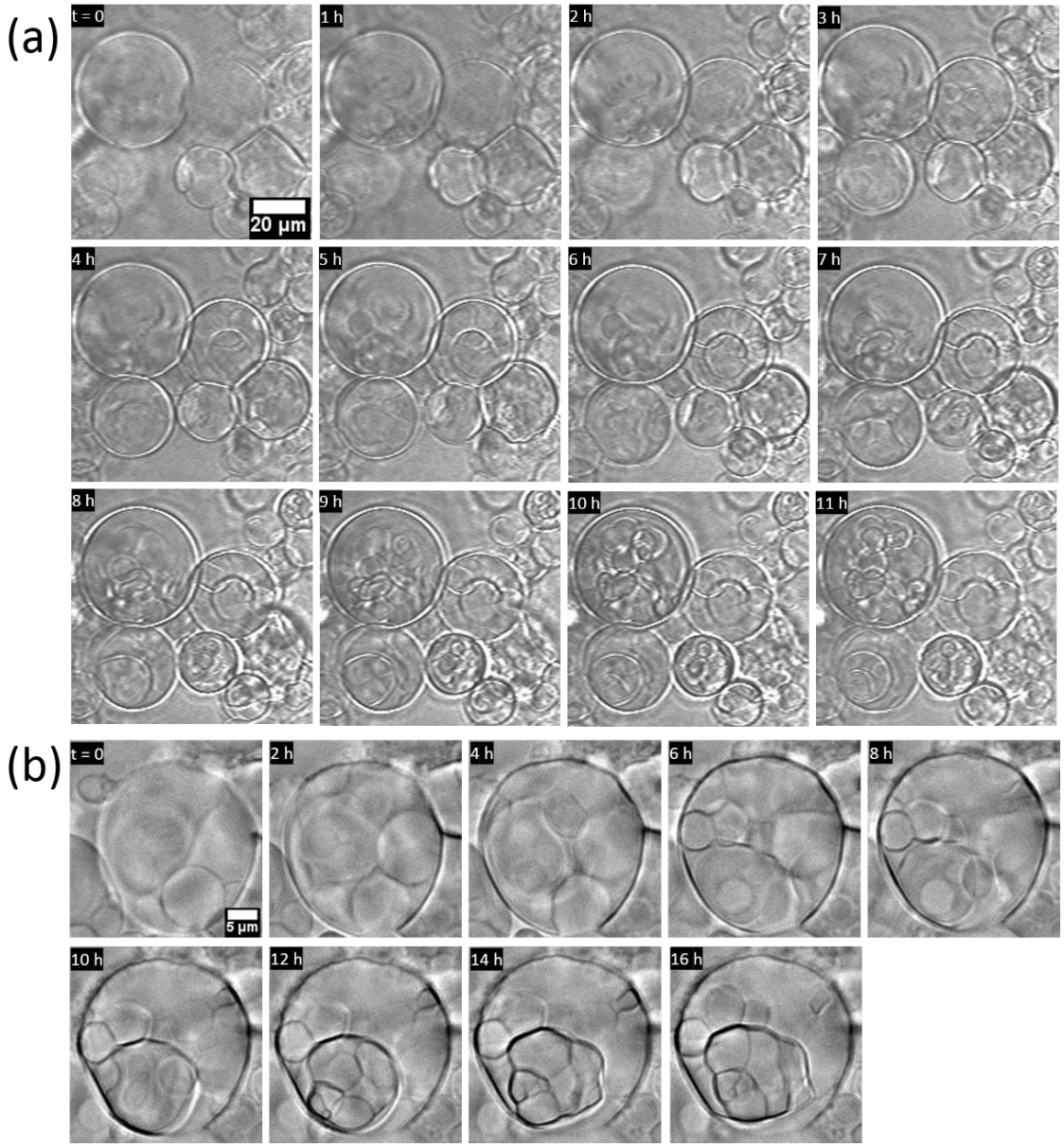

Figure 4.2: Superparticle inner compartments formation process of (a) type 0 PDADMAC (100k – 200k Da, c_p decreased from 5.8 mg/mL to 0.58 mg/mL) and (b) type 2 PDADMAC (400k – 500k Da, c_p decreased from 28 mg/mL to 2.8 mg/mL).

In order to explore if the formation process is reversible, we mixed 10 μL of type 0 PDADMAC induced superparticle suspension (180 mOsm/L, MW 100k – 200k Da c_P = 5.8 mg/mL) and 100 μL 180 mOsm/L glucose solution(c_p = 0) to decrease the polymer concentration outside the superparticles. After mixing uniformly, we withdrew 30 μL diluted superparticle suspension and sealed it into a glass chamber. Our results show that the inner side compartments popped out after PDADMAC concentration decreased, as shown in Figure 4.3(a). In Figure 4.3(a), initially the superparticle had a spherical shape, and the inner membranes slowly popped out within 4 minutes and the superparticle shape was gradually changing as well. Then the whole process appeared to accelerate and the outside membrane no longer could hold the inner compartments after 5 minutes. Because the PDADMAC concentration (c_p = 0.53 mg/mL after dilution) outside was moderate, the popped membranes still adhered with one another and formed a vesicle gel. The whole release process took several (10 – 20) minutes and the release happened within one hour after c_p decreased.

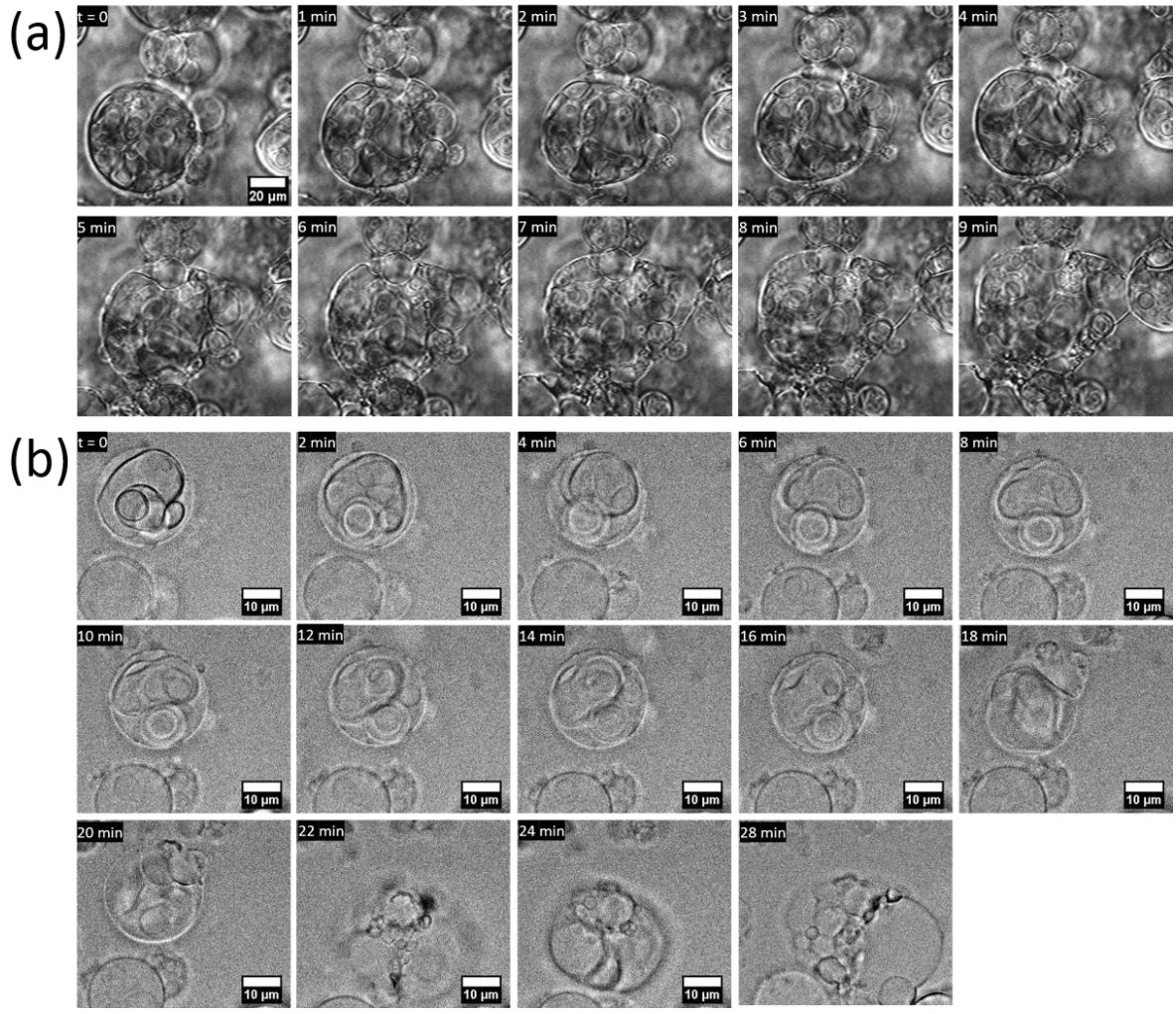

Figure 4.3: Superparticle inner compartments release process of (a) type 0 PDADMAC (100k – 200k Da, c_p = 5.8 mg/mL) and (b) type 2 PDADMAC (400k – 500k Da, c_p = 28 mg/mL).

From the release experiment in Figure 4.3(a), we know that superparticles can transform to vesicle gel after c_p decreases. We also would like to find out if the transformation depends on the sequence of polymer addition. We initially uniformly mixed 100 μL with 0.2 μL type 0 PDADMAC stock solution (MW between 100k – 200k Da, 35 mg/mL, 180 mOsm/L) to achieve 0.069 mg/mL. After being left on table for 24 hours, vesicle gel was formed as shown in Figure 4.4 (b). Afterwards, 19.8 μL type 0 PDADMAC stock solution was further added to the vesicle gel sample with gentle mixture and no shear of the gel as shown

in Figure 4.4(a). Waiting another 24 hours, we observed superparticle formed in the sample in low frequency (roughly 1 out 50).

Because the superparticle formation is reversible upon dilution, and the formation appears to be the same whether c_P is raised in a single step or in two steps, we conclude that the superparticle formation is not a kinetically limited process. Later in this chapter, we will discuss our proposed mechanism.

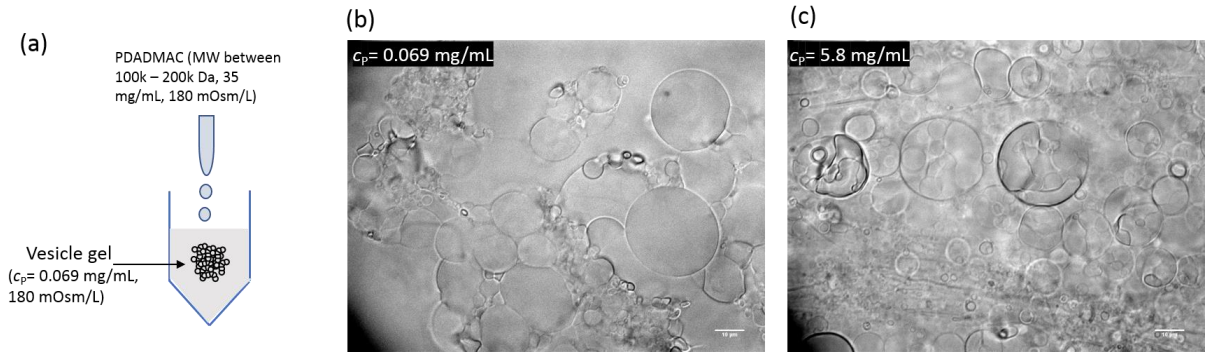

Figure 4.4: (a) Schematic plot of the experiment process to increase c_P. (b) Vesicle gel morphology before increasing c_P, showing a gel without superparticles. (c) Superparticles formed after c_P increased.

4.2.4 Molecular weight dependence of superparticle formation

After observing the properties of superparticles, we would like to understand if the PDADMAC molecular weight (MW) plays a role in superparticle formation. For this study, we purchased two additional lots of PDADMAC. In addition to the PDADMAC with type 0 PDADMAC stock solution (MW between 100k – 200k Da), we prepared the type 1 PDADMAC stock solution (MW < 100k, 43.6 mg/mL, 187 mOsm/L) and type 2 PDADMAC stock solution (MW between 400k – 500k Da, 57.0 mg/mL, 181 mOsm/L). (It is worth noting that PDADMAC is not homogeneous, therefore even following the same dilution ratio the osmolarity could be a little variant. But the concentration order is correct.) We then mixed these PDADMAC solution with varying volumes of 180 mOsm/L glucose solutions to obtain different c_P with approximately the same osmolarity. We mixed SLPC vesicle suspension with type 1 or type 2

PDADMAC stock solution uniformly in different volume ratios to achieve c_P = 0.7, 7, 14, and 28 mg/mL. The mixture was then left on table for 48 hours. The resulting vesicle morphology is shown in Figure 4.5.

When 0.7 mg/mL ≤ c_p ≤7 mg/mL, both type 1 and type 2 PDADMAC stock solution cannot induce superparticle formation. When c_p = 14 mg/mL, type 2 PDADMAC began to induce superparticles formation at low frequency (1 out 50) while type 1 did not induce superparticle formation at all. When c_p = 28 mg/mL, superparticles with typical morphology were induced by type 2 PDADMAC while type 1 still could not lead to superparticles. We can see the critical concentration to induce superparticle formation for type 2 PDADMAC is 14 mg/mL, but type 1 PDADMAC cannot induce superparticle formation as far as we know yet. The superparticles induced by type 2 PDADMAC (400k – 500k Da, c_p = 28 mg/mL) formation process is shown in Figure 4.2(b). The procedure was almost the same as that of Figure 4.2(a) except the vesicle suspension volume ratio. At t = 12 hours, clear compartments with sharp edges were detected. We also confirmed that type 2 PDADMAC induced superparticle also had release potential after c_p was lowered at factor of 10. The release process illustrated in Figure 4.3(b) whose procedure was same as that of Figure 4.3(a). The internal compartments popped out of the outside membrane and adhered with each other. For reasons described below, we believe that the threshold for the lower-MW PDADMAC lies at higher c_P than we can achieve with this osmolarity. Therefore, there is a molecular weight dependence on superparticle formation.

There is a confusing point here: the threshold concentrations of superparticle formation for type 0 PDADMAC (MW 100k – 200k Da) and type 2 PDADMAC (MW 400k – 500k Da) are 0.69 mg/mL and 14 mg/mL respectively. There is an order difference in the critical concentration. Right now, we are not very clear regarding this confusion. It could be due to the polymer molecular weight heterogeneity or the stock solution purity when the manufacture synthesized it.

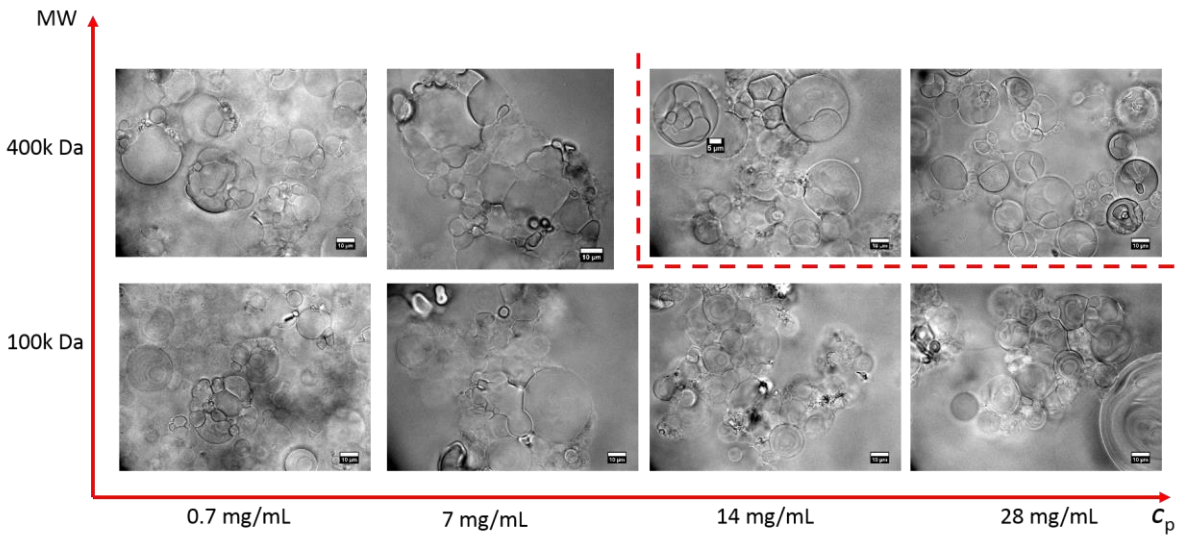

Figure 4.5: PDADMAC MW dependence on superparticle formation

Though we did not find closed compartments for type 1 PDADMAC (MW <100k Da), we did observe typical irregular internally curved vesicle structure as shown in Figure 4.6(a). Unlike normal multilamellar vesicles which is concentric, the internal structure is curved. To test if it is releasable, we mixed 10 μL the irregular suspension (c_p = 35 mg/mL, 180 mOsm/L) with 90 μL glucose solution (180 mOsm/L). We found the inner structure was released as shown in Figure 4.6(b). The irregular spherical object released its internal membranes within 50 minutes.

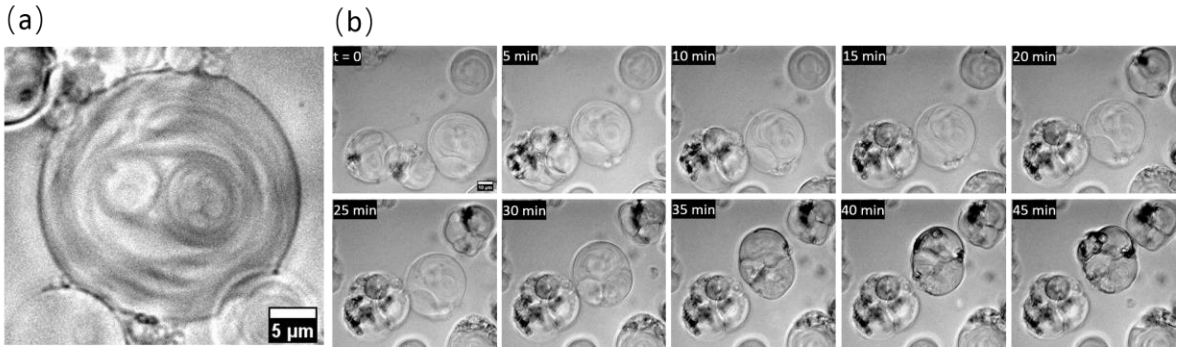

Figure 4.6: (a) Irregular membrane structures induced by type 1 PDADMAC (MW<100k Da, c_p = 35 mg/mL). (b) The releasing process of the irregular membrane structures (c_p was lowered from 35 mg/mL to 3.5 mg/mL).

4.2.6 Osmotic shock effect on superparticle formation

In order to explore the effect of osmotic stress on superparticle formation, we mixed type 1 PDADMAC (MW <100k Da, 43.6 mg/mL, 187 mOsm/L), type 2 PDADMAC (MW 400k – 500k Da, 57 mg/mL, 181 mOsm/L) solution with SLCP vesicle suspension in the presence of osmotic shock. We prepare a glucose solution in 458 mOsm/L, then mixed it with type 1 and type 2 PDADMAC solutions in different volume ratios to achieve 205 mOsm/L and 225 mOsm/L. Then we mixed the PDADMAC sucrose mixture solution with SLPC vesicle suspension (185 mOsm/L) in different volume ratios to achieve 7, 14 and 28 mg/mL. The results are shown in Figure 4.7 and 4.8. Figure 4.7(a) and Figure 4.8(a) show the schematic plot of mixing type 1 and type 2 PDADMAC solutions to SLCP vesicle suspension in the presence of osmotic shock. Both Figure 4.7(b) and 4.8(b) show no significant difference comparing to the results in the absence of osmotic shock. Therefore, osmotic shock does not affect superparticle formation.

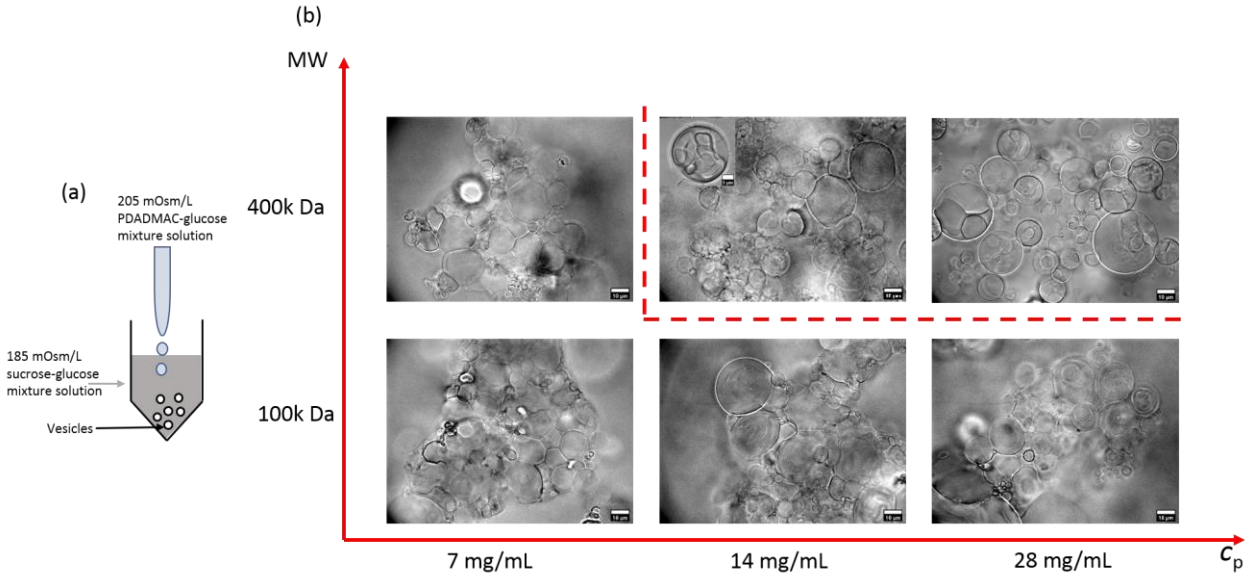

Figure 4.7: (a) Schematic plot of mixing SLPC vesicle suspension with 205 mOsm/L type 1 and type 2 PDADMAC solutions. (b) PDADMAC MW dependence on superparticle formation in the presence of 20 mOsm/L osmotic shock.

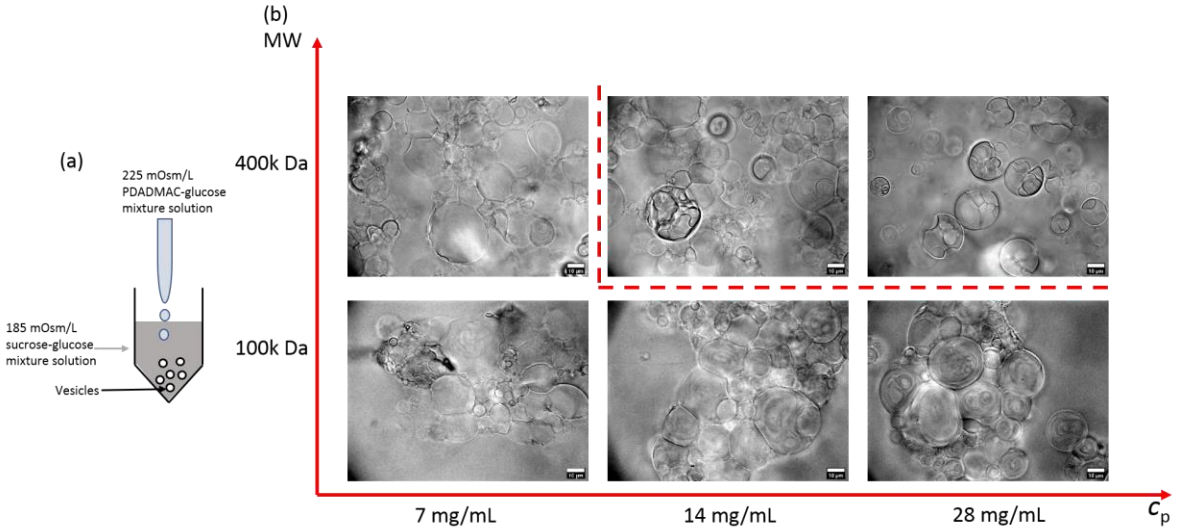

Figure 4.8: (a) Schematic plot of mixing SLPC vesicle suspension with 225 mOsm/L type 1 and type 2 PDADMAC solutions. (b) PDADMAC MW dependence on superparticle formation in the presence of 40 mOsm/L osmotic shock.

4.2.7 Electrostatic screening effect on superparticle formation

Given the high charge density on PDADMAC, we infer the electrostatic interaction is the main reason for the superparticle formation. To test this inference, we mixed vesicle suspension (180 mOsm/L) with NaCl solution (90 mM, 186 mOsm/L) in different volume ratios to achieve 0, 20, 40, 80 mM NaCl concentration. Afterwards, we uniformly mixed 50 μL vesicle-salt mixture solution with 10 μL type 0 PDADMAC stock solution (MW between 100k – 200 kDa, 35 mg/mL, 180 mOsm/L).

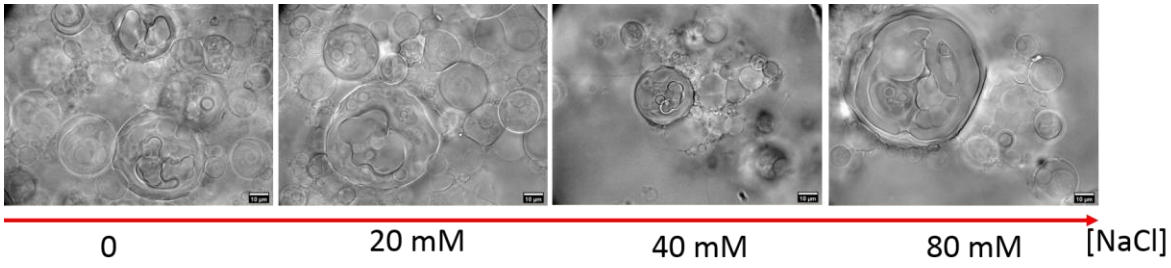

Figure 4.9: NaCl concentration dependence on superparticle (5.8 mg/mL) formation

After 48 h, we found superparticles at each NaCl concentration as shown in Figure 4.9, in which we can see superparticles formed at each NaCl concentration. Although we expected to see a weakening of the electrostatic double-layer interaction with added salt, it might be that this system was too far from the threshold cP value for the added salt to push the system across the threshold.

4.3 Discussion

4.3.1 Superparticle formation and release mechanism

Superparticle formation process illustrated in Figure 4.10(a) shows our hypothesis that the inner compartments originate from multilamellar vesicles. The inner compartments release process illustrated in Figure 4.10(c) makes this is a novel way to drive vesicles to release the excess membrane.

Assuming that the total area of membrane is conserved, and that all of the outer lamellae (except one) are delaminated and turned into the boundaries of interior compartments, we can estimate the typical width of these compartments compared to the initial outer vesicle size. If the total number of delaminated lamellae in the outer membrane is *N*, then the internal size should be proportional to the total radius divided by *N*. The steady-state structure might be limited by *N*. On the other hand, the fluorescence images of Figure 4.1(d,e,f) show that the outer membrane remains multilamellar, and it may therefore be that the steady state is set by a typical size of the internal compartments.

In this section, we propose an explanation to describe the dynamics during superparticle formation and release. In the formation process, we believe PDADMAC molecules penetrate through

outside membrane and bind to inner membranes. There are two possibly reasons for the penetration: one is that PDADMAC binding may increase membrane lateral tension and enlarge the gaps between lipid molecules to let PDADMAC molecule go through; the other one is the entropy driven process: when PDADMAC concentration outside is fairly high, the total entropy is unfavorable for excessive PDADMAC molecules to stay in limited space. (We note, though, that the total osmolarity is kept the same on the inside and outside, by addition of glucose.) As indirect evidence that PDADMAC might permeate the membranes, we point out the finding of chapter 3 that the presence of PDADMAC enabled anionic fluorescein dye to permeate across the membranes when $c_P \geq 0.0069$ mg/mL. This permeation could indicate that complexes of PDADMAC and fluorescein move together, and that PDADMAC might do this even by itself in the absence of fluorescein.

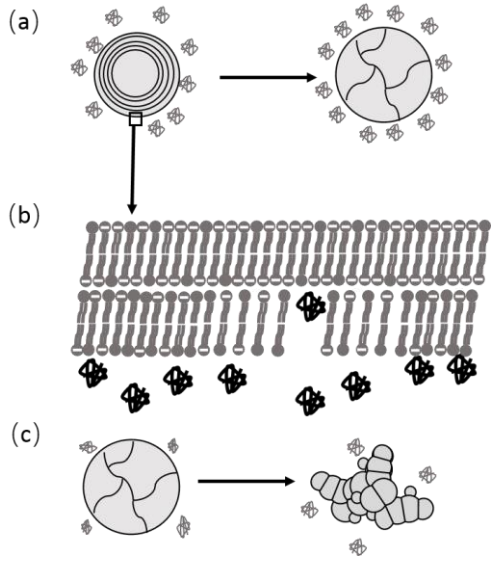

Figure 4.10: (a) Schematic plot of superparticle formation. (b) Schematic plot of PDADMAC penetrating lipid membrane. (c) Schematic plot of superparticle releasing inner compartments.

At low PDADMAC concentration (*e.g* type 0 PDADMAC, MW between 100k – 200k Da, $c_p \leq 0.069$ mg/mL), the membrane tension might not be strong enough to let PDADMAC penetrate, or c_p is too low to create a sufficient entropic drive to push the polymer across the membrane. But at high PDADMAC concentration (*e.g* type 0 PDADMAC, MW between 100k – 200k Da, $c_p \geq 0.69$ mg/mL), the PDADMAC molecules is excessive, some outside molecules are forced to penetrate through membrane and and then bind to the inner membranes as shown in Figure 4.10(b). The inner membranes would then become fully coated by PDADMAC and reverse their charge, which would induce electrostatic repulsion between each layer. The internal structure is forced to reorganize (delaminate) to lower the free energy. As for the morphology after reorganization, it is still under exploration.

4.3.2 Molecular weight dependence mechanism

From the comparison between type 1 (MW<100k Da) and type 2 PDADMAC (MW between 400k – 500k Da) in chapter 4.2.4, we can see under same polymer concentration, type 2 PDADMAC can induce superparticles but type 1 cannot. We attribute the higher total charge on each individual PDADMAC molecule, which means that the bulk concentation that leads to overcharging of the membrane (making it positive and self-repulsive) would be lower.

4.4 Conclusion

In summary, we reported a novel membrane morphology – superparticles, which are nearly spherical but have closed inner membrane compartments (verified by confocal microscopy). We found superparticles only formed when multilamellar vesicles were exposed to high PDADMAC concentration environment with PDADMAC molecular weight larger than 100k Da. With a molecular weight of 400 kDa, we found a threshold concentration of 14 mg/mL. We verified superparticle inner compartments formed from the reorganization of multilamellar vesicle internal membranes. After PDADMAC concentration outside was lowered, the internal compartments would pop out and adhered with each other to form vesicle gel. We also demonstrated that salt cannot prevent the superparticle formation. We propose PDADMAC can permeate through lipid membranes and bind to internal membranes, resulting in electrostatic repulsion.

Superparticles might find application as a method to convert multilamellar vesilces to unilamellar vesicles by exposure to high poylcaton concentration followed by strong dilution. In addition, the ability to make individual vesicles with separately defined interior compartments might lead to a route to vesicles with functionally distinct, membrane-defined compartments.

Chapter 5

LIGHT TRIGGERABLE PARTICEL-MEMBRANE INTERACTION

5.1 Introduction

Vesicles are highly promising structure of controlled encapsulation and release because the membranes can serve as boundary to separate inside and outside aqueous environments. Vesicles can encapsulate cargos, such as drug, dye and nutrition, and release them when certain stimuli like temperature, pH, binding particles, or light are provided. These examples are inspired by the ability of live cells to control traffic across their membranes. In the context of artificial materials, however, light-sensitive membranes are an interesting topic since light stimuli can be turned on and off rapidly without flow-induced external disturbance. It is a meaningful work to design a light-triggerable vesicle responsive system to fulfill trigger-release process.

Previous studies have shown that lipid membrane can respond to particles due to electrostatic interaction. Simulation works indicate that charged particles can bind to membranes when adhesion energy is strong enough [18]. Experiments have demonstrated that particle-membrane interaction can lead to both vesicle-vesicle adhesion and vesicle rupture [24]. There is a transition from adhesion to rupture based on the adhesion and bending energy competition. In these cases, however, the binding interaction was present as the particles were added, so that the reaction occurred at a diffusion-limited rate. Ideally, we could design a system in which particles and membranes will coexist with no change until the stimulus is received. In addition to its direct applications, such a system also creates the potential to encapsulate many different kinds of triggerable particles (responding to different triggers) inside different vesicles that contain different cargo. These vesicles could be formed into a vesicle gel as in chapter 3 or could be a suspension. The system would remain intact until the appropriate stimulus is received, which could then trigger adhesion or disruption.

Light as trigger to induce particle response system has been widely studied for various applications such as drug delivery, signal amplification etc [39]. By introducing g light sensitive groups on nanoparticles, it is possible to change the particle charge, and therefore adhesion strength and structure of the membrane-particle system. l

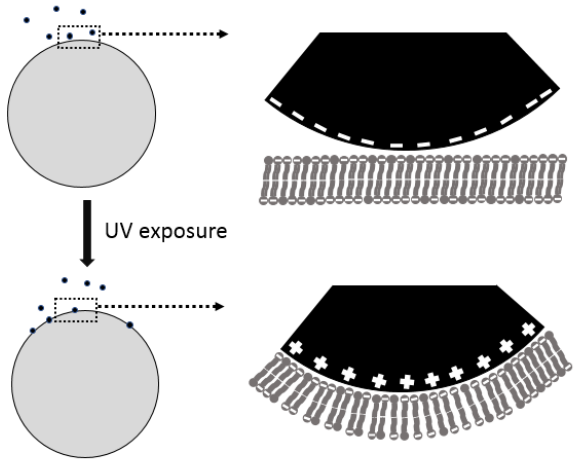

Figure 5.1: Schematic plot of light sensitive vesicle response system.

In this chapter we report an amphiphile-based system that triggers vesicle-vesicle adhesion or vesicle destruction, on demand, by means of a UV stimulus. This projects was done in collaboration with Jingjing Gao and Professor S. Thayumanavan of the Chemistry Department at the University of Massachusetts Amherst. Our collaborators designed and synthesized polymers that self-assemble into nanoparticles with a surface charge density that can be tuned stoichiometrically or by exposure to UV. The mechanism of response involves tuning the electrostatic interaction between lipid membranes and the self-assembled nanoparticles. (See Figure 5.1) We used phospholipid membranes consisting of mixtures of nearly neutral and anionic lipids so that we could tune the membrane charge density. We also tuned the charge density of the nanoparticles to map the final state as a function of these two charge densities. Finally, we chose two examples of membrane and charge density and showed how the system could be switched from fluid to gel or destroyed vesicles within 20 min of exposure to ultraviolet light.

Amphiphilic diblock copolymers were designed to self-assemble into micellar nanoparticles with variable surface charge density. We used three different polymers, each consisting of a hydrophobic block with a hexanyl coumarinyl methacrylate monomer and a hydrophilic block containing PEG_{112} and an end group which we changed from neutral (in **P0**) to a cationic primary amine (**P1**). We also synthesized a UV-

sensitive polymer (**P2**) with a nitrobenzyl-based end group that switches the charge from neutral to positive on exposure to UV [39]. All of these polymers assemble as micellar nanoparticles with a surface charge that is either neutral (for **P0**) or positive (**P1**), or switchable (**P2**) in an aqueous environment. To map the response of the system, we varied the charge density of both the nanoparticles (by means of the fraction of **P1**) and of the membranes (by mixing zwitterionic and anionic lipids). We found four distinct modes of response, ranging from vesicle-vesicle adhesion at relatively low charge densities to rapid vesicle rupture at high charge densities. Turning to the triggered systems, we found that self-assembled nanoparticles composed of **P2** switched the sign of their charge from neutral to cationic. We demonstrated that suspensions of anionic vesicles and these nanoparticles were stable upon mixing. Upon UV exposure, the vesicles either rapidly aggregated into a vesicle-gel structure or rapidly self-destructed. The mode of response depended in a tunable manner on the charge density of the membranes. We quantitatively explain our results by comparing the electrostatic double-layer interaction to the energy cost of deforming the membrane, and show how the results come from a spontaneous wrapping of the nanoparticles by the membrane when the interaction was strongly attractive. These results show that a solid material can be formed from liquid state with UV since vesicle-based gel is a solid as previous studies have shown. We confirm that a delivery system can be made by combining vesicles and triggerable nanoparticles.

5.2 Experiments and results

5.2.1 Materials and methods

Materials: All reagents were purchased from Sigma Aldrich and used without further purification unless specified otherwise. Azobisisobutyronitrile (AIBN) was recrystallized in ethanol prior to use. 1, 2-dioleoyl-sn-glycero-3-phosphocholine (DOPC), 1,2-dioleoyl-sn-glycero-3-phospho-(1'-rac-glycerol) (DOPG) were purchased from Avanti Polar Lipid (Alabaster, Alabama, USA).

Methods: ^{1}H NMR and ^{13}C NMR spectra were recorded on a Bruker DPX-400 MHz NMR spectrometer using the residual proton resonance of the solvent as the internal standard. Molecular weight of the polymers was measured by gel permeation chromatography (GPC, Agilent) using a PMMA standard with a refractive index detector. THF was used as eluent with a flow rate of 1mL/min.

P0, P1, P2 nanoparticles preparation: The polymers **P0**, **P1**, and **P2** (molecular structure shown in Figure 5.2(a))were synthesized as described in the Appendices B. Self-assembled nanoparticles were made with the following procedure: 1 mL 180 mOsm/L glucose aqueous solution was added dropwise to a 100 μL solution of polymer (**P0**, **P1** or **P2**) in acetone (5 mg/mL) and stirred overnight to allow acetone to evaporate. The size and zeta potential of the resulting self-assembled particles were recorded by a Malvern Nanozetasizer ZS90 with a 637-nm laser source with non-invasive backscattering technology detected at 173^{o} using disposable sizing cuvette. Sample was measured at a concentration of 0.2 mg/mL. We refer **P0**, **P1** and **P2** nanoparticles as **NP0**, **NP1** and **NP2** respectively.

Transmission Electron Microscopy (TEM): The **NP0**, **P1** and **NP2** samples were dropped onto carbon-coated copper grid. The grid was dried by slow evaporation in air, and then dry separately in a vacuum overnight. Images were recorded on a JEOL-2000FX electron microscopy operated at 200 kV and at a nominal magnification of 5000X.

Vesicle preparation: We used mixtures of zwitterionic 1, 2-dioleoyl-sn-glycero-3-phosphocholine (DOPC), anionic 1,2-dioleoyl-sn-glycero-3-phospho-(1'-rac-glycerol) (DOPG), and anionic 1, 2- dioleoyl-sn-glycero-3-phospho-L-serine (DOPS). As described earlier, former research indicated that DOPC carries slightly negative charge in aqueous solution while DOPG and DOPS are negatively charged [6]. By varying the ratio of DOPG and DOPC, membrane charge density can be controlled [6]. Vesicles were made with sucrose inside and a glucose-sucrose mixture outside. In all cases, the osmolarities of the interior and exterior were measured (Vapro model 5600 osmometer) and kept at 180 mOsm/L to avoid osmotic stress. Osmolarity measurements were repeated 3 times and the standard deviation was usually 3-4 mOsm/L.

Vesicles were prepared by electroformation mentioned in chapter 2.2.1 : 10mg/mL DOPG and DOPC lipid stock solutions in chloroform were prepared, and the two stock solutions were mixed to achieve a DOPG molar percentage ranging from 0 to 100%. Two clean ITO-coated glass slides were coated, each with 50 µL of the mixed lipid solution and dried under vacuum for 2 h. The ITO slides were held by Teflon spaces with their ITO-coated surfaces facing one another. The gap between them was filled with 3mL of 180 mOsm/L sucrose solution. Electroformation was carried out at 40 °C with a sinusoidal applied voltage at 10 Hz and peak-to-peak voltage 2.4 V for 105 min. After transferring the vesicle suspension to a vial, we added 2.5 mL of glucose solution of the same osmolarity and collected 50 µL of concentrated vesicle suspension at the bottom after sedimentation for 24 h.

Microscopy: The dynamics and steady-state response of mixtures of self-assembled particles and vesicles were imaged using optical microscopy. Bright-field images were acquired through two combinations: one is using a Flir blackfly S CMOS camera and a Zeiss 20× Plan Neofluar objective with 0.4 NA, the other one is CoolSnap HQ2 camera (Roper Scientific) and a Zeiss 63× Plan Neofluar objective with 1.4 NA. Dark-field images were acquired using the CoolSnap HQ2 camera and a Zeiss 100× Plan Neofluar objective with 1.3 NA. The CoolSnap camera measures pixel values that are proportional to the light intensity.

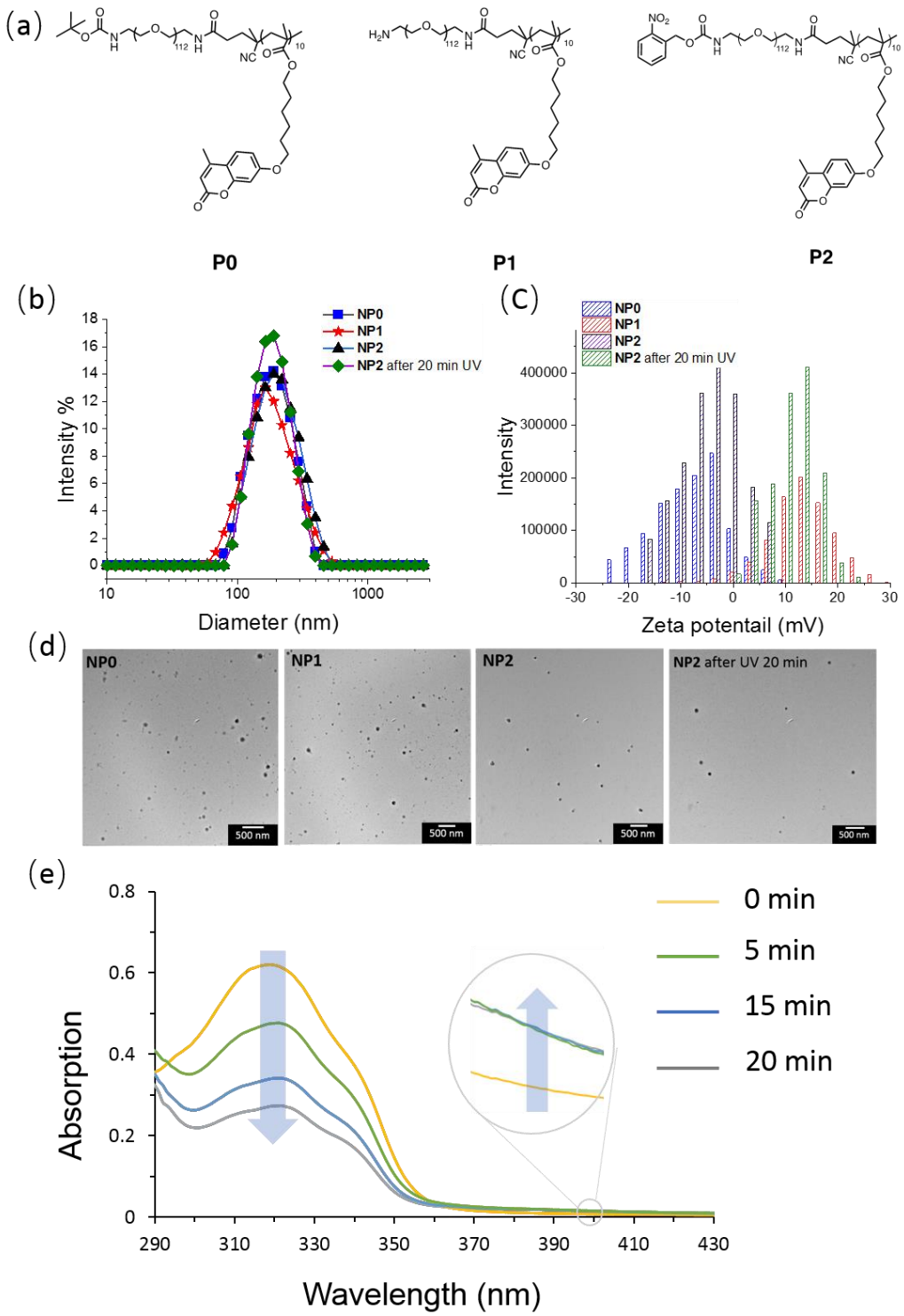

Figure 5.2**:** (a) Molecular structure of **P0**, **P1** and **P2**. (b) DLS spectrum of **NP0**, **NP1**, **NP2** and **NP2** after 20 min UV exposure. (c) Zeta potential spectrum of **NP0**, **NP1**, **NP2** and **NP2** after 20 min UV exposure. (d) TEM images of **NP0**, **NP1**, **NP2** and **NP2** after 20 min UV exposure. (e) Absorption spectrum of **NP2**.

5.2.2 Particle properties

The amphiphilic polymers were designed, synthesized and characterized by our collaborators, Jingjing Gao and Professor S. Thayumanavan. All three amphiphilic polymers, **P0**, **P1** and **P2** with molecular structure shown in Figure 5.2(a), form micellar nanoparticles in aqueous suspension. The average diameter of micellar particles was 125 nm, measured by dynamic light scattering (DLS, Figure 5.2(b)). TEM images in Figure 5.2(d) of dropped cast suspensions of **NP0, NP1** and **NP2** showed discrete particles with a size consistent with DLS (Figure 5.2(b)) The surface (zeta) potentials, inferred from electrophoretic mobility measurements, were -7.9 ± 6.9 mV for **NP0**, 13.0 ± 6.1 mV for **NP1** and -4.1 ± 5.8 mV for **NP2**. The zeta potential mean was estimated using the weighted mean of the probability distribution of surface potentials detected, rather than the peak potential. The uncertainty is the root-mean square deviation from the mean, weighted by the measured probability distribution of the zeta potential. The zeta potential probability distributions of **NP0**, **NP1**, **NP2** are shown in Figure 5.2(c).

Due to the existence of the nitrobenzyl group in **P2**, **NP2** is charge-convertible. An aqueous suspension of **NP2** was exposed to UV (lamp with peak wavelength 365 nm) and its absorbance was monitored by UV-vis. As shown in Figure 5.2(e), a decrease in absorption at 325 nm indicated the coumarin dimerization, and absorbance at 400 nm indicated the cleavage of the nitrobenzyl group, resulting in ionization of the amine group. The zeta potential converted from negative to positive after 10 minutes UV (365 nm, 15W) exposure (Figure 5.2(c)). The DLS spectrum and TEM images show that the morphology of **NP2** did not change in a detectable way after UV exposure (Figure 5.2(d)).

5.2.3 Particle membrane interaction state diagram

To probe the interaction between membranes and nanoparticles, we began by exploring the parameter space using self-assembled nanoparticles of fixed charge, in the absence of a UV stimulus. We made positive charged nanoparticles consisting of mixtures of **P0** and **P1** molecules. We refer to the mole fraction of **P1** as the fraction of amine (relative to neutral PEG), p_{amine}. Giant unilamellar vesicles were

composed of zwitterionic DOPC and anionic DOPG in different molar ratios, and we refer to the molar fraction of DOPG as p_{DOPG}. Both p_{Amine} and p_{DOPG} were set to 0, 25%, 50%, 75% and 100%. We exposed 20 μL of vesicle suspension to 5 μL of micellar nanoparticle suspension in a perfusion chamber, and recorded the interaction under bright field microscopy for at least 1 hour. We explored 25 different combinations of p_{DOPG} and p_{Amine}, with each combination repeated 2-3 times. The typical vesicle response is shown in Figure 5.3.

When p_{Amine} = 0, nanoparticles are near neutral or slightly negatively charged and vesicles have negative charge and charge density is determined by p_{DOPG}. There was no observed interaction between nanoparticles and vesicles, as expected due to the electrostatic repulsion. We observed that the vesicles were still acting as free vesicles, no obvious vesicle deformation happens. This result is same in samples with p_{DOPG} = 0%, 25%, 50%, 75% and 100%. Therefore, free-vesicle state was observed under p_{Amine} = 0 no matter what p_{DOPG} is.

When p_{Amine} = 25%, we observed vesicle-vesicle adhesion and vesicle destruction. When $0 \leq p_{DOPG} \leq 50\%$, vesicle-vesicle adhesion was observed, and no vesicle destruction was detected. When 75%<=p_{DOPG}<=100%, adhesion was still observed but vesicle destruction was also captured. We saw multiple single vesicles got ruptured. And after single vesicle ruptured, the lipid residue was a floating object with high degree of freedom as shown in Figure 5.4(c). We attribute it to the adhesion energy strength. When $0 \leq p_{DOPG} \leq 50\%$, the adhesion energy between nanoparticles are strong enough to overcome thermal fluctuation and nanoparticles can be partially wrapped by membranes, the unwrapped part is still left which could interact with another vesicles. There is a double-layer interaction between nanoparticles and membranes as described in chapter 1.3.1, which further leads to vesicle-vesicle adhesion. When 75%<=p_{DOPG}<=100%, the adhesion energy is so strong that nanoparticles could be fully wrapped. Due to membrane area is consumed by multiple nanoparticles and vesicle area still needs fixing,

the membrane tension goes up and results in vesicle rupture. It is worth noting that after single vesicle rupture, the lipid residue is a floating object with high degree of freedom as shown in Figure 5.4(c).

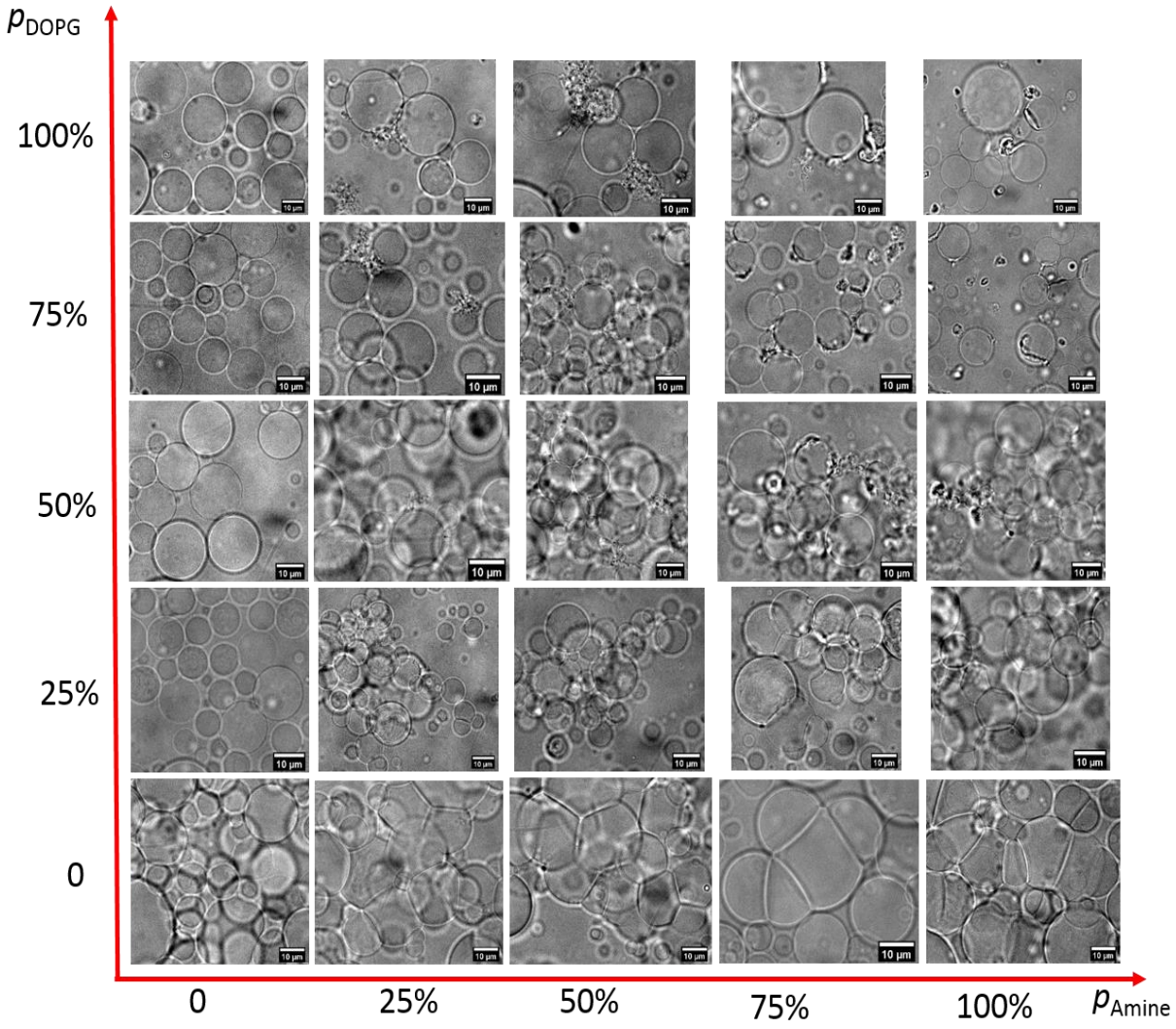

Figure 5.3 : Typical vesicle response states in different combinations of p_{Amine} and p_{DOPG}.

When p_{Amine} = 50%, both vesicle-vesicle adhesion and vesicle destruction were observed. When 0<=p_{DOPG}<=25%, only vesicle-vesicle adhesion happened. When 50%<=p_{DOPG}<=100%, vesicle-vesicle adhesion still globally existed. But for some vesicles, vesicles were destroyed. Just like p_{Amine} = 25%, the lipid residue is still the floating object with high degree of freedom.

When p_{Amine} reached 75%, vesicle-vesicle adhesion happened when 0<=p_{DOPG}<=25%. When 50%<=p_{DOPG}<=100%, vesicle-vesicle adhesion was global, and some vesicles got destroyed but the lipid residue was no longer with high degree of freedom but concrete aggregate which shows no transparency as shown in Figure 5.4(d).

When p_{Amine} = 100%, vesicle-vesicle adhesion was still in dominance when 0<=p_{DOPG}<=25%. When 50%<=p_{DOPG}<=100%, the state was indistinguishable with that of p_{Amine} = 75% -- vesicle-vesicle adhesion and vesicle rupture happen. The lipid residue was still concrete aggregate. But some spherical caps were observed. These caps were formed from two adhered vesicles with one bursting and leaving the residue on the membranes of the other one. we infer the concrete residue has high stiffness since it can hold the tension on membrane as shown Figure 5.4(e).

In summary, we found four distinct particle-membrane interaction states as shown in Figure 5.4 (a-e). With p_{amine} = 0 (particles of **P0** only), we could discern no particle-membrane interactions; the vesicles behaved as free suspended vesicles (Figure 5.4 (a)). With increasing p_{amine}, and modest p_{DOPG}, we found adhesion of vesicles to one another (Figure 5.4 (b)), leading to a macroscopic gel phase. The gel phase was stable over time, with no discernible rupture of the vesicles over a period of 1 h. With higher charge densities, (Figure 5.4 (c)), we observed at least some of the vesicles burst into a compact flexible residue which had high degree of freedom of movement. At the highest charge densities, (Figure 5.4 (d)) we found that vesicles burst and then formed a compact residue with little discernible movement or flexibility. Figure 5.4 (e) shows a common case that coexisted with that of Figure 5.4 (d): given two adhered

vesicles, one of them could burst and leave a ring of residue on the other vesicle, in the form of a spherical cap. The presence of absence of these behaviors was repeatable in samples with the same composition. We emphasize that the boundary between these responses was sharp and well defined. The transition from adhesion-only to destruction was defined as the *onset* of destruction, but in this region not all vesicles were destroyed. We observed vesicle-vesicle adhesion in the destruction region as well.

These behaviors are summarized in a state diagram, shown in Figure 5.4(f). The states that are defined as rupture (corresponding to Figure 5.4(c,d,e)) were defined as those in which vesicles were seen to undergo rupture. In these cases, some vesicles remained intact as will be described below. The states vary systematically with the values of p_{DOPG} and p_{amine}. For example, with p_{amine} fixed at 50% and varying p_{DOPG}, we find a trend from vesicle-vesicle adhesion to vesicle rupture as a flexible residue when p_{DOPG} reaches 50%. On the other hand, when we kept p_{DOPG} at 50%, we observed no interaction at $p_{Amine} = 0$, vesicle-vesicle adhesion at $p_{\mathrm{amine}} = 25\%$, vesicle rupture and flexible residue at $p_{\mathrm{amine}} = 50\%$, and vesicle rupture with compact residue at $p_{\mathrm{amine}} = 75\%$ and 100%. We also observed that roughly 1 out of 20 surviving vesicles showed the spherical cap (as in Figure 5.4(e)) at $p_{\mathrm{amine}} = 100\%$. The rupture was fast, happening within 1 s.

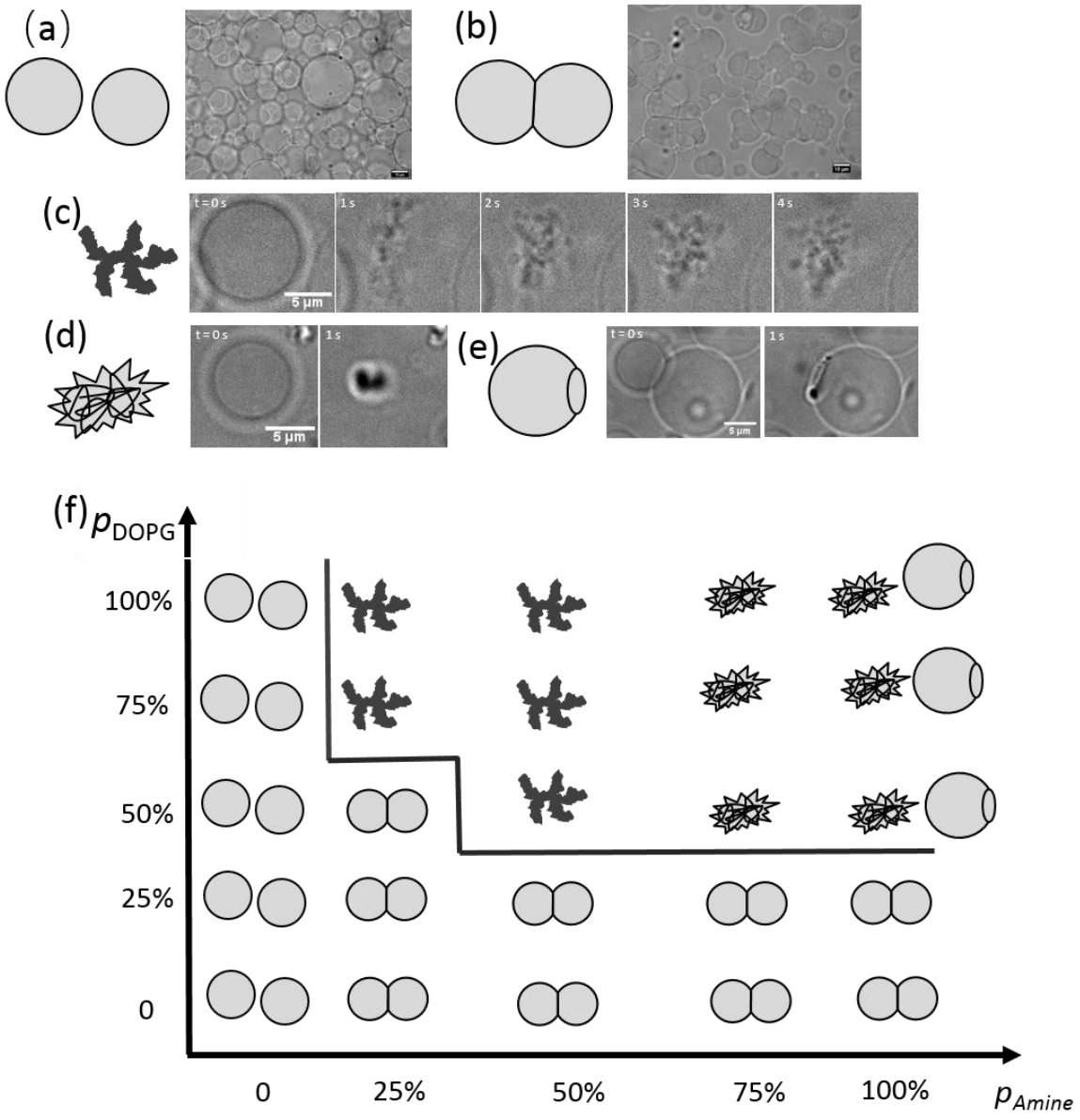

Figure 5.4: Four distinct states of particle-membrane interaction. (a) Free vesicle state. (b) Vesicle-vesicle adhesion. (c) Vesicles burst into flexible residue. (d) Vesicles burst into compact aggregates. (e) One vesicle burst and leaves a spherical cap on a neighboring vesicle. (f) State diagram shows the results one hour after mixing, with different combinations of p_{DOPG} and p_{amine}.

5.2.4 Dark field microscopy analysis

We used dark field microscopy to monitor the intensity of scattered light in the vicinity of the membrane. We began with DOPC vesicles (p_{DOPG}=0). Figure 5.5(a) is a dark-field image of a typical vesicle, showing weak contrast between membrane and background. We then exposed the vesicles to **NP1** particles (p_{amine}=100%), with 20 μL of vesicle suspension combined with 5 μL of **NP1**. After 30 min, the intensity near the membrane was significantly higher, and was higher still in regions where two vesicles adhered to one another (Figure 5.5(b)).

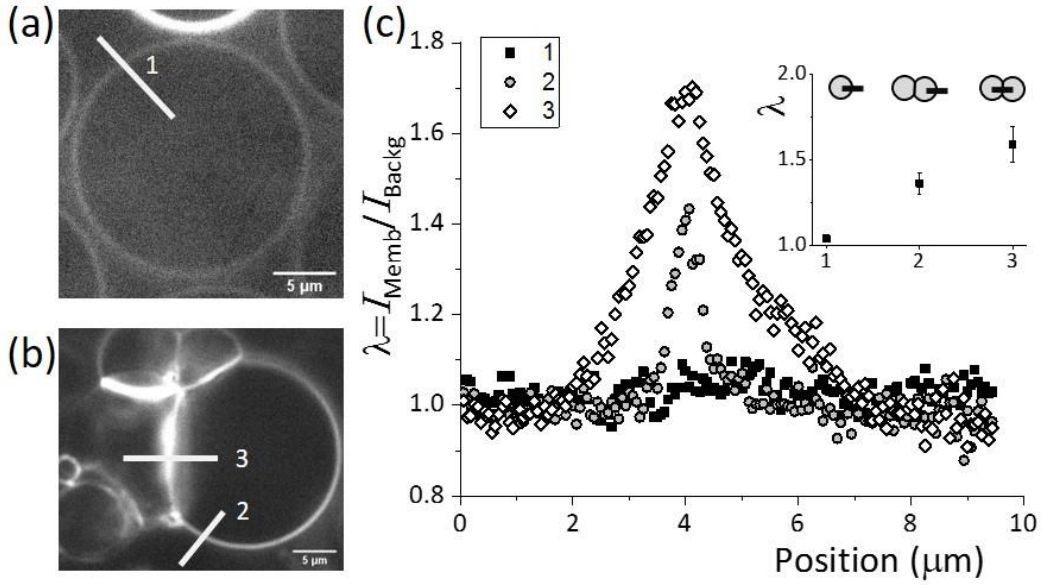

Figure 5.5: Dark-field images of vesicles and nanoparticles. (a) DOPC vesicles (p_{DOPG} = 0) without particles. (b) In the presence of **NP1** particles (p_{amine} = 100%), dark-field images show higher contrast near the membrane. 1st is free lipid membrane, 2nd is single layer and 3rd is double layers exposed to PCN (p_{Amine}=100%) under dark field. (c) Plot of relative camera intensity along the three line segments shown in white in (a,b). Inset: the mean and standard error of λ for a population of vesicles in the 3 cases of just vesicles (#1); particles and vesicles (#2), and particles and vesicles in regions of vesicle-vesicle adhesion (#3).

To quantify the response, we measured the ratio of image intensity across a line, divided by the average background intensity. Figure 5.5(c) shows λ for the images, measured along the white lines labeled 1, 2 and 3. The plot shows a significant peak in λ located at the membrane, indicating binding of particles, The inset shows the peak values at the membrane for a wider set of measurements. Each data point shows the mean and standard error of the mean of 14 or more unilamellar vesicles with focus at the equator under dark field. The 3 cases are as illustrated in parts (a,b) of the figure. Our results show that nanoparticles accumulate with greater surface coverage in the adhered-membrane region.

In addition, we also did an experiment to record the time dependent λ change. We exposed 20 μL 10% DOPS and 90% DOPC vesicles to 5 μL **NP1** (p_{Amine}=100%) in perfusion chamber and kept recording under dark field (DOPS is negatively charged but charge density is lower than DOPG but higher than DOPC). The time-dependent images are shown in Figure 5.6. We marked a double layer region in red box at t = 0. We observed at t = 0, the adhesion surface is not obvious; at t = 7 min, clear adhesion surface appeared; from t = 8 min to 11 min, the adhesion surface scattering kept getting stronger. The double layer region was brighter than the single layer region. The physical essence is same as that in Figure 5.5, **NP1** is more inclined to accumulate in double layer region than single layer region.

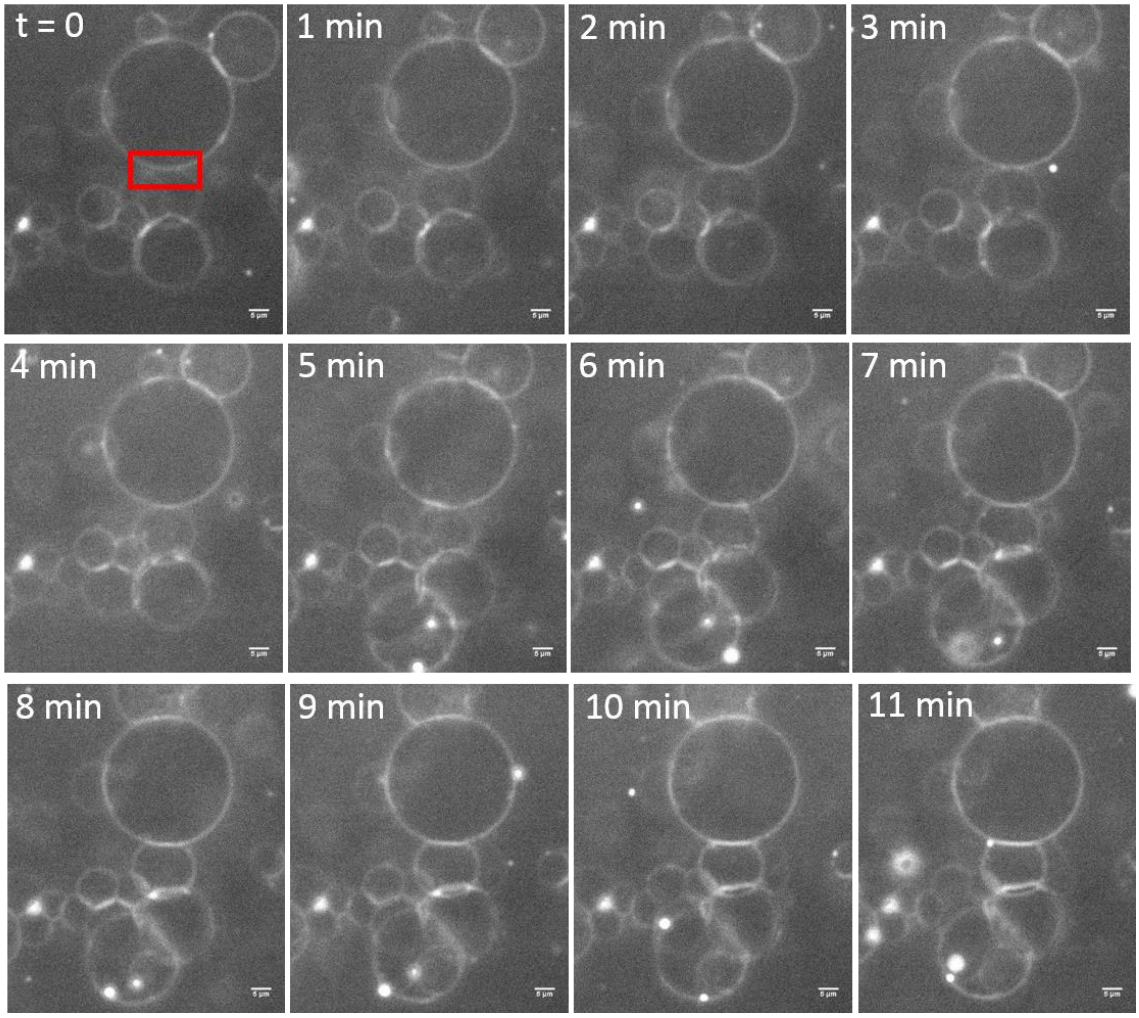

Figure 5.6: 10% DOPS and 90% DOPC vesicles interaction with PCN (p_{Amine}=100%) under dark field microscopy. The red box region at t = 0 is a double layer interaction example, it is getting brighter with time going on.

We selected 4 regions including 3 single layer and 1 double layer region to track λ change through python program presented in chapter 2.7 as shown in Figure 5.7(a). The time dependent λ of these regions are shown in Figure 5.7(b). We can see that λ in the double-layer region increased with time while single layer regions did not have a significant change. Our results show that accumulation of particles in the double-layer region is a gradual process.

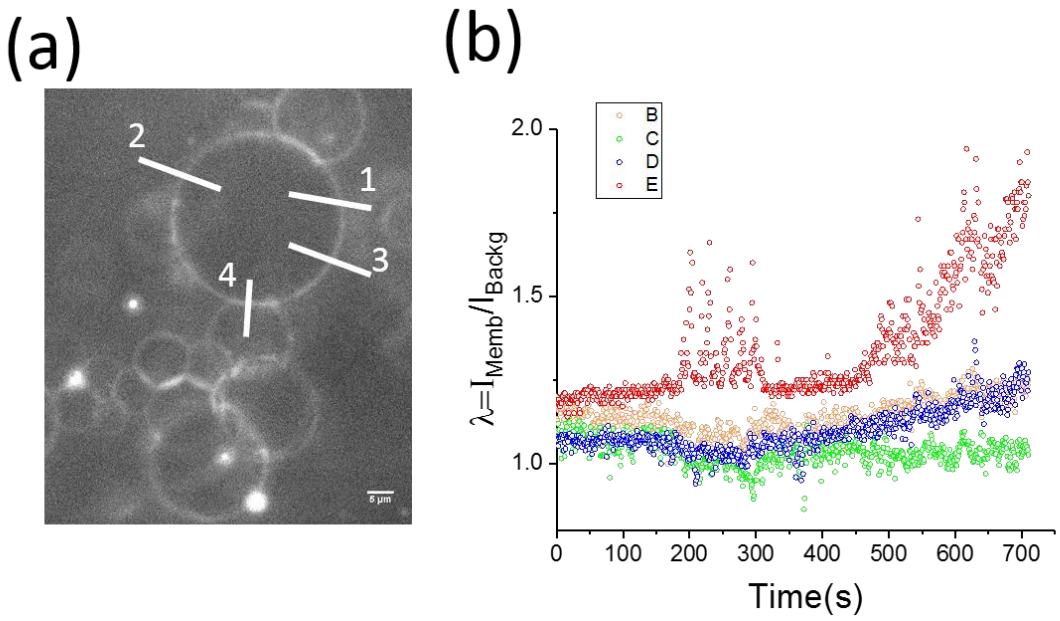

Figure 5.7: (a) Illustration of the 4 selected regions. 1, 2, 3 are single layer regions and 4 is double layer region. (b) Time dependence of light intensity ratio of the 4 selected areas. The fluctuations in the 200-300 s region are from impurity movement.

5.2.5 Light induced vesicle-vesicle adhesion and vesicle rupture

We used the **NP2** nanoparticles to demonstrate triggered vesicle-vesicle adhesion or vesicle rupture response on demand.

To trigger vesicle-vesicle adhesion, we mixed 100 μL vesicle suspension (p_{DOPG} = 0) and 200 μL **NP2** uniformly. Then we split the vesicle-**NP2** mixture suspension into control (150 μL) and experiment (150 μL) groups. We observed that vesicles in the control group were still freely suspended with no adhesion detected 24 hours after mixing. On the contrary, after deposited in a sealed perfusion chamber (light transmissive) to prevent water evaporation, the experiment group was exposed to UV (wavelength 365 nm, power 15W) for 10 min in a UV chamber. We then inspected the sample in a different location and noted typical vesicle-vesicle adhesion as shown in Figure 5.8(a). (Since vesicles in perfusion chamber

almost sank to the bottom and kept static, the vesicles before UV exposure sank to bottom and were well aligned). In terms of Figure 5.4(f), this result corresponds to rapidly shifting from p_{amine}, p_{DOPG} = (0,0) to (0, 100%). The observed final state is indistinguishable from what we reported in the steady-state experiments above.

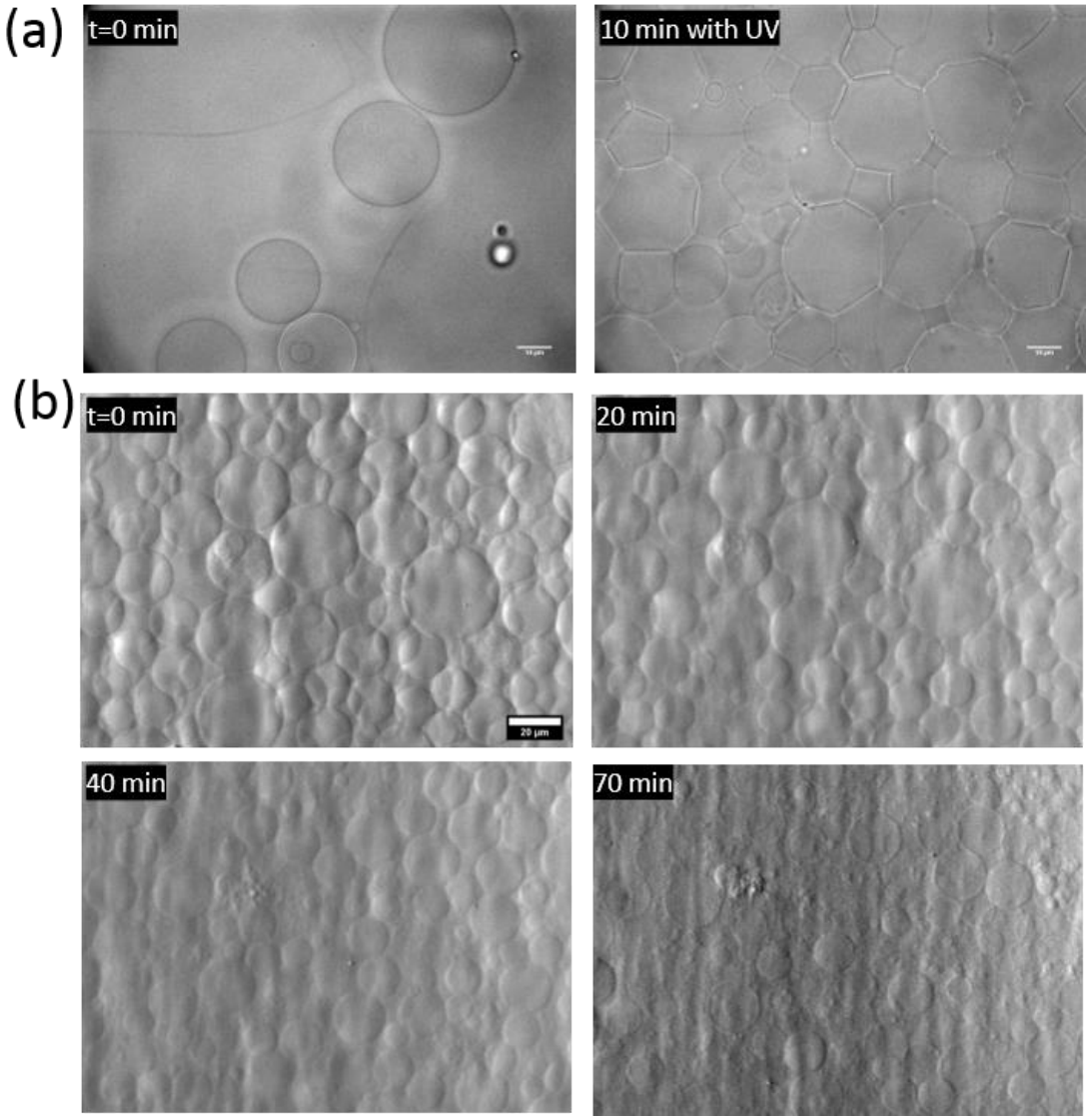

Figure 5.8: (a) Bright-field optical Images of triggered response. (a) UV triggered vesicle-vesicle adhesion of vesicles (p_{DOPG} =0) mixed and **NP2**. UV was turned on at t = 0. (b) Time sequence of UV-triggered vesicle destruction of vesicles with p_{DOPG} =100%, mixed with **NP2**. UV was turned on at t=0.

To trigger vesicle rupture, we set p_{DOPG} = 100%. After depositing 1 μL vesicle suspension with 300 μL **NP2** suspension without mixing in a glass chamber, we exposed UV (wavelength 365 nm, power density 8 mW/cm^2) to our sample continuously and continually acquired bright-field images during the UV illumination as shown in Figure 5.8(b). We observed clear vesicle rupture and a dramatic decrease in the number of intact vesicles over time. From image analysis, we found that 83 out of the initial 124 vesicles were ruptured within 70 minutes. During this process, we also noted a reduction of contrast between the inside and outside of the vesicles. We attribute this to the rupture releasing the glucose from inside the vesicles; we will return to this point in next section.

5.3 Discussion

We attribute the membrane response to electrostatic attraction between the membrane and the nanoparticles, leading to binding. Previous work has shown that the zeta potential of 100% DOPC, 20% DOPG and 80% DOPC, 100% DOPG membrane are near -8, -70 and -80 mV respectively at low NaCl concentration (~10 mM) [6]. When the nanoparticles have only **P0** (p_{Amine} = 0), their charge is near zero and the interaction between lipid membranes and nanoparticles is weak. For any value of p_{DOPG}, vesicles moved freely as illustrated in Figure 5.9(a). After increasing p_{Amine} to ≥ 25%, the nanoparticles are positively charged, leading to a double-layer interaction with the negatively charged membrane. When the attractive interaction strength was moderate (eg. p_{amine} = 100% and p_{DOPG} = 25%), nanoparticles bound to the membrane. They also caused adhesion between two membranes as illustrated in Figure 5.9(b), forming vesicle gel like the ones discussed in chapter 3, where shear rheology studies indicated that the vesicle gel is a solid with non-zero storage modulus(~1 Pa) at low frequency (~0.1 rad/s).

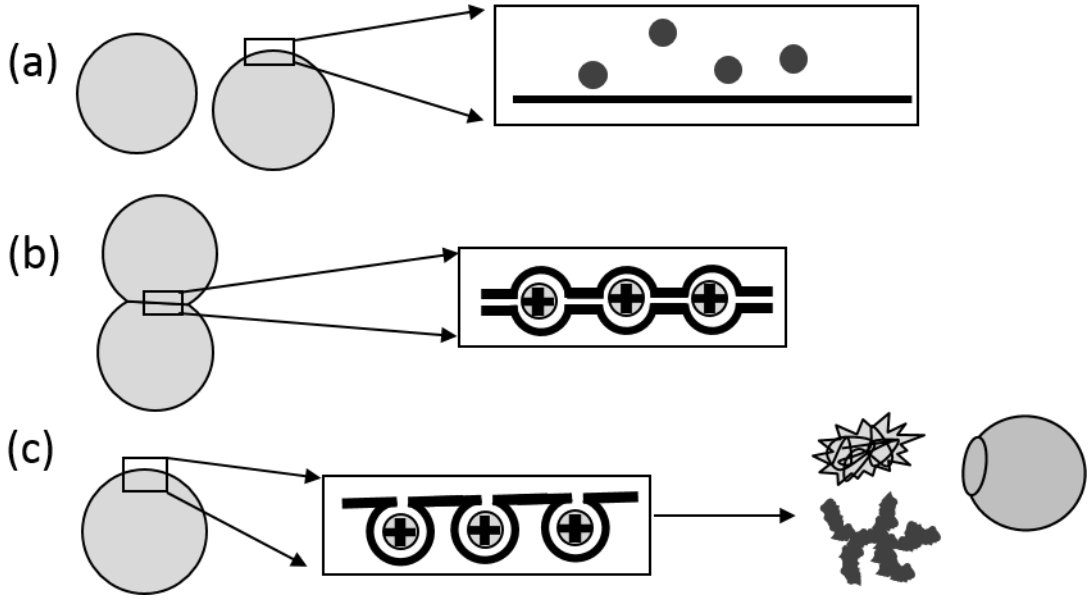

Figure 5.9: Illustration of particle membrane interaction transition. (a) No binding. (b) Membranes partially wrap nanoparticles. (c) Membrane fully wraps nanoparticles.

When the attractive interaction is strong (*e.g.*, p_{amine} = 25% and p_{DOPG} = 100%), nanoparticles induce a rupture of the vesicles. We attribute this response a transition from weak binding and weak deformation of the membrane, to strong binding and compete wrapping of the particle by the membrane. Earlier work has shown there is an energy competition between adhesion and bending. Particle adhesion energy is represented as wa^2 where w is the adhesion energy per area and a is the radius of the particle. Bending energy is characterize by bending modulus κ. When $wa^2/\kappa > ½$ [24], adhesion energy dominates, the membrane maximizes its binding area with the particles, which leads to fully wrapping as shown in Figure 5.9(c). Given the membrane tension consumed by particles, membrane tension increases dramatically and vesicle ruptures. On the contrary, when wa^2 / κ is below threshold, bending energy is dominant, only partial wrapping occurs so that the particle remains partly exposed, then vesicle-vesicle adhesion is achieved owing to the particles binding to two membranes.

We propose a straightforward continuum-level model to predict the conditions leading to the triggered rupture. We used the Debye-Hückel model for the electrostatic double-layer interaction to estimate the binding energy per area *w*. When the distance between the particle surface and the membrane (h) is much smaller than the Debye screening length l_{D}, it is reasonable to regard both membrane and particle as flat plates with surface potentials ψ_m and ψ_p (Figure 1.6(b)). The adhesion free energy per area, *w*, is estimated as $w = (2\varepsilon\varepsilon_0/l_{\mathrm{D}})\,\psi_p\psi_m \exp(-h/l_{\mathrm{D}})$. We assumed that both ψ_p and ψ_m increased linearly with p_{amine} and p_{DOPG} and used our electrophoretic mobility measurements to estimate their values. We then found the set of points in the (p_{amine}, p_{DOPG}) plane where $wa^2/k = 0.5$, the estimated onset of wrapping and destruction with many particles. Owing to the uncertainty in the measured surface potentials, we obtained a range of results corresponding to this predicted transition; details are given in the supplementary section. The calculation and the experimental results are plotted

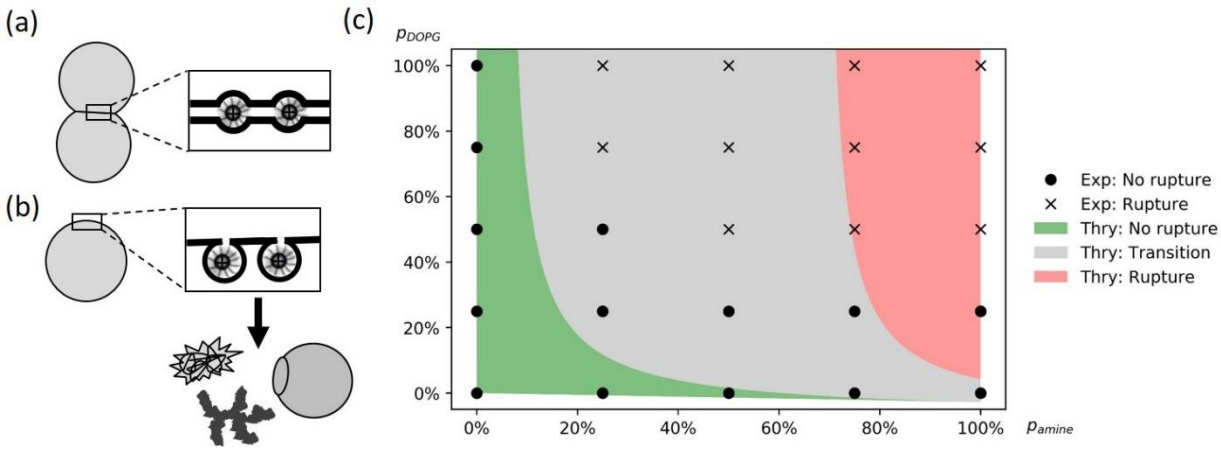

Figure 5.10: The cross-over from weak binding, illustrated in (a), to strong binding where the membrane fully wraps leading to rupture (b). (c) Predicted cross-over from adhesion to wrapping. The cross-over is expected to be sharp and the width of the gray region accounts for uncertainties in the physical parameters. Symbols: ● are measured points of adhesion; × are measured points of wrapping and destruction.

together in Figure 5.10. We found that the model successfully captures the data trend despite the model's simplicity. IN Figure 5.10(c), our model can be classified as 3 different regions: no rupture, transition and rupture region. No rupture region marks the adhesion is below moderate level, no adhesion or partial wrapping is dominating the vesicle-particle interaction, no vesicle deformation or vesicle-vesicle adhesion

is in domination. Transition region is owing to the particle charge density variation shown in Figure 5.2(c), because particle charge density is not homogeneous for each particle, the vesicle response is heterogeneous as mentioned in Figure 5.4(c). In the rupture region, the adhesion energy is so high that particles are fully wrapped by membranes, leading to the vesicle rupture.

In the model, we implicitly assumed that tension was negligible such that $\tau a^2/\kappa \ll 1$. For our system (a = 60 nm, $k \approx 10^{-19}$ J[43]), this condition requires $\tau \ll 30$ mN/m. Tension at that low scale can be realized in vesicles that are slightly deflated by osmotic stress. Such vesicles have clearly visible thermal undulations of their shape, whereas vesicles with τ in the mN/m scale appear spherical in shape (like typical GUVs in our experiments). This leaves open the question of how τ affects binding and wrapping. Here we speculate that when particles bind to a tense membrane, they locally strain it and enhance permeability to water and solute. By this mechanism, τ would decrease over time until the above condition is met and the particles are completely wrapped. This mechanism would explain the approximately 30 s time lag that we observed between particle addition and vesicle destruction.

To check whether the binding energy should be strong enough to induce wrapping, we can use the results of Figure 5.5 to extract a rough estimate of the binding energy for that case. The intensity plots of Figure 5.5(c) show that the concentration of membrane-bound particles is greater between two membranes compared to at one membrane. We do not know how the camera intensity scales with local particle concentration. To get a rough estimate, we note that the particle scatter weakly and assume that the scaling is linear. The inset of Figure 5.5(c) shows a 2-fold enhancement of the local concentration between two membranes (case 3) relative to one membrane (case 2).This enhancement agrees with a previous theory of particle-mediated adhesion of surfaces, which predicted that the concentration of particle in the adhesion spot should be twice that of the free surface [40].

The crossover from flexible residue to rigid residue (Figure 5.4(f)) can be attributed to a greater concentration of bound particles with greater p_{amine}. We speculate that in these conditions, the membrane surface may become jammed by particles and thereby develop a rigid surface.

5.4 Conclusion

In this chapter, we reported a vesicle responsive system designed with light sensitive particles. We observed 4 distinct vesicle response states with different membrane and particle charge density combinations. We showed the interactions among particles and membranes can be rationally tuned using charge density. Based on these results, we made light sensitive particles that were able to convert charge from negative to positive. We accomplished a light sensitive response to achieve a rapid transition from a fluid dispersion to a solid vesicle-based gel, or to achieve rapid and total destruction of the vesicles and release of their interior volume. We attribute the vesicle response to the microscopic membrane wrapping morphology.

Chapter 6

FUTURE WORK

In this chapter, we conclude by first summarizing the key results from chapters 3, 4 and 5. We draw conclusion of the physical essence behind these key results. Finally, we identify some future directions that build on this work.

6.1 Conclusions

In chapter 3, we explained a polyelectrolyte-induced vesicle gel. We varied PDADMAC concentration to tune the gel performance. Rheology results showed that the gel is solid with a shear modulus equal to a few Pascals at low frequency (<10 rad/s) and that it has a linear response with strain amplitude up to 0.7. In addition, vesicle gel is able to support a heavy copper bead against gravity for several hours. Bright field microscopy shows that there is a correlation between vesicle gel stiffness and adhesion strength. To quantify how strong vesicle-vesicle adhesion is, we defined a parameter, effective adhesion strength (λ), to characterize the adhesion strength. We found that λ is not monotonic with PDADMAC concentration but monotonic with gel stiffness. By this way, we succeeded in connecting the microscopic morphology to macroscopic performance. We proposed the shear modulus come from the adhesion energy between vesicle. After comparing gels containing vesicles of different size scales but having similar λ, we conclude that gel modulus does not scale with vesicle size. Finally, we showed that PDADMAC can significantly change the permeability of lipid membrane and gel cannot stop fluorescein and FITC fluorescein penetration. We proposed this is due to the electrostatic association between the dye molecules and the membrane or polymer, and the membrane lateral tension when PDADMAC binds to membranes.

In chapter 4, we reported a novel membrane morphology – superparticles. We found superparticles only appeared when multilamellar vesicles were exposed to high PDADMAC concentration

above a threshold value that increased with PDADMAC molecular weight. We found superparticle formation was the reorganization of multilamellar vesicle internal structure. After decreasing PDADMAC concentration outside, the internal structure would pop out and formed vesicle gel. Confocal images showed superparticles were isotropic and in close-form. We proposed the PDADMAC permeated through lipid membranes and bound to internal membranes, which caused the membrane structure to reform.

In chapter 5, we reported a vesicle responsive system designed with light sensitive particles. We observed 5 distinct vesicle response states with different membrane and particle charge density combinations. We showed vesicle states can be transitioned from free vesicles to vesicle-vesicle adhesion or vesicle rupture under certain conditions that are accurately predicted by Debye-Huckely theory for the electrostatic double-layer interaction combined with the Helfrich model of membrane elasticity. Based on these results, we made light sensitive particles that were able to convert charge from negative to positive. We accomplished the light triggered vesicle-vesicle adhesion by exposing DOPC vesicles and light sensitive particles to UV; we triggered vesicle rupture by shining UV on DOPG vesicles and light sensitive particles. The difference between these responses is owing to the particle-membrane adhesion and bending energy competition, which depends on membrane charge density. We attribute the vesicle-vesicle adhesion to partial wrapping and vesicle rupture to fully wrapping of the particles.

6.2 Future directions

6.2.1 Potential applications of the vesicle gel

The ability to make a solid gel that is 99% water but has a closed-cell morphology leads to many possible applications that would be interesting to study. For example, it should be possible to mix vesicles of different types, containing different cargoes. Or it may be possible to decrease the correlation length by lettering samples age, and thereby increase the modulus. In addition, adhesion induced by a non-electrostatic interaction might prevent selective partitioning of charged solutes into the gel interstices, allowing it to serve as an effective solute barrier.

6.2.2 Particle induced vesicle gel

Rheology measurements in chapter 3 showed that vesicle gels have shear modulus just a few Pascals. It would be interesting to figure out how to increase the stiffness of vesicle gel, which may expand the range of potential applications of this material. A possibility is to form vesicle gel by particles instead of polyelectrolyte. Polymer is able to relax strain since it is long and soft, but particles are rigid, when shear process happens, particles cannot deform to relax stress. In addition computer simulations have shown that membrane-bound particles can form linear structures that may impart elasticity to the membrane, which might also increase the gel modulus [CITE Nanoscale paper, also this one: Saric, A.; Cacciuto, A. "Fluid Membranes Can Drive Linear Aggregation of Adsorbed Spherical Nanoparticles" Phys. Rev. Lett. 2012, 108, 118101. .Vesicle gel induced by particles is potential to have higher stiffness. So far, we have shown that AS-30 particles can induce vesicle-vesicle adhesion. We exposed 20 μL SLPC free vesicles (180 mOsm/L) to 5 μL 0.1 mM silica particles suspension (powder sucrose added to reach 180 mM) in perfusion chamber, the result is shown in Figure 6.1. Clear vesicle-vesicle adhesion was observed. Therefore, particle induced vesicle gel is possible.

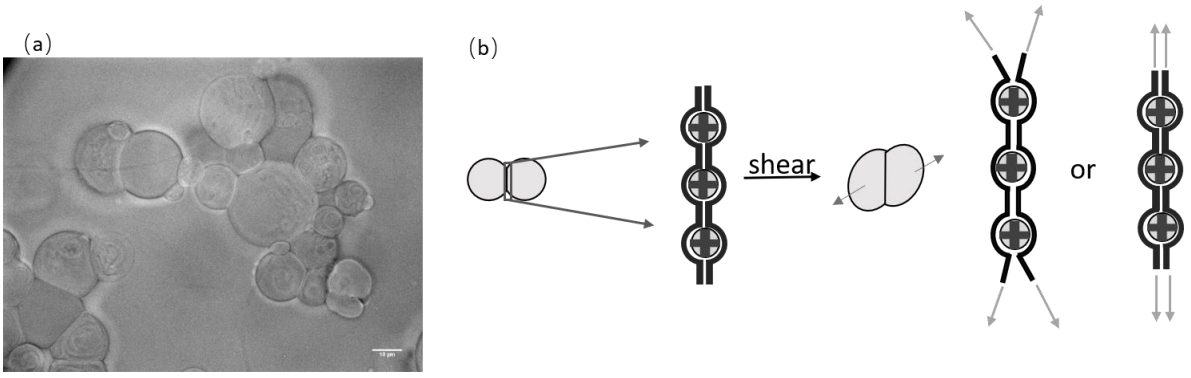

Figure 6.1: (a) Silica particles induced vesicle-vesicle adhesion. (b) Hypothesis of particle induced vesicle gel shear process.

6.2.3 Inside particle membrane interaction

In chapter 5, we introduced the particles that interacted with membranes outside vesicles. It is also challenging and interesting to discover what will happen if particles interact with membranes from the inner side of vesicles. With the charge-converting particles, it is possible to encapsulate light sensitive particles inside vesicles initially by electroformation or other fabrication methods, then shine UV to convert the particle property and see what the interaction would be. If vesicle rupture can be triggered, it is going be a novel way to do trigger-release and more efficient and robust to outside environment since the change of outside solvent does not affect the triggered-release process. On the other hand, if vesicle remain intact, we would like to know if vesicle toughness would be modified by particles binding to the membranes. The vesicle interaction from the inner side is illustrated in Figure 6.2.

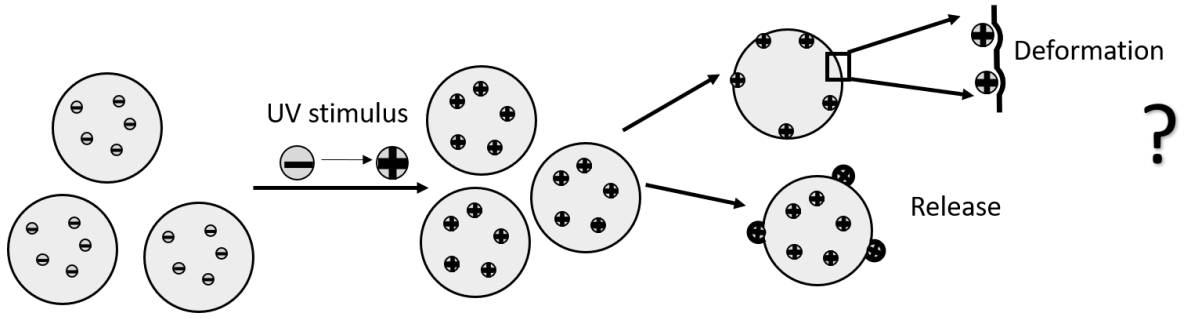

Figure 6.2: Schematic plot of particle membrane interaction from inner side of vesicles.

APPENDIX A

POLYMER SYNTHESIS PROCESS

In chapter 5, 3 kinds of polymers were mentioned: **P0**, **P1** and **P2**. The synthesis process of these polymer are described below. This work was done by Jingjing Gao, a graduate student working with Professor S. Thayumanvan in the University of Massachusetts Amherst Department of Chemistry. The procedure described here was adapted from our joint manuscript(Gao et al, Cellular AND Gates: Synergistic Recognition to Boost Selective Uptake of Polymeric Nanoassemblies, Angew. Chem. Int. Ed. 10.1002, 2020).

Synthesis of molecule **P0**: Monomer hexanyl coumarinyl methacrylate (HCM) and PEG_{5000}-chain transfer agent(PEG-CTA) were prepared according to previously reported procedures [41]. A solution of HCM (103 mg, 0.3 mmol), PEG-CTA (150 mg, 0.03 mmol) and 2,2'-Azobis(2-methylpropionitrile) (0.984 mg, 0.006 mmol), in tetrahydrofuran (400 mL) was degassed by three freeze-pump-thaw cycles before being sealed off under argon protection and vaccum. After 6 h at 65 °C, the polymerization media was diluted in dichloromethane and condensed using a rotavap, and precipitated in diethyl ether for 3 times to remove unreacted monomers. The precipitate was collected and dried under vacuum to yield 233 mg (93% yield) of P0. GPC (THF): Mn= 8.8 K Da, Đ= 1.02. ^{1}H NMR (400 MHz, $CDCl_3$) δ 7.45, 6.80, 6.79, 6.07, 3.97, 3.83, 3.66, 3.48, 2.36, 1.96, 1.82, 1.67, 1.50, 1.46, 1.26, 1.06, 0.89. From ^{1}H NMR, integration of peak at δ 6.07 and δ 3.83 provided the molar ratio of PEG/Coumarin to be 1:10. ^{13}C NMR (126 MHz, $CDCl_3$) δ 161.06, 154.19, 151.62, 124.54, 112.39, 111.52, 110.77, 100.16, 76.26, 76.01, 75.75, 69.56, 67.33, 52.41, 28.68, 27.94, 27.42, 27.08, 24.94, 24.74, 17.63.

Synthesis of polymer **P1**: **P0** was dissolved in dichloromethane/trifluoroaceticacid (1mL/1mL) mixture and stirred overnight at room temperature. The solvent was evaporated and redissolved in DCM, the solution was then dialyzed against DCM/MeOH to get purified P1 (95% yield). GPC (THF): Mn= 8.2 K Da, Đ= 1.05. ^{1}H NMR (400 MHz, $CDCl_3$) δ 7.43, 6.78, 6.67, 6.05, 3.95, 3.81, 3.63, 3.45, 2.34, 1.97, 1.80, 1.66,

1.43, 1.24, 1.04, 0.87. ^{13}C NMR (126 MHz, $CDCl_3$) δ 161.13, 160.76, 154.06, 152.17, 124.58, 112.39, 111.72, 110.55, 100.16, 69.35, 69.32, 69.23, 68.88, 67.37, 38.92, 28.68, 27.93, 27.08, 24.94, 24.73, 17.65.

Synthesis of polymer **P2**: 2-nitrobenzyl alcohol (10 eq. per NH_2 of **P1**) was dissolved in dried THF and stir with argon protection at room temperature, triphosgene (15 wt% in toluene, 20 eq. per NH_2 of **P1**) was added to the mixture and stirred for 2 hours, then the solution was rotavaped to remove solvent and dried with vaccum pump for 3 hours to remove extra phosgene. The residue was redissoved in DCM and added to a solution of **P1** (100 mg) and triethylamine (10 eq. per NH_2 of **P1**), the solution was stired at room temperature for 8 hours and then dialyzed against DCM/MeOH to get purified P2 (95% yield). GPC (THF): Mn= 8.2 K Da, Đ= 1.05. ^{1}H NMR (400 MHz, $CDCl_3$) δ 8.07, 7.62, 7.62, 7.43, 7.26, 6.79, 6.68, 6.06, 5.51, 5.29, 4.97, 3.96, 3.81, 3.63, 3.47, 3.45, 2.36, 2.35, 2.34, 1.97, 1.80, 1.66, 1.45, 1.43, 1.24, 1.05, 0.87. ^{13}C NMR (101 MHz, $CDCl_3$) δ 166.30, 162.06, 161.18, 155.19, 152.64, 145.96, 137.71, 128.35, 127.82, 126.64, 125.55, 113.40, 112.53, 111.77, 101.17, 77.37, 77.05, 76.73, 70.56, 70.56, 69.65, 68.36, 64.97, 45.61, 45.09, 44.68, 39.98, 29.70, 28.97, 28.11, 25.97, 25.76, 18.65, 8.52.

P0, **P1** and **P2** synthesis processes are illustrated in Figure A.

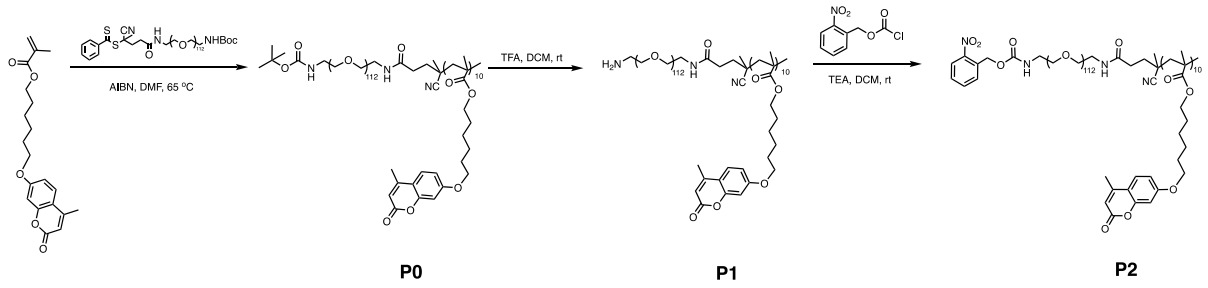

Figure A: **P0**, **P1** and **P2** synthesis processes.

REFERENCE

[1] J. C. S. Ho, C. Steininger, S. H. Hiew, M. C. Kim, E. Reimhult, A. Miserez, N. Cho, A. N. Parikh, and B. Liedberg, Biomacromolecules **20**, 1709 (2019).

[2] I. R. Cooke and M. Deserno, Biophys. J. **91**, 487 (2006).

[3] D. Chen and M. M. Santore, PNAS **111**, 179 (2014).

[4] K. Tsang, Y. Lai, Y. Chiang, and Y. Chen, Phys. Rev. E **012410**, 1 (2017).

[5] R. Tero, H. Watanabe, and T. Urisu, Phys. Chem. Chem. Phys. 3885 (2006).

[6] P. Maity, B. Saha, G. S. Kumar, and S. Karmakar, Biochim. Biophys. Acta - Biomembr. **1858**, 706 (2016).

[7] M. C. Smith, R. M. Crist, J. D. Clogston, and S. E. McNeil, Anal. Bioanal. Chem. **409**, 5779 (2017).

[8] M. Yanagisawa, M. Imai, T. Taniguchi, and F. Ade, Phys. Rev. Lett. **148102**, 1 (2008).

[9] W. Helfrich, Z. Naturforsch **28 c**, 693 (1973).

[10] A. Pressley, *Gaussian, Mean and Principal Curvatures 8* (2010).

[11] O.-Y. Zhong-can and W. Helfrich, Phys. Rev. A **39**, 5280 (1989).

[12] O.-Y. Zhong-can and W. Helfrich, Phys. Rev. Lett. **59**, 2486 (1987).

[13] M. Deserno, *Fluid Lipid Membranes – a Primer* (n.d.).

[14] D. I. Wilson, Eye **32**, 179 (2018).

[15] T. Mason, J. Bibette, D. Weitz, Phys. Rev. Lett. **75**, 2051 (1995).

[16] G. M. Kontogeorgis, B. Maribo-Mogensen, and K. Thomsen, Fluid Phase Equilib. **462**, 130 (2018).

[17] R. Kjellander and S. Marcelja, J. Phys. Chem. **90**, 1232 (1986).

[18] M. Deserno, Phys. Rev. E **69**, 031903 (2004).

[19] M. Dionzou, A. Morère, C. Roux, B. Lonetti, J. D. Marty, C. Mingotaud, P. Joseph, D. Goudounèche, B. Payré, M. Léonetti, and A. F. Mingotaud, Soft Matter **12**, 2166 (2016).

[20] C. Herold, G. Chwastek, P. Schwille, and E. P. Petrov, Langmuir **28**, 5518 (2012).

[21] Z. Földes-Papp, U. Demel, and G. P. Tilz, Int. Immunopharmacol. **3**, 1715 (2003).

[22] S. Hillyard, R. F. Loane, and J. Silcox, Ultramicroscopy **49**, 14 (1993).

[23] Y. Liu and J. Liu, Langmuir **36**, 810 (2020).

[24] S. Zuraw-Weston, D. A. Wood, I. K. Torres, Y. W. Lee, L. S. Wang, Z. Jiang, G. R. Lázaro, S. Y. Wang, A. A. Rodal, M. F. Hagan, V. M. Rotello, and A. D. Dinsmore, Nanoscale **11**, 18464 (2019).

[25] I. S. Sayed and N. S. Mohamed Nasrudin, Int. J. Med. Physics, Clin. Eng. Radiat. Oncol. **05**, 100 (2016).

[26] G. L. Gaines, *Critical Micelle Concentrations of Aqueous Surfactant Systems* (1971).

[27] A. Ramachandran, T. H. Anderson, L. G. Leal, and J. N. Israelachvili, Langmuir **27**, 59 (2011).

[28] E. Kizilay, S. Maccarrone, E. Foun, A. D. Dinsmore, and P. L. Dubin, J. Phys. Chem. B 7256 (2011).

[29] F. lix M. G. i Dov Lichtenberg, Hasna Ahyayauch, Biophys. J. **105**, 289 (2013).

[30] S. Hong, P. R. Leroueil, E. K. Janus, J. L. Peters, M. Kober, M. T. Islam, B. G. Orr, J. R. Baker, and M. M. B. Holl, Bioconjugate Chem **17**, 728 (2006).

[31] J. Lee, J. P. Gustin, T. Chen, G. F. Payne, and S. R. Raghavan, Langmuir 26 (2005).

[32] A. Meller, T. Gisler, D. A. Weitz, and J. Stavans, Langmuir **15**, 1918 (1999).

[33] Y. Mao, M.E. Cates, H.N.W. Lekkerkerker, Physica A **222**, 10 (1995).

[34] D. Marenduzzo, K. Finan, and P. R. Cook, J. Cell Biol. **175**, 681 (2006).

[35] C. De Recherche, P. Pascal, and A. A. Schweitzer, J. Colloid Interface Sci. **448**, 439 (1996).

[36] S. A. Shah, Y. Chen, K. S. Schweizer, and C. F. Zukoski, J. Chem. Phys. **119**, 8747 (2003).

[37] S. Aben, C. Holtze, T. Tadros, and P. Schurtenberger, Langmuir **28**, 7967 (2012).

[38] K. Ogle, J. Sanborn, A. N. Parikh, and R. S. Kraut, Front. Physiol. **3**, 1 (2012).

[39] Y. V Il, M. A. Schwo, and J. Wirz, J. AM. CHEM. SOC. **126**, 4581 (2004).

[40] M. Stieger, J. S. Pedersen, P. Lindner, and W. Richtering, Langmuir 7283 (2004).

[41] J. Gao, P. Wu, A. Fernandez, J. Zhuang, S. Thayumanavan, Angew. Chemie - Int. Ed **10**, 2 (2020).

[42] A. H. Bahrami, R. Lipowsky, and T. R. Weikl, Phys. Rev. Lett. **188102**, 1 (2012).

[43] M. Chambers, A. Mallory, H. Malone, Y. Gao, S. M. Anthony, Y. Yi, and Y. Yu, Soft Matter **12**, 9151 (2016).

[44] H. Duan, J. Li, H. Zhang, F. Qiu, and Y. Yang, J Biol Phys **44**, 1 (2018).

[45] J. Li, H. Zhang, F. Qiu, Y. Yang, and J. Z. Y. Chen, Soft Matter (2015).

[46] X. Yi and H. Gao, ACS Biomater. Sci. Eng **3**, 2954 (2017).

[47] Z. Shen, H. Ye, M. Kröger, and Y. Li, Nanoscale **10**, 4545 (2018).

[48] Q. Xia, H. Ding, and Y. Ma, Nanoscale **9**, 8982 (2017).

[49] H. A. Barnes, Colloids Surfaces A Physicochem. Eng. Asp. **91**, 89 (1994).

[50] J. Zhao and M. H. Stenzel, Polym. Chem. **9**, 259 (2018).

[51] H. Tang, H. Zhang, H. Ye, and Y. Zheng, J. Phys. Chem. B **122**, 171 (2018).

[52] K. Xiong, J. Zhao, D. Yang, Q. Cheng, J. Wang, and H. Ji, Soft Matter **13**, 4644 (2017).

[53] D. M. Richards and R. G. Endres, Rep. Prog. Phys. **80**, (2017).

[54] X. Yi, X. Shi, and H. Gao, Phys. Rev. Lett. **098101**, 1 (2011).

[55] B. Dollet and C. Raufaste, Comptes Rendus Phys. **15**, 731 (2014).

[56] P. Jiilicher and R. Lipowsky, Phys. Rev. Lett. **70**, 2964 (1993).

[57] K. Shigyou, K. H. Nagai, and T. Hamada, Langmuir 13771 (2016).

[58] K. Tsumoto, Y. Hayashi, J. Tabata, and M. Tomita, Colloids Surfaces A **546**, 74 (2018).

[59] M. I. Angelova, S. Soléau, P. Méléard, F. Faucon, and P. Bothorel, in *Trends Colloid Interface Sci. VI* (2007).

[60] K. Nishimura, H. Suzuki, T. Toyota, and T. Yomo, J. Colloid Interface Sci. **376**, 119 (2012).

[61] V. Trappe and D. A. Weitz, Phys. Rev. Lett. **1**, 449 (2000).

[62] S. Dey, S. Z. Ali, and E. Padhi, Proc. R. Soc. A **475**, (2019).

[63] A. Blanazs, S. P. Armes, and A. J. Ryan, Macromol. Rapid Commun **30**, 267 (2009).

[64] S. B. C. Particles, J. Lee, K. H. Ku, J. Kim, Y. J. Lee, S. G. Jang, and B. J. Kim, J. AM. CHEM. SOC. (2019).

[65] J. Stankovich and S. L. Carnie, Langmuir 1453 (1996).

[66] A. Berthault, M. Werner, V. A. Baulin, A. Berthault, M. Werner, and V. A. Baulin, J. Chem. Phys. **149**, (2018).

[67] D. Marsh, Chem. Phys. Lipids **144**, 146 (2006).

[68] E. Evans, V. Heinrich, F. Ludwig, and W. Rawicz, Biophys. J. **85**, 2342 (2003).

[69] L. Picas, F. Rico, and S. Scheuring, Biophys. J. **102**, L01 (2012).

[70] E. Evans and R. Kwok, Biochemistry 4874 (1982).

[71] E. Evans, C. V. T. W, and D. Needham, Faraday Discuss. Chem. Soc. **81**, 267 (1986).

[72] G. van Meer, D. R. Voelker, and G. W. Feigenson, Nat Rev Mol Cell Biol **9**, 112 (2008).

[73] A. Kuklin, D. Zabelskii, I. Gordeliy, J. Teixeira, A. Brûlet, V. Chupin, V. Cherezov, and V. Gordeliy, Sci. Rep. 1 (2020).

[74] F. R. Hall, Food Res. Int. **27**, 195 (1994).

[75] V. Pereno, D. Carugo, L. Bau, E. Sezgin, J. Bernardino, D. Serna, C. Eggeling, and E. Stride, ACS Omega **2**, 994 (2017).